Gyrokinetic theory of micro-instabilities in negative shear tokamaks

Yasuhiro Idomura

February 2000

Abstract

In order to study linear and nonlinear properties of micro-instabilities in negative shear tokamaks, a gyrokinetic integral eigenvalue code and a gyrokinetic finite element particle-in-cell (PIC) code are developed.

Numerical results show that both the slab ion temperature gradient (ITG) mode and the slab electron temperature gradient (ETG) mode become strongly unstable around the $q_{\min}$-surface, where $q_{\min}$ is the minimum value of a safety factor q. Both modes has three types of branches in the negative shear configuration: a single mode-rational surface mode, a double mode-rational surface mode, and a nonresonant mode. From a mixing length estimate of the transport coefficient, for both modes, a double mode-rational surface and nonresonant modes give a significant contribution to the anomalous transport.

The double mode-rational surface negative-sheared slab ITG (NS-ITG) mode becomes a bounded solution which is excited in the $q_{\min}$-surface region between two neighboring mode-rational surfaces. The nonresonant NS-ITG mode has an oscillatory solution around the $q_{\min}$-surface region. Their stability is basically determined locally at the $q_{\min}$-surface, because the magnetic shear is weak in the $q_{\min}$-surface region. For both the double mode-rational surface and nonresonant NS-ITG modes, an unstable k_y region spreads over a high k_y region with $k_y\rho_{ti} \sim 10$, where k_y is the wavenumber in the direction of the diamagnetic drift and ρ_{ti} is the ion Larmor radius.

The short wavelength ETG mode shows different features from the ITG mode, because the Debye shielding effect becomes important in typical fusion plasma parameters. In a Weber type differential eigenmode equation obtained with retaining the Debye shielding effect, a term which makes an effective potential has the opposite sign compared to that in the case of the ITG mode. Hence, types of solutions are exchanged between the ITG and ETG modes. The double mode-rational surface negative-sheared slab ETG (NS-ETG) mode has an oscillatory solution around the $q_{\min}$-surface. The nonresonant NS-ETG mode becomes a bounded solution. The NS-ETG modes give order of magnitude larger radial correlation lengths compared with that of the conventional normal-sheared slab ETG mode. Therefore, the corresponding mixing length estimate of the transport coefficient is significantly

large. As in the case of ITG modes, the stability of both the double mode-rational surface and nonresonant NS-ETG modes is also determined locally at the $q_{\min}$-surface. However, their unstable k_y regions are characterized by $k_y\lambda_{De} \sim 1$, because of the Debye shielding effect, where λ_{De} is the electron Debye length.

In the normal shear case, the unstable k_y region of the ITG mode with $k_y\rho_{ti} < 1$ and that of the ETG mode with $k_y\lambda_{De} < 1$ are separated. However, in the negative shear case, their unstable regions overlap each other around $k_y\rho_{ti} \sim 10$ ($k_y\lambda_{De} \sim 0.4$). Since the growth rate of the ETG modes is an order of magnitude larger than that of the ITG modes, effects of the ETG turbulence is significant in studying the ITG turbulence.

The ETG turbulence in a slab configuration modeling the negative shear tokamak is studied using a gyrokinetic finite element PIC code. It is found that quasi-steady $E_r \times B$ zonal flows are generated in finite magnetic shear regions in both sides of the $q_{\min}$-surface, where the electron thermal transport is reduced substantially. Stability analyses of the electrostatic Kelvin-Helmholtz (K-H) mode show that the quasi-steady $E_r \times B$ zonal flow profile is closely related to the q-profile or the magnetic shear, which has a stabilizing effect on the K-H mode. By changing the q-profile to reduce the magnetic shear, the K-H mode becomes unstable for the quasi-steady $E_r \times B$ zonal flows, and the $E_r \times B$ zonal flows disappear in the weak magnetic shear region. Numerical results show a possibility of controlling $E_r \times B$ zonal flows with the magnetic shear, through the stability of the K-H mode. Also, it is shown that the microscopic $E_r \times B$ zonal flows arising from the ETG turbulence have a strong stabilizing effect on the ITG mode.

Contents

Acknowledgments

I would like to express my gratitude to Prof. Masahiro Wakatani for his supervision in my doctoral program. He accepted me to the laboratory, and led me to the field of theoretical plasma physics. I was aided by his patient encouragement and support.

I also owe gratefulness to Prof. Kyuya Kotajima for serving as my adviser during my undergraduate program at Tohoku University.

I have addressed this work as my doctoral research through a collaboration with Dr. Shinji Tokuda of Japan Atomic Energy Research Institute (JAERI). His insights about a fusion plasma research inspired me to work on the gyrokinetic theory. I would like to express my deep appreciation to him.

I acknowledge to Prof. Katsumi Kondo and Dr. Satoshi Hamaguchi for reading the manuscript and making useful comments and suggestions.

I stayed at Naka Fusion Research Establishment, JAERI in 1997. That time was a great experience to me, and a lot of basic concepts in this work were established. I enjoyed fruitful discussions with Dr. Shinji Tokuda, Dr. Yasuaki Kishimoto, Dr. Takahisa Ozeki, Dr. Tomonori Takizuka, and other members of Plasma Theory Laboratory. Also, I was stimulated by discussions with visitors at JAERI, especially Dr. Taik Soo Hahm and Dr. Greg Rewoldt of Princeton Plasma Physics Laboratory, and Dr. Jean Noel Lebouf of the University of California at Los Angeles. To all these people, I would like to express my appreciation. In particular, I am grateful to Dr. Toshio Hirayama and Dr. Masafumi Azumi for giving me an opportunity to study at JAERI.

I thank to Dr. Hiroshi Naitou of Yamaguchi University for many instructive discussions on the particle simulation technique. The first version of my gyrokinetic particle-in-cell (PIC) code was developed based on his electromagnetic gyrokinetic PIC code, GYRO3D.

To Dr. Hideo Sugama of the National Institute for Fusion Science (NIFS) and Dr. Yuji Nakamura of Kyoto University, I owe much appreciation for helpful discussions and suggestions.

I was helped and encouraged by many colleagues. Especially, I owe thanks to Dr. Masayuki Yokoyama of NIFS, Dr. Yasutomo Ishii and Dr. Taro Matsumoto of JAERI,

Dr. Mitsuru Hayashi of the National Astronomical Observatory, and Dr. Stuart Ronald Hudson of the University of Wisconsin-Madison.

The numerical computations in this work were performed on COMplex PArallel Computer System (COMPACS) of the Center for Promotion of Computational Science and Engineering, JAERI, Paragon XP/S-75MP834 system of Kansai Research Establishment, JAERI, and SX-4/64M2 system of Theory and Computer Simulation Center, NIFS. I thank to computational stuffs in these institute for supporting the development and execution of my codes.

I have been supported by the intern program of JAERI and the Research Fellowships of the Japan Society for the Promotion of Science for Young Scientists. This work was also supported partly by the Numerical EXperiment of Tokamak (NEXT) project at JAERI.

Finally, I wish to express my gratitude to many teachers, researchers, and stuffs at the Institute of Advanced Energy, Kyoto University and Naka Fusion Research Establishment, JAERI.

Chapter 1

Introduction

Understanding of a transport process in fusion plasmas is one of critical issues for a future development of the magnetic thermonuclear fusion reactor, because the energy confinement time determines the reactor size which greatly affects economical efficiency. In order to investigate the turbulent transport in tokamaks, the gyrokinetic theory [1, 2, 3, 4, 5] has been developed. The gyrokinetic theory provides a rigorous kinetic description of low frequency phenomena in high temperature tokamak plasmas. In this thesis, particularly for negative shear tokamaks, various linear and nonlinear properties of micro-instabilities such as the ion temperature gradient driven (ITG) mode and the electron temperature gradient driven (ETG) mode are addressed, based on the gyrokinetic theory.

1.1 Brief historical review and motivation

Early experimental researches on the energy confinement property in DOUBLET III [6, 7] have shown that both the ion and electron heat conductivities are considerably high compared with predictions by the neoclassical theory. It has been believed that the tokamak anomalous transport is produced by a plasma turbulence. From density fluctuations observed by the beam emission spectroscopy (BES) measurement, correlation between low frequency density fluctuations and the anomalous heat conductivity was confirmed [8] in the Tokamak Fusion Test Reactor (TFTR) [9]. Drift-type micro-instabilities has been considered as a driving mechanism of a plasma turbulence, because they becomes unstable

easily for finite density and temperature gradients even in a configuration where magneto-hydrodynamic (MHD) instabilities are suppressed. From comprehensive theoretical studies on linear properties of micro-instabilities, various ion and electron modes have been found. Although the distinction among several branches of drift-type instabilities is sometimes difficult, they are classified mainly into the slab mode, the toroidal mode, and the trapped particle mode, depending on their driving mechanisms. The slab drift mode [10, 11] is the most basic drift wave which is excited by a resonance of particle motion with a wave phase velocity in the direction parallel to the ambient magnetic field. The toroidal mode [12] is destabilized by the magnetic drift in a bad curvature region of a toroidal plasma. The trapped particle mode [10] is caused by a resonance of the precessional drift of trapped particles with a wave phase velocity. Low frequency density fluctuations propagating in the ion diamagnetic direction was observed firstly in the Texas EXperimental Tokamak (TEXT) [13], and later in other machines [14, 15]. Thus, a model of the ion anomalous transport based on the ITG mode has been widely accepted in the magnetic fusion community, and substantial efforts have been made for a study of the ITG turbulence. Also, low frequency density fluctuations propagating in the electron diamagnetic direction have been reported [14]. From comprehensive linear kinetic calculations [16, 17], the toroidal ITG mode and the trapped electron mode (TEM) have been considered as important candidates for these ion branch and electron branch fluctuations.

However, in recent advanced tokamak configurations with a reversed magnetic shear or a negative shear configuration, the observed confinement properties have been drastically changed from those in the conventional normal shear experiments. In the negative shear tokamaks, significant improvement of particle and energy confinement due to the internal transport barrier (ITB) has been observed [18, 19, 20]. The ITB in the weak magnetic shear region was firstly observed in the Japan Atomic Energy Research Institute Tokamak-60 Upgrade (JT-60U) [21]. The energy break-even will be expected in the reversed shear plasmas with the ITB on JT-60U [22]. Since the configuration is realized with a high fraction of the bootstrap current, the negative shear configuration is considered as a promising operation mode in future tokamak reactors. The ITB in the negative shear tokamaks is characterized by steep density and temperature gradients near the $q_{\min}$-surface, and often,

sheared poloidal and toroidal flows are observed in the same region. Here, the $q_{\min}$-surface is a magnetic surface where a safety factor q becomes the minimum value. Recent transport analyses for negative shear tokamak experiments [23, 24] have shown that the ion thermal diffusivity reduces to the neoclassical level in the internal transport barrier (ITB) region. This transport reduction is well explained by a model based on a $E_r \times B$ flow shear suppression [25] for micro-instabilities, especially for the ITG mode. And, coincidence between the region of the flow shear suppression for the ITG mode, which is characterized by the empirical condition, $\omega_{E_r \times B} > \gamma_{\max}$ [26], and the region of the reduced ion thermal diffusivity has been obtained experimentally, where $\omega_{E_r \times B}$ is the $E_r \times B$ shearing rate and $\gamma_{\max}$ is the maximum growth rate of the ITG mode. Although the TEM has also been considered to be stabilized with the observed $\omega_{E_r \times B}$, the electron thermal diffusivity is often still anomalous in the ITB region. Recently, the ETG mode [27, 28] has been proposed as a cause of the electron anomalous transport in the ITB [29]. In analyses for the DIII-D negative shear discharges [30], it has been shown that the growth rate of the toroidal ETG mode greatly exceeds an observed $E_r \times B$ shearing rate, and that the electron temperature gradient is limited by its critical value where the toroidal ETG mode is marginally stable.

In most of analyses mentioned above, linear growth rates have been evaluated with kinetic ballooning calculations [16, 17], which solves a linear gyrokinetic eigenmode equation under the ballooning representation or the Wentzel-Kramers-Brillouin (WKB) approximation. Since the scale length ordering between the radial mode structure and equilibrium profiles or $k_r^{-1}/L_n \sim k_r^{-1}/L_t \ll 1$ has been considered to be valid for relatively high-n modes in the conventional normal shear tokamaks, the WKB method has been adopted in these calculations, where n is a toroidal mode number, k_r is a wavenumber in the radial direction, and L_n and L_t are scale lengths of the density and temperature gradients, respectively. However, as is shown in recent works using the gyrokinetic global spectral code [31, 32], the linear gyrokinetic particle-in-cell (PIC) code [33], and the nonlinear gyrokinetic PIC codes [34, 35], medium (or low)-n modes have a global radial eigenmode structure. Furthermore, in negative shear tokamaks, steep gradients in density and temperature profiles have been observed in the ITB region or a weak magnetic shear region around the $q_{\min}$-surface. Here, the scale length ordering should be modified as $k_r^{-1}/L_n \sim k_r^{-1}/L_t \leq 1$, where the

WKB approximation may not be a good approximation. Also, in analyzing various micro-instabilities ranging from a relatively long wavelength ITG mode to a short wavelength ETG mode, a treatment of the full finite Larmor radius (FLR) effect is required. Therefore, a global approach based on a gyrokinetic integral eigenmode equation is required for studying properties of micro-instabilities in the ITB region of the negative shear tokamaks.

Although several kinetic eigenvalue codes based on the Vlasov or gyrokinetic integral eigenmode equation have been developed both for a slab or cylinder geometry [31, 36, 37], and for a toroidal geometry [32, 38], numerical results for clarifying properties of micro-instabilities in the negative shear configuration were very limited. Only a few cases have been reported in Ref. [32], where the ITG mode with a medium-n mode number ($n \simeq 10$) shows a slab-like eigenmode structure in the negative shear configuration. This may imply an importance of the slab ITG mode in the negative shear configuration.

The linear theory is useful in providing many insights on the driving mechanism, the characteristic wavelength and frequency, and the marginal stability condition. However, as for a study of micro-instabilities, prior attention should be paid to their nonlinear properties, because fluctuations which are usually observed in tokamak plasmas are considered as a nonlinearly saturated state of micro-instabilities. In relation to $E_r \times B$ flow shear stabilization of the ITG mode, the linear stability analyses were performed for a model $E_r \times B$ shear flow [37, 39]. Also, using the empirical condition, $\omega_{E_r \times B} > \gamma_{\max}$, the $E_r \times B$ flow shear suppression has been discussed for the experimental $E_r \times B$ shear flow [24, 30]. However, important nonlinear issues such as a generation of self-consistent $E_r \times B$ shear flows in a neutral plasma can not be resolved only by the linear theory. Therefore, it is essential to consider a nonlinear approach in analyzing the transport properties of fusion plasmas. A lot of theoretical attempts have been made to describe nonlinear properties of micro-instabilities. The quasilinear theory and the weak turbulence theory [40, 41] are standard descriptions of a drift wave turbulence in tokamak plasmas, which is considered as a weak turbulence. However, the present existing theories are not enough for explaining the experimental data completely. Therefore, future experimental devices such as the International Thermonuclear Experimental Reactor [42] (ITER) have been designed principally based on the empirical energy confinement scalings obtained from the experimental

database.

Besides experimental and theoretical approaches, recent progress on high performance computers and numerical techniques suggest the third approach, a computer simulation or a numerical experiment. The particle simulation model of plasma is one of standard simulation methods in the space and laboratory plasma research [43, 44, 45]. In this model, a plasma is simulated by following motions of a large number of particles in the self-consistent electromagnetic fields, which is described with the coupled Newton-Maxwell equations. Thus, the particle model essentially describes all the phenomena ranging from the microscopic phase space trajectory [46] to the macroscopic collective motion. Since simulations based on the particle model require a large storage memory and a high computational speed, both the time and spatial scales of phenomena investigated by the particle model were greatly limited with the available computational resources. However, recent improvements in simulation techniques and development of parallel computers make a large scale plasma simulation with $\sim 10^9$ particles possible.

As for a simulation modeling in the fusion plasma research, a global gyrokinetic particle simulation has become a powerful tool in a study of kinetic instabilities in tokamaks. In these problems, the frequency of the drift wave or the kinetic MHD mode is much smaller than that of basic plasma phenomena, such as the plasma oscillation or gyro-motion of particles. Hence, in order to explore the low frequency physics in tokamaks, the empirical gyrokinetic model was firstly proposed by Lee [1]. Then, the model was refined in an excellent way using the action-variational Lie perturbation method [47, 48], and the gyrokinetic formalism of the Vlasov-Maxwell system was derived [3, 4, 5]. The gyrokinetic Vlasov-Maxwell system was successfully implemented on the gyrokinetic particle simulation code [49]. In the gyrokinetic Vlasov-Maxwell equations, the gyro-motion of particles, and the waves arising from the gyro-resonances, are removed analytically without losing important physical effects such as the FLR effect and the polarization effect of the gyrating particles. Also in this system, the plasma oscillation (the longitudinal wave) is excluded because of the gyrokinetic ordering, $k_\parallel / k_\perp \sim \mathcal{O}(\epsilon)$, where $k_\parallel, k_\perp$ are the wave vectors in the parallel and perpendicular direction to the ambient magnetic field, respectively. As a result, the global gyrokinetic particle simulation is enabled with the simulation time step

of $\sim \Omega^{-1}$ and the spatial grid size of $\sim \rho$, where Ω and ρ denote the gyro-frequency and the gyro-radius, respectively.

In recent years, the ITG turbulence has been studied intensively using the global [34, 35] and local [50] gyrokinetic PIC codes. And, a modeling for the gyrokinetic particle simulation tends to converge through a number of linear and nonlinear benchmarks [51]. One of the most important physics found in those simulations is a reduction of the ion anomalous transport due to the turbulent driven $E_r \times B$ shear flows or zonal flows [35]. The generation of $E_r \times B$ shear flows or $E_r \times B$ zonal flows in a magnetized plasma was discussed by several authors. Hasegawa *et al.* discussed a self-organization process of an electrostatic drift wave turbulence by analogy to a Rossby wave turbulence [52]. A generation of shear flow due to a self-organization process or an inverse wave energy cascade was shown for the electrostatic turbulence [53]. Diamond and Kim proposed the flow generation mechanism based on the turbulence-induced Reynolds stress [54]. Recently, Diamond *et al.* discussed the modulational instability of coherent drift waves as a mechanism of zonal flow generation [55].

However, we recognize that for keeping quasi-steady $E_r \times B$ shear flows, the $E_r \times B$ shear flows should be linearly stable for perturbations destroying the flow structure. As is shown by the Rayleigh necessary condition for instability, it is well known that the Kelvin-Helmholtz (K-H) mode becomes unstable in a neutral fluid or a plasma, provided that the flow velocity profile has an inflection point of flow shear [56]. Accordingly, if we assume a homogeneous magnetized plasma in a uniform background field with sufficiently large system size that satisfies $L_v/L_x < 1$, the K-H mode is basically unstable for $E_r \times B$ zonal flows, where L_x is a system size and L_v is a characteristic scale length of flow shear. Therefore, an intrinsic stabilizing effect on the K-H modes is required for sustaining quasi-steady $E_r \times B$ zonal flows.

Also, from a comparison between the gyrokinetic [50] and gyro-Landau fluid [57] simulations of the ITG turbulence, it was shown that a damping mechanism of the $E_r \times B$ zonal flow play a critical role for determining an ion thermal diffusivity in the saturated stationary state. Rosenbluth *et al.* have shown that a damping of a poloidal flow is sufficiently weak in collisionless high temperature plasmas [58]. However, if $E_r \times B$ shear flows

become unstable to the K-H mode, $E_r \times B$ shear flows are destroyed easily. Therefore, it is crucial to study the stability of $E_r \times B$ shear flows or $E_r \times B$ zonal flows, especially for understanding the transport properties of the ITB in negative shear tokamaks, where $E_r \times B$ shear flows are considered to play a critical role.

1.2 Outline

In Chapter 2, basic equations are derived, and their physical meanings are discussed. In Section 2.2, by showing the formulation of the kinetic equations from the Newton-Maxwell equations to the Vlasov-Maxwell equations, the basis for the collisionless or Vlasov description of a plasma is discussed. In Section 2.3, the gyrokinetic Vlasov-Maxwell system is formulated based on the Lagrangian formalism of the action variational Lie perturbation method. In Section 2.4. a similar approach is also considered for the treatment of the transit motion of high energy passing electrons, and the equation system is extended to include the orbit-averaged electron drift-kinetic equation [59]. This equation system enables an efficient description of the low frequency phenomena with thermal electrons. In Section 2.5, the energy conservation low is derived from an intrinsic nature of the Hamiltonian system, which is conserved via an area preserving property of the Lie transform.

Linear calculations for the slab ITG mode and the slab ETG mode in the negative shear configuration with TFTR like parameters are presented in Chapters 3 and 4. In Section 3.2, the linearized gyrokinetic Vlasov-Maxwell system is formulated to derive a gyrokinetic integral eigenvalue equation with retaining the full kinetic responses of ions and electrons. Although a full toroidal calculation is essential for quantitative understanding of the linear stability, it is useful to capture the underlying physics even with a preliminary sheared slab model. In studying micro-instabilities in such a new configuration as the negative shear configuration, it is also important to restructure a linear theory of slab drift waves before doing full toroidal calculations. Therefore, we have started a development of our code from a sheared slab geometry.

Depending on a number of the mode-rational surfaces, the slab ITG mode in the negative shear configuration has three types of branches: a single mode-rational surface

mode, a double mode-rational surface mode, and a nonresonant mode. In Section 3.3, for the latter two modes, new analytic solutions of the negative-sheared slab ITG (NS-ITG) [60] mode are presented using a Weber type differential eigenmode equation. In Section 3.4, all three types of the NS-ITG modes are identified in numerical results obtained from the gyrokinetic integral eigenvalue code. The stabilizing and destabilizing mechanisms of the NS-ITG mode are discussed in detail based on both the fluid and kinetic pictures.

Similar three types of solutions are also found for the slab ETG mode. However, unlike the conventional theory of the ETG mode [10], it is found that the ITG and ETG modes show different features for the present plasma parameters. In Sec 4.2, analytic solutions of the negative-sheared slab ETG (NS-ETG) [61] mode are obtained from a new Weber type differential eigenmode equation which is formulated with retaining the Debye shielding effect. This new eigenmode equation shows that for typical fusion plasma parameters with $\lambda_{De}^2 \gg \rho_{te}^2$, the Debye shielding is effective for the ETG mode, while for the ITG mode, the quasineutrality condition is imposed by the ion polarization. Here, λ_{De} is the electron Debye length and ρ_{te} is the electron Larmor radius. In Section 4.3, numerical solutions of the NS-ETG mode is obtained by the gyrokinetic integral eigenvalue code. In Section 4.4, the obtained numerical solutions of ITG and ETG modes are compared quantitatively with respect to the growth rate spectra, the critical values of the temperature gradient parameter, and the mixing length estimate for the transport coefficients. From these linear calculations, it is shown that a plasma turbulence in the negative shear tokamaks is considerably different from that in the normal shear tokamaks.

In Chapter 5, nonlinear simulations of the ETG turbulence [62, 63] are presented with a gyrokinetic finite element PIC code [33]. In the numerical results, a generation mechanism and a stability of turbulent driven $E_r \times B$ zonal flows are investigated intensively. In Section 5.2, an implementation of the gyrokinetic finite element PIC code is described. The simulations of the nonresonant NS-ETG mode are shown in Section 5.3. A spontaneous generation of $E_r \times B$ zonal flows is observed in the simulations. Effects of $E_r \times B$ zonal flows on the electron anomalous transport are discussed based on the simulation data. In Section 5.4, a stability of $E_r \times B$ zonal flows is studied from a point of view of the K-H instability. The magnetic shear stabilization of the K-H mode is shown both in analytical

and numerical calculations. Also, a dependence of the marginal $E_r \times B$ shear flow velocity on the magnetic shear is studied using the gyrokinetic integral eigenvalue code, which is extended to include an equilibrium $E_r \times B$ shear flow. From a comparison between linear calculations of the K-H mode and the observed $E_r \times B$ zonal flow profile, it is shown that the K-H mode plays a critical role in the underlying physics of the $E_r \times B$ zonal flow in the ETG turbulence. A possibility of controlling the $E_r \times B$ zonal flow and resulting confinement improvement is discussed. In Section 5.5, the linear stability of the ITG mode in the presence of the $E_r \times B$ zonal flows is analyzed using a gyrokinetic Fourier particle code in which the full FLR effect is involved. From numerical results, it is shown that the microscopic $E_r \times B$ zonal flow with $\rho_{ti}/L_v \sim \mathcal{O}(1)$ is effective for stabilizing the ITG mode.

Finally, in Chapter 6, obtained physical results are summarized, and conclusions of this thesis are presented. Also, remarks for future studies are discussed.

Chapter 2

Gyrokinetic Vlasov-Maxwell system

2.1 Introduction

The Newton-Maxwell equation system is the most rigorous description of the dynamical system consist of many charged particles. However, since it is impossible to follow all the particle motions in the system directly, some statistical treatment is required for describing a many charged particle system or a plasma. The Vlasov-Maxwell system is considered as a statistical description of a collisionless plasma. When a discreteness parameter is sufficiently small like a fusion plasma, the Vlasov-Maxwell system is useful to study various kinetic phenomena. However, in analyzing relatively low frequency waves, the frequencies of either the collisionless drift wave or the kinetic MHD mode are much smaller than that of basic dynamics, such as the plasma oscillation or the gyro-motion of particles. Hence, in order to investigate the low frequency physics in fusion plasmas efficiently, the gyrokinetic formalism [1, 2, 3, 4, 5] of the Vlasov-Maxwell equations has been developed.

In the gyrokinetic theory, time scales of a fast gyro-motion of particles and low frequency waves are separated under the gyrokinetic ordering. Using the action-variational Lie perturbation method [47, 48], a fast periodic gyro-motion, which is recognized as a non-secular perturbation in low frequency waves, is removed from the system, and the gyrokinetic Vlasov-Maxwell system appropriate for a description of low frequency phenomena is derived without losing important physics, such as the FLR effect.

A similar treatment is also considered for disparate time scales between a parallel thermal motion, which is characterized by a bounce frequency or a transit frequency in a toroidal plasma, and low frequency waves. Within the gyrokinetic model, we present an orbit-averaging model [59] for high energy passing electrons. In this model, the action-variational Lie perturbation method is applied to the treatment of the transit motion of fast passing electrons in a slab configuration. Since the inherent nature of the Hamiltonian system is kept in the Lie transform, a conservation low is straightforwardly derived also for the system with the gyrokinetic and orbit-averaging model.

2.2 Vlasov-Maxwell system

By following the text book by Ichimaru [64], we derive kinetic equations for a plasma consist of single species charged particles with a smeared-out neutralizing background charge (or the one component plasma).

A system of many charged particles is fully described by the Newton-Maxwell equations,

$$\frac{d\mathbf{x}_j}{dt} = \mathbf{v}_j, \tag{2.1}$$

$$\frac{d\mathbf{v}_j}{dt} = \frac{q}{m}\mathbf{E}(\mathbf{x}_j), \tag{2.2}$$

$$\nabla^2\phi(\mathbf{x},t) = 4\pi q\left[n - \sum_{j=1}^{N}\delta(\mathbf{x}-\mathbf{x}_j(t))\right], \tag{2.3}$$

$$\mathbf{E}(\mathbf{x},t) = -\nabla\phi(\mathbf{x},t), \tag{2.4}$$

where x_j and v_j are the position and velocity of j-th particle, respectively, m is the mass, q is the charge, n is the average number density, N is the number of particles, ϕ is the electrostatic potential, and $\mathbf{E}(\mathbf{x},t)$ is the electric field. In Eqs. (2.1)-(2.4), the electrostatic approximation is used for simplicity.

In order to change the description of the system from Lagrangian variables to Eulerian variables, we introduce the Klimontovich distribution function,

$$\mathcal{N}(\mathbf{X}) = \sum_{j=1}^{N}\delta(\mathbf{X}-\mathbf{X}_j(t)), \tag{2.5}$$

$$\mathbf{X}_j(t) \equiv [\mathbf{x}_j(t), \mathbf{v}_j(t)], \tag{2.6}$$

where $\mathbf{X}_j(t)$ denotes the j-th particle trajectory in the six-dimensional phase space. The distribution function (2.5) satisfies the continuity equation in the $6N$-dimensional phase space,

$$\frac{d\mathcal{N}}{dt} = \frac{\partial\mathcal{N}}{\partial t} + \dot{\mathbf{X}}\cdot\frac{\partial\mathcal{N}}{\partial\mathbf{X}} = 0. \tag{2.7}$$

Writing the phase space coordinates explicitly and using Newton's equation (2.1) and (2.2), we have

$$\frac{\partial\mathcal{N}}{\partial t} + \mathbf{v}\cdot\frac{\partial\mathcal{N}}{\partial\mathbf{x}} + \frac{q}{m}\mathbf{E}\cdot\frac{\partial\mathcal{N}}{\partial\mathbf{v}} = 0, \tag{2.8}$$

which is coupled with the Poisson equation (2.3) through the electric field (2.4) to obtain a closed set of equations. By assuming a system without an external electric field, $\mathbf{E}$ is represented explicitly with the analytical solution of the Poisson equation,

$$\mathbf{E}(\mathbf{x},t) = -q\frac{\partial}{\partial\mathbf{x}}\int d\mathbf{X}'\frac{\mathcal{N}(\mathbf{X}')}{|\mathbf{x}-\mathbf{x}'|}. \tag{2.9}$$

Substituting the expression (2.9) into Eq.(2.8), we obtain the Klimontovich equation,

$$\left[\frac{\partial}{\partial t} + \mathcal{L}(\mathbf{X}) - \int d\mathbf{X}'\mathcal{V}(\mathbf{X},\mathbf{X}')\mathcal{N}(\mathbf{X}')\right]\mathcal{N}(\mathbf{X}) = 0, \tag{2.10}$$

$$\mathcal{L}(\mathbf{X}) = \mathbf{v}\cdot\frac{\partial}{\partial\mathbf{x}}, \tag{2.11}$$

$$\mathcal{V}(\mathbf{X},\mathbf{X}') = \frac{q^2}{m}\left(\frac{\partial}{\partial\mathbf{x}}\frac{1}{|\mathbf{x}-\mathbf{x}'|}\right)\cdot\frac{\partial}{\partial\mathbf{v}}, \tag{2.12}$$

where $\mathcal{L}(\mathbf{X})$ denotes a single-particle operator and $\mathcal{V}(\mathbf{X},\mathbf{X}')$ is a two-particle operator arising from Coulomb interaction.

The Klimontovich equation is a rigorous microscopic description of a fully ionized plasma and gives a deterministic time evolution of a plasma in the phase space, provided that we could set the initial conditions for all the particles. However, it is impossible to perform orbit calculations for $\sim 10^{20}\mathrm{m}^{-3}$ of charged particles. From a practical point of view, it is not necessary to obtain the time evolution of all the particles, and, therefore, we consider a coarse-graining treatment in the following.

In the $6N$-dimensional phase space, the phase point is defined as

$$\{\mathbf{X}_i\} \equiv (\mathbf{X}_1, \mathbf{X}_2, \cdots, \mathbf{X}_N). \tag{2.13}$$

Here, we consider statistical ensembles $\mathcal{I}$ for the system $\{\mathbf{X}_i\}$ and introduce the Liouville distribution $D(\{\mathbf{X}_i\};t)$ in the $6N$-dimensional phase space according to

$$D(\{\mathbf{X}_i\};t)d\{\mathbf{X}_i\} \equiv \lim_{\mathcal{I}\to\infty}\frac{\mathcal{I}_i}{\mathcal{I}}, \tag{2.14}$$

where $\mathcal{I}_i$ refers to the number of ensembles in an infinitesimal volume $d\{\mathbf{X}_i\}$ around $\{\mathbf{X}_i\}$. By the definition it satisfies the normalization condition

$$\int d\{\mathbf{X}_i\}\, D(\{\mathbf{X}_i\};t) = 1. \tag{2.15}$$

By using the Liouville distribution (2.14), the ensemble average of a microscopic quantity $A(\mathbf{X}_1,\mathbf{X}_2,\cdots,\mathbf{X}_N;\{\mathbf{X}_i\})$ is defined as

$$\langle A(\mathbf{X}_1,\mathbf{X}_2,\cdots,\mathbf{X}_N;t)\rangle = \int d\{\mathbf{X}_i\}\, D(\{\mathbf{X}_i\};t) A(\mathbf{X}_1,\mathbf{X}_2,\cdots,\mathbf{X}_N;\{\mathbf{X}_i\}). \tag{2.16}$$

The s-particle distribution function $F_s(1,2,\cdots,s)$ is obtained by averaging the Klimontovich distribution as

$$F_1(1) = \langle \mathcal{N}(1;t)\rangle, \tag{2.17}$$

$$F_2(1,2) = \langle \mathcal{N}(1;t)\mathcal{N}(2;t)\rangle - \delta(1-2)F_1(1), \tag{2.18}$$

$$F_3(1,2,3) = \langle \mathcal{N}(1;t)\mathcal{N}(2;t)\mathcal{N}(3;t)\rangle - \delta(1-2)\delta(1-3)F_1(1) - \delta(1-2)F_2(2,3) - \delta(2-3)F_2(3,1) - \delta(3-1)F_2(1,2), \tag{2.19}$$

where the coordinates, $\mathbf{X}_1,\mathbf{X}_2,\cdots$, are replaced by simplified notations, $1,2,\cdots$. The higher-order distributions have information of interaction between multi-particles. On the other hand, the single-particle distribution is sufficient for a kinetic description of a collective motion in a plasma. The s-particle distribution function is calculated by using the ensemble averaged Klimontovich equation.

The Klimontovich equation (2.10) is written using a notation introduced above as

$$\left[\frac{\partial}{\partial t} + \mathcal{L}(1) - \int d\mathbf{X}_2 \mathcal{V}(1,2)\mathcal{N}(2;t)\right]\mathcal{N}(1;t) = 0. \tag{2.20}$$

Carrying out the ensemble average of this equation, we have an equation for the single-particle and two-particle distributions,

$$\left[\frac{\partial}{\partial t} + \mathcal{L}(1)\right]F_1(1) = \int d\mathbf{X}_2 \mathcal{V}(1,2)F_2(1,2). \tag{2.21}$$

Here, from the symmetry of the two-particle operator $\mathcal{V}(1,2)$, a relation

$$\int d\mathbf{X}_2 \delta(1-2)\mathcal{V}(1,2)F_2(1,2) = 0, \tag{2.22}$$

is used. For the two-particle and three-particle distributions, we transform the Klimontovich equation in the following form,

$$\left[\frac{\partial}{\partial t} + \mathcal{L}(1) + \mathcal{L}(2)\right]\mathcal{N}(1;t)\mathcal{N}(2;t) = \int d\mathbf{X}_3 \left[\mathcal{V}(1,3)+\mathcal{V}(2,3)\right]\mathcal{N}(1;t)\mathcal{N}(2;t)\mathcal{N}(3;t), \tag{2.23}$$

By taking the ensemble average of Eq. (2.23), we obtain an equation for the two-particle and three-particle distributions,

$$\left[\frac{\partial}{\partial t} + \mathcal{L}(1) + \mathcal{L}(2) - \left[\mathcal{V}(1,2)+\mathcal{V}(2,1)\right]\right]F_2(1,2) = \int d\mathbf{X}_3 \left[\mathcal{V}(1,3)+\mathcal{V}(2,3)\right]F_3(1,2,3). \tag{2.24}$$

These procedures are analogously extended to the s-particle distribution function and we have the Bogoliubov-Born-Green-Kirkwood-Yvon (BBGKY) hierarchy equations,

$$\left[\frac{\partial}{\partial t} + \sum_i^s \mathcal{L}(i) - \sum_{i\neq j}^s \mathcal{V}(i,j)\right]F_s(1,\cdots,s) = \sum_i^s \int d\mathbf{X}_{s+1}\mathcal{V}(i,s+1)F_{s+1}(1,\cdots,s,s+1). \tag{2.25}$$

Since the BBGKY hierarchy has a structure such that the s-particle distribution function depends on the $(s+1)$-particle distribution function, there is no straightforward closed form in itself. We then consider a truncation method for the hierarchy equations.

The discreteness parameter Δ is defined as the inverse of the number of particles contained in the Debye sphere,

$$\Delta \equiv \left(\frac{4\pi}{3}n\lambda_D^3\right)^{-1}, \tag{2.26}$$

where n is the mean particle density and λ_D is the Debye length. Since the discreteness parameter Δ becomes extremely small parameter, $\sim 10^{-10}$, for typical fusion plasma parameters, we can expand the s-particle distribution function with respect to Δ,

$$F_s = F_s^{(0)} + F_s^{(1)} + F_s^{(2)} + \cdots. \tag{2.27}$$

We substitute this expression to the BBGKY hierarchy equations (2.25) and leave only the lowest order terms to obtain

$$\left[\frac{\partial}{\partial t}+\sum_{i}^{s}\mathcal{L}(i)-\sum_{i\neq j}^{s}\mathcal{V}(i,j)\right]F_{s}^{(0)}(1,\cdots,s)$$
$$=\sum_{i}^{s}\int d\mathbf{X}_{s+1}\mathcal{V}(i,s+1)F_{s+1}^{(0)}(1,\cdots,s,s+1). \tag{2.28}$$

In order to truncate the hierarchy equations, we introduce an ansatz that $F_s^{(0)}$ is expressed in a form of a product of single particle distribution functions,

$$F_{s}^{(0)}(1,\cdots,s)=\prod_{i}^{s}\left[nf(i)\right], \tag{2.29}$$

where $f(i)$ is the normalized single-particle distribution function. Substituting this relation into Eq.(2.21), we have an equation for $f(i)$,

$$\left[\frac{\partial}{\partial t}+\mathcal{L}(1)-\sum_{j=2}^{s}\mathcal{V}(1,j)\right]f(1)=n\int d\mathbf{X}_{2}\mathcal{V}(1,2)f(1)f(2). \tag{2.30}$$

Writing $\mathcal{L},\mathcal{V}$ and the simplified notations $1,2,\cdots$, explicitly, this equation is rewritten as

$$\left[\frac{\partial}{\partial t}+\mathbf{v}_{1}\cdot\frac{\partial}{\partial\mathbf{x}_{1}}-\frac{q^{2}n}{m}\int d\mathbf{X}_{2}\left(\frac{\partial}{\partial\mathbf{x}_{1}}\frac{f(\mathbf{x}_{2},\mathbf{v}_{2})}{|\mathbf{x}_{1}-\mathbf{x}_{2}|}\right)\cdot\frac{\partial}{\partial\mathbf{v}_{1}}\right]f(\mathbf{x}_{1},\mathbf{v}_{1})$$
$$=\frac{q^{2}}{m}\sum_{j=2}^{s}\left(\frac{\partial}{\partial\mathbf{x}_{1}}\frac{1}{|\mathbf{x}_{1}-\mathbf{x}_{j}|}\right)\cdot\frac{\partial}{\partial\mathbf{v}_{1}}f(\mathbf{x}_{1},\mathbf{v}_{1}). \tag{2.31}$$

The right hand of eq.(2.31) represents the many particle correlation which corresponds to the collision operator. A small discreteness parameter of fusion plasmas $\Delta\sim10^{-10}$ enables a description in the Vlasov limit [65], where the individuality of the particles is suppressed. The Vlasov limit or the fluid limit is introduced by taking the limit $m\to0,q\to0,n\to\infty$, remaining $q/m,nq$ as constant. In this limit, the collision operator is eliminated and the Vlasov equation is obtained,

$$\left[\frac{\partial}{\partial t}+\mathbf{v}_{1}\cdot\frac{\partial}{\partial\mathbf{x}_{1}}-\frac{q^{2}n}{m}\int d\mathbf{X}_{2}\left(\frac{\partial}{\partial\mathbf{x}_{1}}\frac{f(\mathbf{x}_{2},\mathbf{v}_{2})}{|\mathbf{x}_{1}-\mathbf{x}_{2}|}\right)\cdot\frac{\partial}{\partial\mathbf{v}_{1}}\right]f(\mathbf{x}_{1},\mathbf{v}_{1})=0. \tag{2.32}$$

The Vlasov equation (2.32) is recognized as a conservation law of f along the characteristics in the six-dimensional phase space. Consequently, the Vlasov-Maxwell system is the Hamiltonian system. The Hamiltonian structure of the Vlasov-Maxwell system is advantageous in studying the perturbation theory and performing a nonlinear simulation.

2.3 Gyrokinetic model

In this section, the derivation of the gyro-phase averaged Vlasov-Maxwell equations using the Lagrangian formalism [5] is shown.

Let us consider a charged particle motion in a strong background magnetic field with an electrostatic fluctuation. For describing a charged particle motion in a strong magnetic field, it is convenient to use the non-canonical coordinates, so-called the gyro-center coordinates, $\mathbf{z}=(t;\mathbf{R},v_z,M,\theta)$, where $\mathbf{R}$ is the position of guiding center; $v_z=\mathbf{v}\cdot\mathbf{b}$; $v_\perp=|\mathbf{v}\times\mathbf{b}|$; M is defined as $M\equiv mv_\perp^2/2\Omega$; $\Omega=qB_0/mc$; m and q are the mass and charge of particles, respectively; c is the velocity of light; the gyro-phase angle is given by $\theta\equiv\tan^{-1}(\mathbf{v}\cdot\mathbf{e}_1/\mathbf{v}\cdot\mathbf{e}_2)$ and $\mathbf{e}_1$, $\mathbf{e}_2$ are the unit vector in the x- and y-directions. In this formulation, we consider a sheared slab geometry. Here, in addition to the uniform magnetic field $\mathbf{B}_0=B_0\mathbf{b}$ in the z-direction, the finite sheared magnetic field $B_1(x)$ is imposed in the y-direction. $B_1/B_0\sim\mathcal{O}(\epsilon)$ is assumed for describing tokamak plasmas. In this configuration, the fundamental one-form of a perturbed single particle motion in the canonical coordinates $(t;\mathbf{x},\mathbf{v})$ is given by

$$\gamma\equiv\left[\frac{q}{c}\mathbf{A}_0(\mathbf{x})+\frac{q}{c}A_z(\mathbf{x})\mathbf{b}+m\mathbf{v}\right]\cdot d\mathbf{x}-\left[\frac{1}{2}mv^2+q\phi(\mathbf{x},t)\right]dt, \tag{2.33}$$

where ϕ is the perturbed electrostatic potential, and $\mathbf{A}_0$ and $A_z(x)\mathbf{b}$ are the vector potentials describing $\mathbf{B}_0$ and $\mathbf{B}_1$, respectively. In general, a transformation to the gyro-center coordinates is performed using the Darboux transformation [47]. However, in the present case with the uniform background field $\mathbf{B}_0$, the transformation is done by using a simple gauge transformation, in which a gauge scalar is chosen as $-(mv_\perp/B_0)\mathbf{A}_0\cdot[\cos\theta\mathbf{e}_1-\sin\theta\mathbf{e}_2]$. We then obtain the fundamental one-form in the gyro-center coordinates as

$$\gamma_0 = \frac{q}{c}\mathbf{A}_0\cdot d\mathbf{R}_\perp+mv_z dR_z+Md\theta-h_0dt, \tag{2.34}$$
$$\gamma_1 = \frac{q}{c}A_z(\mathbf{R}+\rho)dR_z-h_1dt, \tag{2.35}$$

and the Hamiltonians h_0, h_1 are

$$h_0 = M\Omega+\frac{1}{2}mv_z^2, \tag{2.36}$$
$$h_1 = q\phi(\mathbf{R}+\rho,t), \tag{2.37}$$

where $\rho = \mathbf{b} \times \mathbf{v}/\Omega$ and $\mathbf{R}_\perp$ denotes the coordinate vector in the perpendicular direction to $\mathbf{b}$. Since the wavenumbers and frequency of the low frequency fluctuation, or the characteristic scale lengths in tokamak plasmas can be specified, we analyze a charged particle motion with Eqs. (2.34)-(2.37), under the usual gyrokinetic ordering: $\omega/\Omega \sim k_\parallel/k_\perp \sim q\phi/T \sim \rho/L_n \sim \mathcal{O}(\epsilon)$, where ω is the characteristic frequency of the fluctuation, $k_\parallel$ and $k_\perp$ are the wavenumbers in the parallel and perpendicular directions to $\mathbf{b}$, T is the temperature, and L_n is the characteristic scale length of the density gradient. The unperturbed particle motion described by the Euler-Lagrange equation of Eq. (2.34) involves the fast periodic motion about θ, the gyration of a particle. We consider to transform the fundamental one-form, Eqs. (2.34)-(2.37), to the system where the θ-dependent non-secular perturbation does not exist by using the non-canonical Lie transform. The first order Lie transform [47, 48] is

$$\bar{\Gamma}_0 = \gamma_0, \tag{2.38}$$

$$\bar{\Gamma}_1 = dS_1 - L_1\gamma_0 + \gamma_1, \tag{2.39}$$

$$(L_1\gamma_0)_\nu = g_1^\mu(\partial_\nu\gamma_{0\mu} - \partial_\mu\gamma_{0\nu}), \tag{2.40}$$

where $\bar{\Gamma}$ is the fundamental one-form in the new coordinate system. Under the gyrokinetic ordering, the generating function S_1 and the generator g_1^μ of the first order Lie transform are solved as:

$$S_1 = \frac{q}{\Omega}\int^\theta \tilde{\Psi}(\mathbf{R}+\rho,t)d\theta', \tag{2.41}$$

$$\tilde{\Psi} = \Psi - \langle\Psi\rangle_\theta, \tag{2.42}$$

$$g_1^{\mathbf{R}} = \frac{c}{qB_0}\nabla_{\mathbf{R}}S_1\times\mathbf{b} - \frac{1}{m}\frac{\partial S_1}{\partial v_z}\mathbf{b}, \tag{2.43}$$

$$g_1^{v_z} = \frac{1}{m}\mathbf{b}\cdot\nabla_{\mathbf{R}}S_1 + \frac{q}{mc}\tilde{A}_z, \tag{2.44}$$

$$g_1^M = \frac{\partial S_1}{\partial\theta}, \tag{2.45}$$

$$g_1^\theta = -\frac{\partial S_1}{\partial M}, \tag{2.46}$$

where $\langle\cdot\rangle_\theta$ denotes a θ-independent part of a quantity, $\tilde{A}_z = A_z - \langle A_z\rangle_\theta$ is the θ-dependent part of A_z, and $\Psi \equiv \phi - v_z A_z/c$ is a generalized potential. It is noted that in an electrostatic

model, the θ-dependence of the shear magnetic field $\mathbf{B}_1 = \nabla\times A_z\mathbf{b}$ is often ignored ($\tilde{A}_z = 0$) because of the tokamak ordering $B_1/B_0 \sim \mathcal{O}(\epsilon)$. We then find the fundamental one-form in the gyro-averaged coordinates, $\bar{\mathbf{Z}} = (t;\bar{\mathbf{R}},\bar{v}_z,\bar{M},\bar{\theta})$,

$$\bar{\Gamma} = \frac{q}{c}\mathbf{A}_0\cdot d\bar{\mathbf{R}}_\perp + [\langle A_z\rangle_{\bar{\theta}} + m\bar{v}_z]\,d\bar{R}_z + \bar{M}d\bar{\theta} - \bar{h}dt, \tag{2.47}$$

where the gyro-phase averaged Hamiltonian is

$$\bar{h} = \bar{M}\Omega + \frac{1}{2}m\bar{v}_z^2 + q\langle\phi\rangle_{\bar{\theta}}. \tag{2.48}$$

Relations between the non-vanishing components of the Poisson tensor in the gyro-center coordinates $\mathbf{z}$ and those in the gyro-averaged coordinates $\bar{\mathbf{Z}}$ are calculated as

$$\{R_x,R_y\} = \{\bar{R}_x,\bar{R}_y\} = \frac{c}{eB_0}, \tag{2.49}$$

$$\{R_z,v_z\} = \{\bar{R}_z,\bar{v}_z\} = \frac{1}{m_e}, \tag{2.50}$$

$$\{M,\theta\} = \{\bar{M},\bar{\theta}\} = -1, \tag{2.51}$$

where $\{,\}$ denotes the Poisson bracket. Since the Poisson tensor possesses a form invariance, the area preserving property of the Hamiltonian system is kept in this transformation. Also, the Jacobian of the gyro-center coordinates, D, and the gyro-averaged coordinates, $\bar{D}$, are given as $D = \bar{D} = |qmB_0/c|$. By calculating the Euler-Lagrange equations $\dot{\bar{Z}}_\mu = (\partial_\mu\bar{\Gamma}_\nu - \partial_\nu\bar{\Gamma}_\mu)^{-1}(\partial_t\bar{\Gamma}_\nu - \partial_\nu\bar{h})$, we obtain equations of motion in the gyro-averaged coordinates:

$$\frac{d\bar{\mathbf{R}}}{dt} = \frac{c}{B_0}\mathbf{b}\times\nabla_{\bar{\mathbf{R}}}\langle\phi\rangle_{\bar{\theta}} + \frac{\bar{v}_z}{B_0}\langle\mathbf{B}\rangle_{\bar{\theta}}, \tag{2.52}$$

$$\frac{d\bar{v}_z}{dt} = -\frac{q}{mB_0}\langle\mathbf{B}\rangle_{\bar{\theta}}\cdot\nabla_{\bar{\mathbf{R}}}\langle\phi\rangle_{\bar{\theta}}, \tag{2.53}$$

$$\frac{d\bar{M}}{dt} = 0, \tag{2.54}$$

$$\frac{d\bar{\theta}}{dt} = \Omega + q\frac{\partial\langle\Psi\rangle_{\bar{\theta}}}{\partial\bar{M}}. \tag{2.55}$$

We then have the gyrokinetic equation for the distribution function, $\bar{F}$, in the gyro-averaged coordinates,

$$\frac{\partial\bar{F}}{\partial t} + \left[\frac{c}{B_0}\mathbf{b}\times\nabla_{\bar{\mathbf{R}}}\langle\phi\rangle_{\bar{\theta}} + \frac{\bar{v}_z}{B_0}\langle\mathbf{B}\rangle_{\bar{\theta}}\right]\cdot\nabla_{\bar{\mathbf{R}}}\bar{F} - \frac{q}{mB_0}\langle\mathbf{B}\rangle_{\bar{\theta}}\cdot\nabla_{\bar{\mathbf{R}}}\langle\phi\rangle_{\bar{\theta}}\frac{\partial\bar{F}}{\partial\bar{v}_z} = 0, \tag{2.56}$$

where $\mathbf{B} = \mathbf{B}_0 + \mathbf{B}_1 = \nabla\times\mathbf{A}_0 + \nabla\times A_z\mathbf{b}$. It is noted that, since the Hamiltonian $\bar{h}$ is not a function of $\bar{\theta}$, $\bar{F}$ must be $\bar{\theta}$-independent.

For Eq. (2.56), we impose the consistency condition in the real space, $\mathbf{x}$. From the functional relationship of a scalar function in the Lie transform, the distribution functions $\bar{F}$ in the gyro-averaged coordinates and f in the gyro-center coordinates are related as

$$f(\cdot) = (\mathbf{1} + g^\mu\partial_\mu)\bar{F}(\cdot) + \mathcal{O}(\epsilon^2), \tag{2.57}$$

where $(\cdot)$ denotes dummy arguments. We then have the particle density n in the real space as:

$$\begin{aligned} n(\mathbf{x},t) &= \int f(\mathbf{R},v_z,M,\theta,t)\delta([\mathbf{R}+\rho]-\mathbf{x})Dd^6\mathbf{z} \\ &= \int \bar{F}(\bar{\mathbf{R}},\bar{v}_z,\bar{M},t)\delta([\bar{\mathbf{R}}+\bar{\rho}]-\mathbf{x})\bar{D}d^6\bar{\mathbf{Z}} \\ &\quad + \int\left[\left(\frac{c}{qB_0}\nabla_{\bar{\mathbf{R}}}S_1\times\mathbf{b} - \frac{1}{m}\frac{\partial S_1}{\partial\bar{v}_z}\mathbf{b}\right)\cdot\nabla_{\bar{\mathbf{R}}}\bar{F}\right. \\ &\quad \left. + \left(\frac{1}{m}\mathbf{b}\cdot\nabla_{\bar{\mathbf{R}}}S_1 + \frac{q}{mc}\widetilde{A}_z\right)\frac{\partial\bar{F}}{\partial\bar{v}_z} + \frac{\partial S_1}{\partial\bar{\theta}}\frac{\partial\bar{F}}{\partial\bar{M}}\right]\delta([\bar{\mathbf{R}}+\bar{\rho}]-\mathbf{x})\bar{D}d^6\bar{\mathbf{Z}}. \end{aligned} \tag{2.58}$$

In evaluating the second term in Eq. (2.58), we will linearize the distribution function with a local Maxwellian,

$$F_M(\bar{\mathbf{R}}_x,\bar{v}_z,\bar{M}) = \frac{n_0(\bar{\mathbf{R}}_x)}{[2\pi mT_0(\bar{\mathbf{R}}_x)]^{3/2}}\exp\left[-\frac{\bar{M}\Omega}{T_0(\bar{\mathbf{R}}_x)} - \frac{m\bar{v}_z^2}{2T_0(\bar{\mathbf{R}}_x)}\right], \tag{2.59}$$

where n_0 and T_0 are the background guiding center density and temperature, respectively. With retaining the leading order terms and substituting the generating function (2.41) into Eq. (2.58), we obtain the usual polarization density,

$$\begin{aligned} n(\mathbf{x},t) &= \int \bar{F}(\bar{\mathbf{R}},\bar{v}_z,\bar{M},t)\delta([\bar{\mathbf{R}}+\bar{\rho}]-\mathbf{x})\bar{D}d^6\bar{\mathbf{Z}} \\ &\quad + \frac{n_0}{(2\pi mT_0)^{3/2}}\int\left[-\frac{q}{cT_0}\widetilde{A}_z\bar{v}_z - \frac{q}{T_0}\left(\widetilde{\phi} - \frac{1}{c}\bar{v}_z\widetilde{A}_z\right)\right] \\ &\quad \times\exp\left(-\frac{\bar{M}\Omega}{T_0} - \frac{m\bar{v}_z^2}{2T_0}\right)\delta([\bar{\mathbf{R}}+\bar{\rho}]-\mathbf{x})\bar{D}d^6\bar{\mathbf{Z}} \\ &= \int \bar{F}(\bar{\mathbf{R}},\bar{v}_z,\bar{M},t)\delta([\bar{\mathbf{R}}+\bar{\rho}]-\mathbf{x})\bar{D}d^6\bar{\mathbf{Z}} \\ &\quad - \frac{n_0q}{T_0}\sum_{\mathbf{k}}\left[1 - I_0(k_\perp^2\rho_t^2)\exp(-k_\perp^2\rho_t^2)\right]\phi_{\mathbf{k}}\exp(i\mathbf{k}\cdot\mathbf{x}), \end{aligned} \tag{2.60}$$

where ρ_t is the Larmor radius evaluated with the thermal velocity and I_0 is the zeroth order modified Bessel function. It is noted that, since we are considering electrostatic perturbations, such as drift waves driven by density and temperature gradients, the equilibrium current, which appears as the drift velocity in the local Maxwellian, is ignored, and the sheared magnetic field $\mathbf{B}_1$ is treated as an external field in the present formulation. Finally, the self-consistency condition is imposed with the Poisson equation,

$$-\nabla^2\phi = 4\pi e[n_i(\mathbf{x}) - n_e(\mathbf{x})]. \tag{2.61}$$

Equations (2.56), (2.60) and (2.61) constitute a closed set of equations, which describe the low frequency dynamics of tokamak plasmas.

2.4 Orbit-averaging model

In this section, we present an orbit-averaging model for fast passing electrons, which is formulated under the transit time ordering. The formulation is shown for a limit of the drift-kinetic electrons $\rho_e \to 0$ and the shearless or semi-local case $B_1 \to 0$.

Before introducing the transit time ordering, we briefly discuss the ballistic mode [66]. By taking the drift-kinetic limit of Eq. (2.56), we have the electron drift-kinetic equation in a shearless slab configuration,

$$\frac{\partial\bar{F}_e}{\partial t} + \left[\frac{c}{B_0}\mathbf{b}\times\nabla_{\bar{\mathbf{R}}}\phi + \bar{v}_z\mathbf{b}\right]\cdot\nabla_{\bar{\mathbf{R}}}\bar{F}_e + \frac{e}{m_e}\mathbf{b}\cdot\nabla_{\bar{\mathbf{R}}}\phi\frac{\partial\bar{F}_e}{\partial\bar{v}_z} = 0. \tag{2.62}$$

We linearize the electron distribution function as $\bar{F}_e = \bar{F}_{e0} + \bar{F}_{e1}$ and apply the Fourier-Laplace transform to the perturbed distribution function $\bar{F}_{e1}$ and the perturbed electrostatic potential ϕ. We then have a perturbed distribution function,

$$\bar{F}_{e1p,\mathbf{k}} = \frac{\bar{F}_{e1\mathbf{k}}(t=0)}{p + ik_z\bar{v}_z} + \frac{\left[(c/B_0)\mathbf{b}\times i\mathbf{k}\cdot\nabla_{\bar{\mathbf{R}}}\bar{F}_{e0} + (e/m_e)ik_z(\partial\bar{F}_{e0}/\partial\bar{v}_z)\right]\phi_{p,\mathbf{k}}}{p + ik_z\bar{v}_z}, \tag{2.63}$$

where p is a complex frequency. In Eq. (2.63), the second term shows the contribution from the eigenmode of the system. The first term (the ballistic term) shows a perturbation due to the free streaming of particles. This means that the Vlasov system conserves the

memory of an initial perturbation during the whole time. By taking the inverse Laplace transform of the first term, the perturbation of the ballistic mode is obtained as

$$\bar{F}_{e1B\mathbf{k}}(t) = \bar{F}_{e1B\mathbf{k}}(t=0)\exp(-ik_z\bar{v}_z t). \tag{2.64}$$

The contribution of $\bar{F}_{e1B}$ to the Poisson equation vanishes as $t \to \infty$ because of the phase mixing; therefore, the ballistic term is not often considered in the linear analysis. However, in a simulation which solves the initial value problem directly, the system will inevitably contain the ballistic mode. From the comparison of the transit time τ_{tr} to the characteristic time scale of the low frequency fluctuation (e.g., the Alfvén time τ_A), we have the following relation:

$$\frac{\tau_A}{\tau_{tr}} = \frac{v_{te}}{v_A} \sim \left(\frac{m_i}{m_e}\beta\right)^{1/2}, \tag{2.65}$$

where τ_{tr} is evaluated with the electron thermal velocity v_{te} and β is the plasma beta. For the case $\beta \sim 5\%$, τ_A/τ_{tr} becomes ~ 10. Although the ballistic mode plays no important roles in the low frequency physics in fusion plasmas, the electron ballistic mode arising from the high energy electrons determines the Courant-Friedlichs-Lewy (CFL) condition of the simulation system. In order to reduce the computational cost of the global gyrokinetic particle simulation with drift-kinetic electrons, we eliminate the ballistic mode analytically by applying a secular perturbation theory to the high energy transit electron. We separate the time scale of the low frequency fluctuation and the transit motion of the high energy electrons by introducing the transit time ordering $\omega/\omega_{tr} \sim \mathcal{O}(\epsilon)$, where $\omega_{tr} = k_z v_{te}$. Since, in the orbit analysis of the high energy transit electron, the adiabatic change is assumed for the low frequency fluctuation of the eigenmode, the Z-dependent non-secular perturbation is averaged over the unperturbed orbit. Consequently, the ignorable coordinate, Z, and the corresponding adiabatic invariant appear in the perturbed orbit. In the averaging transformation, we adopt the action variational Lie perturbation method as in the gyrokinetic theory.

Let us consider the high energy electron to which we apply the transit time ordering. By taking the limit of $\rho_e \to 0$ and $A_z \to 0$ in Eqs. (2.47) and (2.48), we have the fundamental

one-form for the electron in the gyro-averaged coordinates,

$$\bar{\Gamma} = -\frac{e}{c}\mathbf{A}_0 \cdot d\bar{\mathbf{R}}_\perp + m_e\bar{v}_z d\bar{R}_z + \bar{M}d\bar{\theta} - \bar{h}dt, \tag{2.66}$$

where the Hamiltonian $\bar{h}$ is

$$\bar{h} = \bar{M}\Omega_e + \frac{1}{2}m_e\bar{v}_z^2 - e\phi. \tag{2.67}$$

By neglecting ϕ in Eqs. (2.66) and (2.67), we obtain equations for the unperturbed orbit,

$$\frac{d\bar{\mathbf{R}}}{dt} = \bar{v}_z\mathbf{b}, \tag{2.68}$$

$$\frac{d\bar{v}_z}{dt} = 0, \tag{2.69}$$

$$\frac{d\bar{M}}{dt} = 0, \tag{2.70}$$

$$\frac{d\bar{\theta}}{dt} = \Omega_e. \tag{2.71}$$

The particle motion in the z-direction is periodic because the periodic boundary condition is imposed in the z-direction. This corresponds to the inherent periodicity in the toroidal system. The unperturbed orbit of the transit electron contains the fast periodic motion in the $\bar{R}_z$-direction. Using the non-canonical Lie transform, the fundamental one-form, Eq. (2.66), is transformed to the orbit-averaged coordinates, $\mathbf{Z} = (t; \mathbf{X}, V, \bar{M}, \bar{\theta})$, where the $\bar{R}_z$-dependent non-secular perturbation is removed. The functional relationship of the first order Lie transform is again given as

$$\Upsilon_0 = \bar{\Gamma}_0, \tag{2.72}$$

$$\Upsilon_1 = d\bar{S}_1 - \bar{L}_1\bar{\Gamma}_0 + \bar{\Gamma}_1, \tag{2.73}$$

$$(\bar{L}_1\bar{\Gamma}_0)_\nu = \bar{g}_1^\mu(\partial_\nu\bar{\Gamma}_{0\mu} - \partial_\mu\bar{\Gamma}_{0\nu}), \tag{2.74}$$

where Υ is the fundamental one-form in the orbit-averaged coordinates. Under the transit time ordering, the generating function $\bar{S}_1$ and the generator $\bar{g}_1^\mu$ of the Lie transform are solved as,

$$\bar{S}_1 = -\sum_{k_z\neq 0}\frac{e}{ik_z\bar{v}_z}\phi_{\mathbf{k}}e^{i\mathbf{k}\cdot\bar{\mathbf{R}}}, \tag{2.75}$$

$$\bar{g}_1^{\bar{\mathbf{R}}} = -\frac{c}{eB_0}\nabla_{\bar{\mathbf{R}}}\bar{S}_1\times\mathbf{b} - \frac{1}{m_e}\frac{\partial \bar{S}_1}{\partial \bar{v}_z}\mathbf{b}, \tag{2.76}$$

$$\bar{g}_1^{\bar{v}_z} = \frac{1}{m_e}\mathbf{b}\cdot\nabla_{\bar{\mathbf{R}}}\bar{S}_1, \tag{2.77}$$

$$\bar{g}_1^{\bar{M}} = 0, \tag{2.78}$$

$$\bar{g}_1^{\bar{\theta}} = 0. \tag{2.79}$$

We then have the fundamental one-form Υ and the Hamiltonian $\mathcal{H}$ in the orbit-averaged coordinates,

$$\Upsilon = -\frac{e}{c}\mathbf{A}_0\cdot d\mathbf{X}_\perp + m_e V dZ + \bar{M}d\bar{\theta} - \mathcal{H}dt, \tag{2.80}$$

$$\mathcal{H} = \bar{M}\Omega_e + \frac{1}{2}m_e V^2 - e\langle\phi\rangle_Z, \tag{2.81}$$

where $\langle\cdot\rangle_Z$ denotes a Z-independent quantity. Also for the fundamental one-forms, Eqs. (2.66) and (2.80), the non-vanishing components of the Poisson tensor are calculated as

$$\{\bar{R}_x, \bar{R}_y\} = \{X, Y\} = \frac{c}{eB_0}, \tag{2.82}$$

$$\{\bar{R}_z, \bar{v}_z\} = \{Z, V\} = \frac{1}{m_e}, \tag{2.83}$$

$$\{\bar{M}, \bar{\theta}\} = -1, \tag{2.84}$$

where the Jacobian of the orbit-averaged coordinates is $\mathcal{D}_e = \bar{D}_e = |em_eB_0/c|$. Consequently, the transformation to the orbit-averaged coordinates is also the area preserving transform. The Euler-Lagrange equations of the fundamental one-form, Eq. (2.80), are

$$\frac{d\mathbf{X}_\perp}{dt} = \frac{c}{B_0}\mathbf{b}\times\nabla_{\mathbf{X}_\perp}\langle\phi\rangle_Z, \tag{2.85}$$

$$\frac{dZ}{dt} = V\mathbf{b}, \tag{2.86}$$

$$\frac{dV}{dt} = 0, \tag{2.87}$$

$$\frac{d\bar{M}}{dt} = 0, \tag{2.88}$$

$$\frac{d\bar{\theta}}{dt} = \Omega_e - e\frac{\partial\langle\phi\rangle_{\bar{\theta}}}{\partial\bar{M}}. \tag{2.89}$$

Like the symmetry about $\bar{\theta}$ in the gyrokinetic system, this system has another symmetry about Z; therefore, the momentum in the Z-direction is also an adiabatic invariant in the orbit-averaged coordinates. The change of velocity due to an adiabatic response to

the low frequency fluctuation is absorbed in the generator (2.77) and is proportional to the amplitude of $k_z \neq 0$ component of the electrostatic potential. Accordingly, when the instability is weak, the high energy electrons remain in the same region of velocity space during the whole simulation time. From equations of motion (2.85)-(2.89), we obtain the orbit-averaged drift-kinetic equation,

$$\frac{\partial\mathcal{F}_e}{\partial t} + \frac{c}{B_0}\mathbf{b}\times\nabla_{\mathbf{X}\perp}\langle\phi\rangle_Z\cdot\nabla_{\mathbf{X}\perp}\mathcal{F}_e = 0, \tag{2.90}$$

where $\mathcal{F}_e$ is the electron distribution function in the orbit-averaged coordinates. Since the Hamiltonian $\mathcal{H}$ is Z-independent, the $\partial\mathcal{F}_e/\partial Z$ term does not appear in Eq. (2.90) and the problem reduces to a two-dimensional problem which involves only the $E\times B$ nonlinearity.

The self-consistency condition for this equation system is also imposed in the real space $\mathbf{x}$. By using the functional relationship of a scalar function in the Lie transform, the high energy part of the electron distribution function in the gyro-averaged coordinates, $\bar{F}_e$, takes the form:

$$\bar{F}_e(\cdot) = (\mathbf{1} + \bar{g}^\mu\partial_\mu)\mathcal{F}_e(\cdot) + \mathcal{O}(\epsilon^2). \tag{2.91}$$

Substituting Eq. (2.91) into the electron density, Eq. (2.58), we have

$$\begin{aligned} n_e(\mathbf{x},t) = &\int_L \bar{F}_e(\bar{\mathbf{R}},\bar{v}_z,\bar{M},t)\delta(\bar{\mathbf{R}}-\mathbf{x})\bar{D}_e d^6\bar{\mathbf{Z}} \\ &+\int_H \mathcal{F}_e(\mathbf{X}_\perp,V,\bar{M},t)\delta(\mathbf{X}-\mathbf{x})\mathcal{D}_e d^6\mathbf{Z} \\ &+\int_H\left[-\frac{c}{eB_0}\nabla_{\mathbf{X}}\bar{S}_1\times\mathbf{b}\cdot\nabla_{\mathbf{X}\perp}\mathcal{F}_e\right. \\ &\left.+\frac{1}{m_e}\mathbf{b}\cdot\nabla_{\mathbf{X}}\bar{S}_1\frac{\partial\mathcal{F}_e}{\partial V}\right]\delta(\mathbf{X}-\mathbf{x})\mathcal{D}_e d^6\mathbf{Z} + \mathcal{O}(\epsilon^2), \end{aligned} \tag{2.92}$$

where the electron polarization density vanishes in the drift-kinetic limit. In Eq. (2.92), the first term is the contribution from the low energy part of the electron distribution function [which is determined by Eq. (2.62)] and the other terms show the contribution from the high energy electrons. As in the case of the ion polarization density, the third term is evaluated with the local Maxwellian;

$$n_e(\mathbf{x},t) = \int_L \bar{F}_e\delta(\bar{\mathbf{R}}-\mathbf{x})\bar{D}_e d^6\bar{\mathbf{Z}} + \int_H \mathcal{F}_e\delta(\mathbf{X}-\mathbf{x})\mathcal{D}_e d^6\mathbf{Z} + \frac{en_{0e}}{T_{0e}}N_\phi\left(\phi - \langle\phi\rangle_Z\right), \tag{2.93}$$

$$N_\phi = \sqrt{\frac{m_e}{2\pi T_e}}2\int_{V_{eL}}^{\infty}\exp\left[-\frac{m_eV^2}{2T_e}\right]dV, \tag{2.94}$$

where n_{0e} and T_{0e} denote the local background electron density and electron temperature respectively, and V_{eL} is the threshold velocity where the high and low energy part of the electron distribution function are separated. In Eq. (2.93), the third term represents the adiabatic response of the high energy electrons to the fluctuating electric field. This is shown clearly by taking the limit $V_{eL} \to 0$. In this limit, we can see that this renormalized term reduces to the usual adiabatic approximation, $en_{0e}/T_{0e}(\phi - \langle\phi\rangle_Z)$. Eqs. (2.56), (2.60), (2.61), (2.62), (2.90), and (2.93) constitute a closed set of equations in which the ballistic mode arising from the high energy transit electron is removed. Here, the threshold velocity, V_{eL}, must be chosen carefully in order to correctly incorporate the wave-particle resonant interaction or the particle trapping effect.

2.5 Energy conservation

In this section, the energy conservation property [67] of the gyrokinetic Vlasov-Maxwell system is derived by using an inherent nature of the Hamiltonian system. Let us consider the Hamiltonian H of a single particle motion in a coordinate system $\mathbf{z}$. The particle density Ω in the phase space is written in the differential form as

$$\Omega = fDd^6\mathbf{z}, \tag{2.95}$$

where D is the Jacobian of the coordinate system $\mathbf{z}$. The Vlasov equation is written as

$$\frac{d}{dt}\Omega = \partial_t\Omega + L_g\Omega = 0, \tag{2.96}$$

where L_g is the Lie derivative along the vector field ${g_h}^\mu$ generated by equations of motion. The change of the energy in a volume element Ω along its characteristics is given as

$$\begin{aligned}\frac{d(H\Omega)}{dt} &= \frac{dH}{dt}\Omega + H\frac{d\Omega}{dt} \\ &= \partial_t(H)fDd^6\mathbf{z}.\end{aligned} \tag{2.97}$$

In another notation, Eq. (2.97) is written as

$$\begin{aligned}\frac{d(H\Omega)}{dt} &= \partial_t(H\Omega) + L_g(H\Omega) \\ &= \partial_t(Hf)Dd^6\mathbf{z} + \partial_\mu({g_h}^\mu HfD)d^6\mathbf{z}.\end{aligned} \tag{2.98}$$

Combining Eqs. (2.97) and (2.98), we obtain the following equality

$$H\partial_t f D d^6\mathbf{z} = -\partial_\mu({g_h}^\mu HfD)d^6\mathbf{z}. \tag{2.99}$$

Eq. (2.99) is integrated over the whole phase space to obtain the conservation law in the Hamiltonian system,

$$\int H(\mathbf{z},t)\partial_t f(\mathbf{z},t)Dd^6\mathbf{z} = 0. \tag{2.100}$$

By applying Eq. (2.100) to the gyrokinetic Vlasov-Maxwell system, Eqs. (2.56), (2.60), and (2.61), we derive the energy conservation law in the total system

$$\sum_s \left[\frac{d}{dt}\int \frac{1}{2}m_s\bar{v}_z^2\bar{F}_s\bar{D}_s d^6\bar{\mathbf{Z}} + \int q_s\langle\phi\rangle_{\bar{\theta}}\partial_t\bar{F}_s\bar{D}_s d^6\bar{\mathbf{Z}}\right] = 0, \tag{2.101}$$

where s denotes the particle species, and the contribution from the adiabatic invariant, $\bar{M}$ is omitted for simplicity. Using an expression for the particle density, Eq. (2.60), and the Poisson equation, Eq. (2.61), the field energy e_ϕ is calculated as

$$\begin{aligned}\frac{de_\phi}{dt} &= \sum_s \int q_s\langle\phi\rangle_{\bar{\theta}}\partial_t\bar{F}_s\bar{D}_s d^6\bar{\mathbf{Z}} \\ &= \frac{d}{dt}\frac{1}{8\pi}\sum_{\mathbf{k}}\left[k^2|\phi_{\mathbf{k}}|^2 + \sum_s\sum_{\mathbf{k}'}\left\{1 - I_0(k'^2_\perp\rho_{ts}^2)\exp(-k'^2_\perp\rho_{ts}^2)\right\}\phi_{\mathbf{k}}\phi^*_{\mathbf{k}'}\right].\end{aligned} \tag{2.102}$$

Finally, we derive a convenient form of the energy conservation law as

$$\begin{aligned}\frac{d}{dt}\sum_s\left[\int\frac{1}{2}m_s\bar{v}_z^2\bar{F}_s\bar{D}_s d^6\bar{\mathbf{Z}} + \frac{1}{8\pi}\sum_{\mathbf{k}}\sum_{\mathbf{k}'}\left\{1 - I_0(k'^2_\perp\rho_{ts}^2)\exp(-k'^2_\perp\rho_{ts}^2)\right\}\phi_{\mathbf{k}}\phi^*_{\mathbf{k}'}\right] \\ + \frac{d}{dt}\frac{1}{8\pi}\int|\nabla\phi|^2 d^3\mathbf{x} = 0.\end{aligned} \tag{2.103}$$

A similar energy conservation law is also derived for the new gyrokinetic Vlasov-Maxwell system including the orbit-averaged electron drift-kinetic equation, Eqs. (2.56), (2.60), (2.61), (2.62), (2.90), and (2.93). By omitting a contribution from the new adiabatic invariant V, we write the energy conservation law as

$$\begin{aligned}&\frac{d}{dt}\int\frac{1}{2}m_i\bar{v}_z^2\bar{F}_i\bar{D}_i d^6\bar{\mathbf{Z}} + \frac{d}{dt}\int_L\frac{1}{2}m_e\bar{v}_z^2\bar{F}_e\bar{D}_e d^6\bar{\mathbf{Z}} \\ &+\frac{d}{dt}\frac{1}{8\pi}\sum_{\mathbf{k}}\sum_{\mathbf{k}'}\left\{1 - I_0(k'^2_\perp\rho_{ti}^2)\exp(-k'^2_\perp\rho_{ti}^2)\right\}\phi_{\mathbf{k}}\phi^*_{\mathbf{k}'} \\ &+\frac{d}{dt}\frac{1}{8\pi}\int\frac{N_\phi}{\lambda_{De}^2}|\phi - \langle\phi\rangle_Z|^2 d^3\mathbf{x} + \frac{d}{dt}\frac{1}{8\pi}\int|\nabla\phi|^2 d^3\mathbf{x} = 0.\end{aligned} \tag{2.104}$$

2.6 Discussion

In this chapter, we have discussed about a treatment of disparate time scales involved in the Vlasov-Maxwell system. This problem becomes crucial especially in the nonlinear simulation which solves an initial value problem. In order to resolve this difficulty, the gyro-motion (and the transit motion) of charged particles, which determines the CFL condition of the simulation, is eliminated analytically by using the non-canonical Lie perturbation method. Also, the gyrokinetic Vlasov-Maxwell equations (with the orbit-averaged drift-kinetic equation for high energy electrons) are formulated. This equation system has the following properties: (a) the system conserves the Hamiltonian structure of the dynamics of the collisionless plasma, (b) the gyro-motion (and the transit motion) of charged particles and the corresponding resonance and ballistic mode are removed analytically, (c) the polarization (and adiabatic) response is renormalized in the particle density, and important physics such as the FLR effect (and the $E \times B$ nonlinearity) is retained. Hence, the CFL condition of the simulation is relaxed and a low cost computation is enabled without losing the important physical effects.

In the former work [49], a gyrokinetic PIC simulation with a time step of $\sim \Omega_i^{-1}$ was reported, and the efficiency of the model was validated. Also, in Ref. [59], we have developed a new gyrokinetic PIC code using the orbit-averaging model. And, a reduction of about 70% of the computational cost has been achieved in a test simulation of the universal mode.

Although we have applied the non-canonical Lie perturbation method only to the treatment of the gyro-motion and transit motion of charged particles, this technique is quite general. We can apply this technique to the analysis of any kind of particle orbits, provided that the unperturbed orbit is well understood. A similar treatment can also be applied to the bounce motion of trapped particles in the toroidal case [68], because the unperturbed orbit of the trapped particles has a periodicity and the bounce frequency is also much higher than the eigenfrequency of low frequency waves. Thus, the orbit averaging model provides many promising features towards the global gyrokinetic particle simulation including the drift-kinetic electrons.

Chapter 3

Slab ion temperature gradient driven mode

3.1 Introduction

In this chapter, we will clarify various stabilizing or destabilizing mechanisms of the slab ITG mode in the negative-sheared slab configuration modeling the ITB of negative shear tokamaks. As is mentioned in Chapter 1, the ITB region is characterized by a weak or zero magnetic shear and steep density and temperature gradients, where a WKB approach is inappropriate. Basically, the eigenmode structure and the corresponding eigenvalue are determined by the balance between the destabilizing and stabilizing contributions, which are related to the equilibrium profiles. For a proper treatment of these contributions, it is required to solve the integral eigenmode equation without using any assumption among scale lengths of an eigenmode structure and equilibrium profiles. To this end, we have developed a gyrokinetic integral eigenvalue code [60], which involves full kinetic effects of ions and electrons. From numerical results, it is found that a combination of the negative shear configuration and the steep ion temperature gradient produces unique features of the negative-sheared slab ITG (NS-ITG) mode [60]. Also, it is shown that modes which appear in the high-$k_\perp$ region with $k_\perp \rho_{ti} > 1$, the kinetic responses of ions and electrons, and the asymmetric FLR effect due to the steep ion temperature gradient play a significant

role in the linear stability of the NS-ITG modes. These effects were ignored in the previous works [69, 70], in which the slab ITG mode in the negative shear configuration has been studied using the fluid type linear eigenmode equation and the corresponding WKB shooting code [71].

In our analytical and numerical analyses, a slab geometry is used as a model configuration. In the framework of the ballooning representation [12], the magnetic drift frequency is written as $\omega_D = 2\epsilon_n\omega_i^*[(v_\parallel^2 + v_\perp^2/2)/v_{ti}^2)](\cos\theta_b + \hat{s}\theta_b \sin\theta_b)$, where $\epsilon_n = L_n/R$ (R is the major radius), $\hat{s} = rq'/q$ (q is the safety factor), ω_i^* is the ion diamagnetic frequency, $v_\parallel$ and $v_\perp$ are the velocities parallel and perpendicular to the ambient magnetic field, respectively, v_{ti} is the ion thermal velocity, and θ_b is the ballooning angle. Here, the contribution from the second term disappears in a small magnetic shear region [32]. From the comparison between the average magnetic drift frequency, $\langle\omega_D\rangle \sim 2\epsilon_n\omega_i^*$, and a typical frequency of the ITG mode, $\omega \sim \omega_{ti}^*$ ($\omega_{ti}^* = \eta_i\omega_i^*$), we have a relation, $\langle\omega_D\rangle/\omega \sim 2\epsilon_{ti}$, where $\eta_i = L_n/L_{ti}$ and $\epsilon_{ti} = L_{ti}/R$. If we assume a steep ion temperature gradient as in the ITB region, this relation yields $\langle\omega_D\rangle/\omega \ll 1$. Consequently, a driving effect due to the magnetic drift tends to become weak for configurations considered in the present analysis. In addition, the toroidal mode coupling is weak in a small magnetic shear region around the $q_{\min}$-surface. Hence, although it may be significant to treat full toroidal effects for a quantitative evaluation of a growth rate and a stability limit, we believe that most of features of the NS-ITG modes can be captured in a slab model, and that a slab model is useful for the present analysis. Also, a slab model is advantageous in regard to an analytical treatment of the eigenmode equation, as well as a numerical resolution in solving the gyrokinetic integral eigenmode equation.

Drift waves in the negative shear configuration are characterized by following features: (a) the magnetic shear stabilization disappear around the $q_{\min}$-surface, (b) the variation of the magnetic shear, q'', characterizes an effective potential structure in a Weber type differential eigenmode equation, and (c) a single mode-rational surface mode, a double mode-rational surface mode, and a nonresonant mode appear depending on the number of the mode-rational surfaces. The single mode-rational surface NS-ITG mode corresponds to the weak shear limit [72] of the slab ITG mode. Its property is significantly affected by

a steep ion temperature gradient which produces an asymmetric eigenmode structure with respect to the $q_{\min}$-surface through a variation of the FLR effect. The latter two modes appear only in the negative shear configuration. The properties of these modes are understood by an effective potential structure in a Weber type differential eigenmode equation. For the double mode-rational surface (nonresonant) NS-ITG mode, a parabolic potential well (hill) perturbed by a fourth order potential hill is formed near the $q_{\min}$-surface. Thus, the double mode-rational surface (nonresonant) NS-ITG mode becomes a bounded (oscillatory) solution around the $q_{\min}$-surface, and an asymptotic solution of the NS-ITG mode behaves as the outgoing wave, which has a stabilizing effect on the nonresonant NS-ITG mode (an oscillatory solution). The stability of these modes is determined locally at the $q_{\min}$-surface because $q' \simeq 0$. As a result, the unstable region in the k_y space widely spreads over the high-k_y region with $k_y\rho_{ti} \sim 10$. This is a remarkable feature of the NS-ITG mode clarified by the gyrokinetic integral eigenvalue code which make analyses of micro-instabilities with $k_\perp\rho_{ti} \gg 1$ possible.

3.2 Gyrokinetic integral eigenvalue code

In this section, we derive an integral eigenvalue equation based on the gyrokinetic Vlasov-Maxwell system. We also give a numerical method for solving the linear eigenvalue problem described as a transcendental equation.

In the present study of the ITG mode, we consider a sheared slab geometry, where the x-direction corresponds to the radial direction, the z-direction is chosen in the direction of the magnetic field at $x = 0$, and the y-direction is chosen to be normal to both the x- and z-directions. We assume the periodic boundary condition in the y- and z-directions, and the fixed boundary condition with conducting walls in the x-direction. By expanding the q-profile around the position $x = 0$, we write the q-profile as $q(x) = q_0 + q_0'x + \frac{1}{2}q_0''x^2 + \cdots$, where q_0, q_0' and q_0'' are evaluated at $x = 0$. The corresponding slab magnetic field configuration for the normal shear case with $q_0' \neq 0$ is

$$\mathbf{B}(x) = B_0[\mathbf{e}_z - x/L_s\mathbf{e}_y], \tag{3.1}$$

where $L_s = (q_0^2 R)/(q_0' r_0)$, R is the major radius of a toroidal plasma, r_0 is the minor radius at the position $x = 0$, and $x = 0$ is the position of the mode-rational surface. For the negative shear case with $q_0' = 0$, we choose the model magnetic configuration as

$$\mathbf{B}(x) = B_0[\mathbf{e}_z - (x/L_{ns})^2 \mathbf{e}_y], \tag{3.2}$$

where $L_{ns} = \sqrt{(2q_0^2 R)/(q_0'' r_0)}$, and $x = 0$ corresponds to the position of the $q_{\min}$-surface. Here, it is noted that an inclusion of the first order shear term [70] in Eq. (3.2) just shifts the position of the $q_{\min}$-surface, and changes the minimum value of q from q_0. Thus, only the second order derivative term is retained in Eq. (3.2). In these model configurations, the asymmetry of the configuration which is produced by q_0''' is ignored for simplicity.

By linearizing the gyrokinetic Vlasov-Maxwell system, Eqs. (2.56), (2.60), and (2.61), we obtain the linearized gyrokinetic equations:

$$\frac{\partial \bar{F}_1}{\partial t} + \frac{\bar{v}_z}{B_0}\mathbf{B}\cdot\nabla_{\bar{\mathbf{R}}}\bar{F}_1 + \frac{c}{B_0}\mathbf{b}\times\nabla_{\bar{\mathbf{R}}}\langle\phi\rangle_{\bar{\theta}}\cdot\nabla_{\bar{\mathbf{R}}}\bar{F}_0 - \frac{q}{mB_0}\mathbf{B}\cdot\nabla_{\bar{\mathbf{R}}}\langle\phi\rangle_{\bar{\theta}}\frac{\partial \bar{F}_0}{\partial \bar{v}_z} = 0, \tag{3.3}$$

$$n_1(\mathbf{x}) = \int \bar{F}_1 \delta([\bar{\mathbf{R}} + \bar{\rho}] - \mathbf{x})\bar{D}d^6\bar{\mathbf{Z}} - \frac{qn_0}{T}\sum_{\mathbf{k}}\left[1 - I_0(k_\perp^2\rho_t^2)\exp(-k_\perp^2\rho_t^2)\right]\phi_{\mathbf{k}}\exp(i\mathbf{k}\cdot\mathbf{x}), \tag{3.4}$$

$$-\nabla^2\phi = 4\pi e\left[n_{i1}(\mathbf{x}) - n_{e1}(\mathbf{x})\right], \tag{3.5}$$

where $\bar{F}_0$ is the unperturbed guiding-center distribution function, and $\bar{F}_1$, ϕ are the linear perturbations. In Eq. (3.3), the gyro-average for the sheared magnetic field is ignored because of the scale length ordering, $\rho/L_s \sim \rho/L_{ns} \sim \mathcal{O}(\epsilon)$.

Since the system is symmetric in the y- and z-directions, we assume the $\bar{R}_y$- and $\bar{R}_z$-dependences of a linear perturbation $\bar{F}_1$ as a plane wave with specified k_y and k_z:

$$\bar{F}_1(\bar{\mathbf{R}}, \bar{v}_z, \bar{M}, t) = \bar{F}_1(\bar{R}_x, \bar{v}_z, \bar{M})\exp(ik_y\bar{R}_y + ik_z\bar{R}_z - i\omega t), \tag{3.6}$$

where the time dependence is also assumed as $\exp(-i\omega t)$ with a complex frequency ω. By expanding the radial eigenfunction into a Fourier series, we write a perturbed guiding-center distribution function and an electrostatic potential in a form:

$$\bar{F}_1(\bar{\mathbf{R}}, \bar{v}_z, \bar{M}, t) = \sum_{k_x}\bar{F}_{1k_x}(\bar{v}_z, \bar{M})\exp(ik_x\bar{R}_x + ik_y\bar{R}_y + ik_z\bar{R}_z - i\omega t), \tag{3.7}$$

$$\bar{F}_{1k_x}(\bar{v}_z, \bar{M}) = \frac{1}{2L_x}\int_{-L_x}^{L_x}\bar{F}_1(\bar{R}_x, \bar{v}_z, \bar{M})\exp(-ik_x\bar{R}_x)d\bar{R}_x, \tag{3.8}$$

and

$$\phi(\bar{\mathbf{R}}, t) = \sum_{k_x}\phi_{k_x}\exp(ik_x\bar{R}_x + ik_y\bar{R}_y + ik_z\bar{R}_z - i\omega t), \tag{3.9}$$

$$\langle\phi(\bar{\mathbf{R}} + \bar{\rho}, t)\rangle_{\bar{\theta}} = \sum_{k_x}\phi_{k_x}J_0(k_\perp\bar{\rho})\exp(ik_x\bar{R}_x + ik_y\bar{R}_y + ik_z\bar{R}_z - i\omega t), \tag{3.10}$$

$$\phi_{k_x} = \frac{1}{2L_x}\int_{-L_x}^{L_x}\phi(\bar{R}_x)\exp(-ik_x\bar{R}_x)d\bar{R}_x, \tag{3.11}$$

where L_x denotes the system size in the x-direction. In the Fourier series representation, the gyro-average of a perturbed quantity is written using the zeroth order Bessel function, J_0. By substituting these expressions into Eq. (3.3), we have the perturbed guiding-center distribution function as

$$\bar{F}_1(\bar{R}_x, \bar{v}_z, \bar{M}) = \frac{\omega^*\left[1 - \eta\{\frac{3}{2} - (\bar{M}\Omega + \frac{1}{2}m\bar{v}_z^2)/T\}\right] - k_\parallel\bar{v}_\parallel}{k_\parallel\bar{v}_\parallel - \omega} \times\frac{q}{T}\bar{F}_0\sum_{k_x}\phi_{k_x}J_0(k_\perp\bar{\rho})\exp(ik_x\bar{R}_x), \tag{3.12}$$

where $k_\parallel = \mathbf{k}\cdot\mathbf{B}/B$, $\bar{v}_\parallel = \bar{v}_z B/B_0$, $\eta = d\ln T/d\ln n_0$, and the diamagnetic drift frequency is $\omega^* = (k_y T/m\Omega)(d\ln n_0/d\bar{R}_x)$. Using a local Maxwellian (2.59) for the unperturbed guiding-center distribution function, we obtain the perturbed density from Eq. (3.4):

$$\begin{aligned} n_1(x) &= \frac{1}{2L_x}\sum_{k_x}\sum_{k_x'}\int_{-L_x}^{L_x}dx'\exp(ik_x(x - x') + ik_x'x') \\ &\quad\times\frac{qn_0}{T}\phi_{k_x'}\left[\left\{\Gamma_0 - \eta\left(\frac{1}{2} + b_a\right)\Gamma_0 + \eta b_g\Gamma_1\right\}\xi^* Z + \Gamma_0(\eta\xi^*\xi - 1)(1 + \xi Z)\right] \\ &\quad - \frac{qn_0}{T}\sum_{k_x'}\left[1 - I_0(b')\exp(-b')\right]\phi_{k_x'}\exp(ik_x'x). \end{aligned} \tag{3.13}$$

The definitions of quantities in Eq. (3.13) are given as follows: $Z = Z(\xi)$ is the Fried-Conte plasma dispersion function; $\xi = \omega/(\sqrt{2}|k_\parallel|v_t)$; $\xi^* = \omega^*/(\sqrt{2}|k_\parallel|v_t)$; $b = (k_x^2 + k_y^2)\rho_t^2$; $b' = (k_x'^2 + k_y^2)\rho_t^2$; $b_a = (b + b')/2$, $b_g = \sqrt{bb'}$; $\Gamma_0(b_a, b_g) = \exp(-b_a)I_0(b_g)$; $\Gamma_1(b_a, b_g) = \exp(-b_a)I_1(b_g)$; and I_n is the n-th order modified Bessel function. Finally, by imposing the self-consistency condition or the Poisson equation, Eq. (3.5), in the Fourier space, we derive the linear integral equation for the Fourier amplitude, ϕ_{k_x},

$$\sum_{k_l}\mathcal{L}_{k_m,k_l}(\omega)\phi_{k_l} = 0 \tag{3.14}$$

$$\mathcal{L}_{k_m,k_l}(\omega) \equiv \frac{1}{2L_x}\int_{-L_x}^{L_x} dx \exp[i(k_l-k_m)x]\times\Bigg[-(k_l^2+k_y^2+k_z^2) + \sum_s \frac{1}{\lambda_{Ds}^2}\Bigg[\left\{\Gamma_0-\eta_s\left(\frac{1}{2}+b_{as}\right)\Gamma_0+\eta_s b_{gs}\Gamma_1\right\}\xi_s^* Z_s + \Gamma_0(\eta_s\xi_s^*\xi_s-1)(1+\xi_s Z_s)-\{1-I_0(b_s')\exp(-b_s')\}\Bigg]\Bigg], \quad (3.15)$$

where the notation for k' is changed as k_l, $\mathcal{L}_{k_m,k_l}(\omega)$ are elements of the complex matrix $\mathcal{L}(\omega)$, $\lambda_{Ds}^2 = T_s/(4\pi n_{s0}q_s^2)$, and s denotes the particle species. Thus, the linear stability problem of low frequency micro-instabilities in the sheared magnetic field is formulated as the integral eigenvalue equation. Since our interest is not only in the ITG mode, but also in the short wavelength ETG mode, we have used the general dielectric tensor including the electron kinetic effects in Eq. (3.15).

The matrix form of the integral eigenvalue equation, Eq. (3.14), can be reduced to the problem of finding eigenvalues, $\{\omega_i\}_{i=1,N}$, of the complex matrix $\mathcal{L}$, which satisfy

$$\det\mathcal{L}(\omega_i) = 0. \quad (3.16)$$

In finding a root of Eq. (3.16), first, we plot the contour lines of $\mathrm{Re}(\det\mathcal{L}) = 0$ and $\mathrm{Im}(\det\mathcal{L}) = 0$ in a complex ω-plane, and obtain guesses for the eigenfrequencies, $\{c_i\}_{i=1\cdots N}$, in a region where the eigenfrequency with the maximum growth rate exists. We then refine guesses using a method based on the algorithm developed by Davies [73]. Although the original algorithm can treat multiple roots simultaneously, we apply the algorithm only for a single root case. Let us set a closed positively oriented contour, $C : |\omega - c_i| = r_i$, so that there exists a single root, ω_i, in the region limited by C. Applying the residue theorem, the eigenfrequency, ω_i, is written by the following integral:

$$\omega_i = \frac{1}{2\pi i}\oint_C \omega\frac{g'(\omega)}{g(\omega)}d\omega, \quad (3.17)$$

where $g(\omega) = \det\mathcal{L}(\omega)$. In order to avoid the numerical calculation of $g'(\omega)$, we use integration by parts to estimate Eq. (3.17). Here, since $\ln[g]$ is not single-valued along the contour, C, we rewrite the integral, Eq. (3.17), in the following form:

$$\begin{aligned}\omega_i &= \frac{1}{2\pi i}\oint_C \omega\frac{G'(\omega)}{G(\omega)}d\omega + c_i,\\ &= -\frac{1}{2\pi i}\oint_C \ln[G(\omega)]d\omega + c_i \end{aligned} \quad (3.18)$$

where $G(\omega) = g(\omega)/(\omega - c_i)$, and $\ln[G]$ is single-valued along the contour, C. The integral, Eq. (3.18), is evaluated using a numerical quadrature to obtain the eigenfrequency, ω_i. Finally, the corresponding eigenfunction is solved using the usual inverse iterative method.

As a benchmark test, we have calculated the dispersion relations of micro-instabilities, which were obtained in the other gyrokinetic or Vlasov integral eigenvalue code. And, we have confirmed that our gyrokinetic integral eigenvalue code recovers the eigenfunction and the dispersion relation of the normal-sheared slab ITG mode [74] and the normal-sheared slab ETG mode (the $\beta = 0$ case in Ref. [27]).

3.3 Analytic solutions

Before showing numerical results of the gyrokinetic integral eigenvalue code, we provide an analytical result of the differential eigenmode equation [75, 76] in order to show qualitative characteristics of the NS-ITG mode.

We try an analytical treatment of the gyrokinetic Vlasov-Maxwell system under the ordering for the phase velocity, $v_{ti} < |\mathrm{Re}(\omega)/k_\parallel| \ll v_{te}$. Hence, the differential eigenmode equation is obtained from the quasi-neutrality condition with the gyrokinetic ion response and the adiabatic electron response. We also apply a long perpendicular wavelength approximation, $b_i \sim b_i' \ll 1$, to the ion gyrokinetic response, Eq. (3.13). We then have the second order ordinary differential equation,

$$\frac{\partial^2\tilde{\phi}}{\partial\tilde{x}^2} + Q(\tilde{x})\tilde{\phi} = 0, \quad (3.19)$$

$$Q(\tilde{x}) \equiv -\tilde{k}_y^2 + \tau\frac{\tau+1+\{\tau+1/\tilde{\Omega}-\eta_i/(2\tilde{\Omega})\}\xi_i Z_i + (\eta_i/\tilde{\Omega})\xi_i^2(1+\xi_i Z_i)}{\{\tau+1/\tilde{\Omega}+\eta_i/(2\tilde{\Omega})\}\xi_i Z_i + (\eta_i/\tilde{\Omega})\xi_i^2(1+\xi_i Z_i)}, \quad (3.20)$$

where $\tau \equiv T_e/T_i$, $\rho_s = \sqrt{\tau}\rho_{ti}$, and each variables are normalized as follows: $\tilde{\Omega} \equiv \omega/\omega_e^*$; $\tilde{x} \equiv x/\rho_s$; $\tilde{k}_y \equiv k_y\rho_s$; and $\tilde{\phi} \equiv e\phi/T_e$. Here, it is noted that in this normalization, radial variation of the temperature within an analysis domain is assumed to be weak, $T \sim \bar{T}$, even for a finite η, where $\bar{T}$ is an average temperature. This assumption is valid for a case with relatively weak density and temperature gradients. Using the asymptotic expansion for the plasma dispersion function, $Z_i \sim -\xi_i^{-1} - \frac{1}{2}\xi_i^{-3} - \frac{1}{4}\xi_i^{-5} - \cdots$, under the fluid limit,

$\xi_i > 1$, we have a reduced form of the eigenmode equation [76],

$$\frac{d^2\tilde{\phi}}{d\tilde{x}^2} + \left[-\tilde{k}_y^2 + \frac{1-\tilde{\Omega}}{\tilde{\Omega}+(1+\eta_i)/\tau} + \frac{\tilde{L}_n^2|\tilde{k}_\parallel|^2}{\tilde{k}_y^2\tilde{\Omega}^2}\right]\tilde{\phi} = 0. \tag{3.21}$$

For the normal shear case with $q_0' \neq 0$ or the model magnetic field, Eq.(3.1), the eigenmode equation is rewritten in a form of the well-known Weber equation:

$$\frac{d^2\tilde{\phi}}{d\zeta^2} + (\epsilon - \zeta^2)\tilde{\phi} = 0, \tag{3.22}$$

where

$$\zeta = a\tilde{x}, \quad a = \left(-\frac{\tilde{L}_n^2}{\tilde{L}_s^2\tilde{\Omega}^2}\right)^{1/4}, \quad \epsilon = a^{-2}\left[-\tilde{k}_y^2 + \frac{1-\tilde{\Omega}}{\tilde{\Omega}+(1+\eta_i)/\tau}\right].$$

In Eq. (3.22), $\tilde{k}_z$ is set to zero, because $\tilde{k}_z$ does not affect the stability but just shift the mode-rational surface from $x = 0$. From the bounded solution in the ζ space and the corresponding quantization condition for ϵ, we have the eigenfunction and the dispersion relation as follows,

$$\tilde{\phi}_l(\tilde{x}) = \left[a/\left(\sqrt{\pi}2^l l!\right)\right]^{1/2} H_l(\zeta)\exp(-\zeta^2/2), \tag{3.23}$$

$$\epsilon = 2l+1, \tag{3.24}$$

where l denotes a radial mode number, H_l is the l-th order Hermite polynomials, and the eigenfunction, Eq. (3.23), is normalized as $\int|\tilde{\phi}_l|^2 d\tilde{x} = 1$. If we assume that the eigenfrequency satisfies $|\mathrm{Re}(\tilde{\Omega})| \gg |\mathrm{Im}(\tilde{\Omega})|$, a potential of the Weber equation, Eq. (3.22), is recognized as a parabolic potential hill and the eigenfunction, Eq. (3.23), shows an oscillatory feature in the $\tilde{x}$ space. The asymptotic solution of Eq. (3.22) is then given as

$$\lim_{|x|\to\infty}\tilde{\phi} = C\exp\left(-i\frac{|\tilde{L}_n|}{2\tilde{L}_s\tilde{\Omega}}\tilde{x}^2\right), \tag{3.25}$$

where C is a constant. By comparing Eq. (3.25) with an eikonal form of WKB solution, $\exp(\int\tilde{k}_x d\tilde{x})$, the group velocity is evaluated as

$$\tilde{v}_g = \frac{\partial\tilde{\Omega}}{\partial\tilde{k}_x} = \frac{|\tilde{L}_n|}{\tilde{k}_x^2\tilde{L}_s}\tilde{x}. \tag{3.26}$$

Hence, the asymptotic solution, Eq. (3.25), behaves as the outgoing wave which takes a wave energy away from an unstable region around the mode-rational surface to a stable

region where the wave energy is absorbed by the ion Landau damping. This stabilizing mechanism is so-called the shear convective damping [77].

For the negative shear case with $q_0' = 0$ or the model magnetic field, Eq. (3.2), the eigenmode equation becomes

$$\frac{d^2\tilde{\phi}}{d\zeta^2} + (\epsilon - \zeta^2 - \alpha\zeta^4)\tilde{\phi} = 0, \tag{3.27}$$

where

$$\zeta = a\tilde{x}, \quad a = \left(\frac{2\tilde{k}_z}{\tilde{k}_y}\frac{\tilde{L}_n^2}{\tilde{L}_{ns}^2\tilde{\Omega}^2}\right)^{1/4}, \quad \alpha \equiv -\left(\frac{\tilde{k}_y}{2\tilde{k}_z}\right)^{3/2}\left(\frac{\tilde{\Omega}^2}{\tilde{L}_n^2\tilde{L}_{ns}^2}\right),$$
$$\epsilon = a^{-2}\left[-\tilde{k}_y^2 + \frac{1-\tilde{\Omega}}{\tilde{\Omega}+(1+\eta_i)/\tau} + \frac{\tilde{L}_n^2\tilde{k}_z^2}{\tilde{\Omega}^2\tilde{k}_y^2}\right].$$

By considering α as a perturbation parameter, the perturbation theory [78] can be applied to Eq. (3.27). Solving the perturbed eigenfunction $\tilde{\phi}_l^{(1)}$ and the perturbed energy level $\epsilon_l^{(1)}$ yields the eigenfunction,

$$\tilde{\phi}_l = \tilde{\phi}_l^{(0)} + \tilde{\phi}_l^{(1)}, \tag{3.28}$$

$$\tilde{\phi}_l^{(0)} = \left[a/\left(\sqrt{\pi}2^l l!\right)\right]^{1/2} H_l(\zeta)\exp(-\zeta^2/2), \tag{3.29}$$

$$\tilde{\phi}_l^{(1)} = \sum_{j\neq l}\frac{\epsilon_l^{(1)}}{\epsilon_l^{(0)} - \epsilon_j^{(0)}}\tilde{\phi}_j^{(0)}, \tag{3.30}$$

and the dispersion relation,

$$\epsilon = \epsilon_l^{(0)} + \epsilon_l^{(1)} \tag{3.31}$$

$$\epsilon_l^{(0)} = 2l+1, \tag{3.32}$$

$$\epsilon_l^{(1)} = \int\tilde{\phi}_l^{(0)*}\alpha\zeta^4\tilde{\phi}_l^{(0)}d\tilde{x}, \tag{3.33}$$

where $\tilde{\phi}_l^{(0)*}$ denotes a complex conjugate of $\tilde{\phi}_l^{(0)}$. Equation (3.28) involves two characteristic solutions depending on a relative sign between $\tilde{k}_z$ and $\tilde{k}_y$.

When $\tilde{k}_z > 0$ (and $\tilde{k}_y > 0$), the configuration has two mode-rational surfaces. Again, assuming the case satisfying $|\mathrm{Re}(\tilde{\Omega})| \gg |\mathrm{Im}(\tilde{\Omega})|$, a potential in Eq. (3.27) is recognized as a parabolic potential well with a fourth order perturbation, and the eigenfunction, Eq. (3.28), becomes basically a bounded solution in the $\tilde{x}$ space. Accordingly, the linear

stability problem of the NS-ITG mode with the double mode-rational surfaces is recognized as a harmonic oscillator perturbed by a fourth order potential. In the negative shear configuration with two neighboring mode-rational surfaces at $\tilde{x}_{r\pm} = \pm\sqrt{\tilde{k}_z/\tilde{k}_y}\tilde{L}_{ns}$, a potential well is formed between these mode-rational surfaces, $\tilde{x}_{r-} < \tilde{x} < \tilde{x}_{r+}$. From Eq. (3.28), the width of the eigenfunction is evaluated as $\Delta\tilde{x} \sim a^{-1}$. From a comparison between the width of the eigenfunction and that of the potential well, we obtain a relation, $\Delta\tilde{x}/(\tilde{x}_{r+} - \tilde{x}_{r-}) = \sqrt{\alpha} < 1$, i.e., the eigenfunction, Eq. (3.28), becomes localized within the potential well. Therefore, the stabilizing effect of shear convective damping does not work for the double mode-rational surface NS-ITG mode.

On the other hand, when $\tilde{k}_z < 0$ (and $\tilde{k}_y > 0$), the configuration has no mode-rational surface. For the eigenfrequency with $|\mathrm{Re}(\tilde{\Omega})| \gg |\mathrm{Im}(\tilde{\Omega})|$, a potential function in the eigenmode equation behaves as a parabolic potential hill with a fourth order perturbation. And, the eigenfunction, Eq. (3.28), corresponds to an oscillatory solution. For an unstable mode, the asymptotic solution is written as [69]

$$\lim_{|x|\to\infty} \tilde{\phi} = C \exp\left(-i\frac{|\tilde{L}_n|}{3\tilde{L}_{ns}^2\tilde{\Omega}}|\tilde{x}|^3\right). \tag{3.34}$$

This solution has the group velocity of the outgoing wave:

$$\tilde{v}_g = \frac{\partial\tilde{\Omega}}{\partial\tilde{k}_x} = \frac{|\tilde{L}_n|}{\tilde{k}_x^2\tilde{L}_{ns}^2}\frac{\tilde{x}^3}{|\tilde{x}|}. \tag{3.35}$$

Accordingly, in the nonresonant case, we expect a stabilizing effect of shear convective damping as seen in the conventional slab ITG mode.

3.4 Numerical solutions

Using the gyrokinetic integral eigenvalue code, we have analyzed the ITG modes both in the normal shear case and in the negative shear case. Use of the gyrokinetic integral eigenvalue code enable us to analyze an eigenmode with a long radial correlation length, $k_x\rho_{ti} < 1$, as well as a short perpendicular wavelength mode with $k_\perp\rho_{ti} > 1$, where the full FLR effect becomes significant.

Parameters studied in this section are shown in Table 3.1. The model magnetic configuration is given with $L_s = 2.78\mathrm{m}(L_n/L_s = 0.167)$ for the normal shear case, and

Major radius	R	=	2.6m
$q_{\min}$-surface ($q_{\min} = 2$)	r_0	=	0.3m
Magnetic field	B_0	=	4.6T
Density	$\bar{n}_e$	=	$\bar{n}_i = 2\times10^{19}\mathrm{m}^{-3}$
Density gradient	L_{ne}	=	$L_{ni} = 0.38$m
Electron temperature	$\bar{T}_e$	=	3.91keV
Ion temperature	$\bar{T}_i$	=	12.8keV
Electron Larmor radius	$\bar{\rho}_{te}$	=	0.0325mm
Ion Larmor radius	$\bar{\rho}_{ti}$	=	2.52mm
Ion cycrotron frequency	$\bar{\Omega}_i$	=	440MHz
Electron Debye length	$\bar{\lambda}_{De}$	=	0.104mm

Table 3.1: Description of TFTR like parameters used in analyses. $\bar{\ }$ denotes a quantity averaged over the region of the $q_{\min}$-surface.

$L_{ns} = 0.883$m for the negative shear case. Also, in the present analysis, the non-adiabatic electron response is included for completeness, and its effect on the ITG modes in a high-k_y region is examined. As for a numerical resolution, in order to exclude spurious solutions, we have used 128 modes for the k_x spectrum corresponding to the system size of $L_x = 60.3\bar{\rho}_{ti}$, the grid size of $\Delta x \simeq 0.471\bar{\rho}_{ti}$, and the wavenumber of $k_x\bar{\rho}_{ti} \leq 7$. Also, we have adopted a sine series expansion to satisfy the conducting wall boundary condition in the x-direction.

In Fig. 3.1, typical eigenfunctions of the slab ITG modes are plotted for $\eta_i = \eta_e = 5$, which corresponds to $L_{ti} = L_{te} = 0.076$m. Although this temperature gradient parameter seems to be relatively higher than that observed in the experiment, we have chosen a steep temperature gradient profile in order to clearly see the characteristics of the slab ITG modes. We will discuss about the η_i-dependence of the linear stability later. In the figure, the mode-rational surface, x_r, the ion resonance point, x_i, and the electron resonance point, x_e, are defined as $k_\parallel(x_r) = 0$, $|\mathrm{Re}(\omega)/k_\parallel(x_i)| = v_{ti}$, and $|\mathrm{Re}(\omega)/k_\parallel(x_e)| = v_{te}$, respectively. Figure 3.1(a) shows the eigenfunction of the $l = 0$ branch of the conventional slab ITG mode, which gives the radial correlation length of $\Delta x \sim 4.92\bar{\rho}_{ti}$. Here, the radial correlation

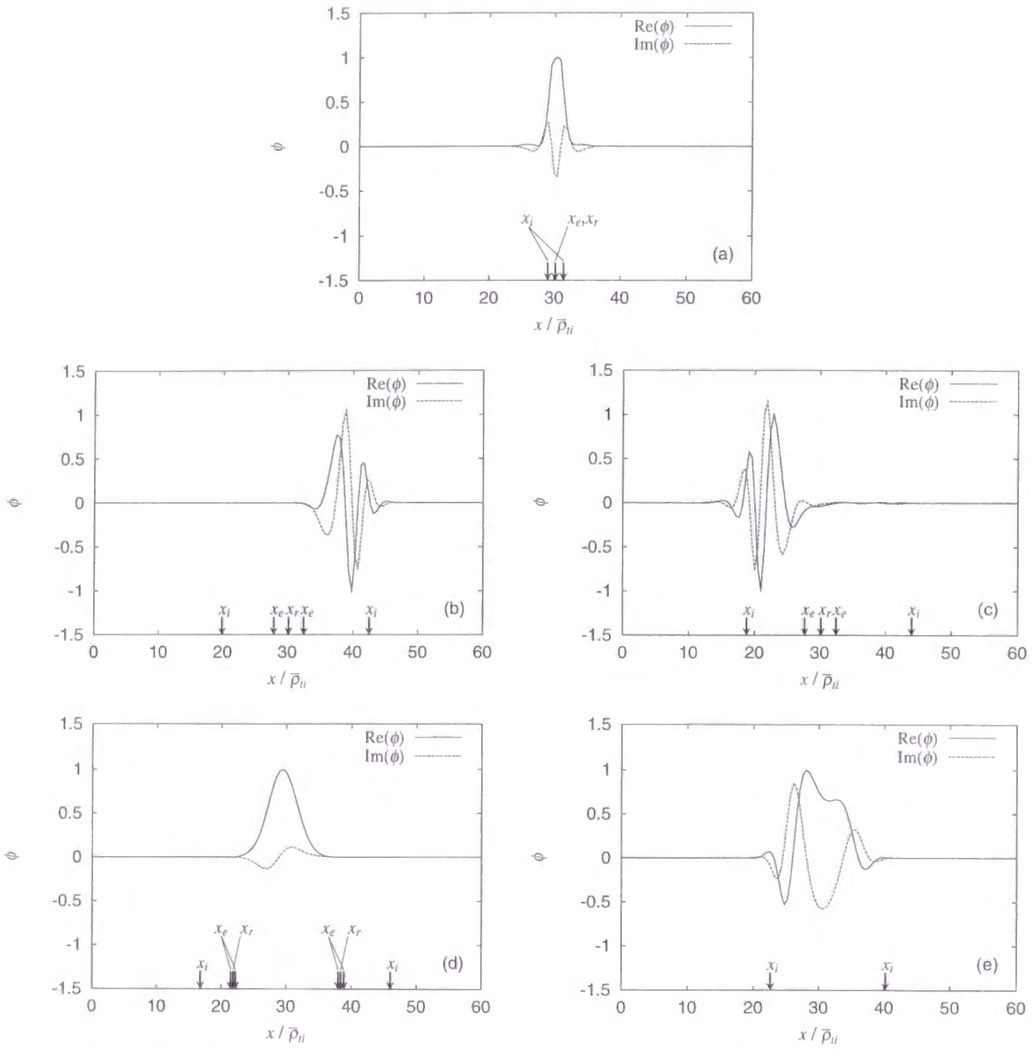

Figure 3.1: Typical eigenfunctions of the normal-sheared slab ITG modes are plotted for $\eta_i = \eta_e = 5$. (a) shows the $l = 0$ branch of the slab ITG mode for $k_y\bar{\rho}_{ti} \simeq 0.4$ and $L_n/L_s = 0.167$. (b) and (c) show the high-T_i and low-T_i branches of the single mode-rational surface NS-ITG mode for $k_y\bar{\rho}_{ti} \simeq 0.9$ and $k_y\bar{\rho}_{ti} \simeq 0.348$, respectively. (d) shows the $l = 0$ branch of the double mode-rational surface NS-ITG mode for $k_y\bar{\rho}_{ti} \simeq 1.5$ and $k_z\bar{\rho}_{ti} \simeq 0.00849$. (e) shows the $l = 0$ branch of the nonresonant NS-ITG mode for $k_y\bar{\rho}_{ti} \simeq 1.5$ and $k_z\bar{\rho}_{ti} \simeq -0.00849$. The nonresonant NS-ITG mode shows a oscillatory feature. For the negative shear case, a scale length of the magnetic shear has been chosen as $L_n/L_{ns} = 0.43$, and the $q_{\min}$-surface is at $x = 30.2\bar{\rho}_{ti}$. In all figures, positions of the mode-rational surface, x_r, the ion resonance point, x_i, and the electron resonance point, x_e are also indicated by arrows.

length is defined as

$$\Delta x \equiv \left(\bar{k}_x/2\pi\right)^{-1} = \left[\left(\sum_{k_x} k_x|\phi_{k_x}|\right) \Big/ \left(2\pi \sum_{k_x} |\phi_{k_x}|\right)\right]^{-1}. \tag{3.36}$$

Figure 3.1(b) and 3.1(c) show the eigenfunctions of the single mode-rational surface NS-ITG modes for $k_y\bar{\rho}_{ti} \simeq 0.9$ and $k_y\bar{\rho}_{ti} \simeq 0.348$, respectively. Since the linear stability of the slab ITG mode does not depend on the sign of the magnetic shear, this case corresponds to the weak shear limit of the normal shear case. In the weak magnetic shear region around the $q_{\min}$-surface, an unstable region of the single mode-rational surface NS-ITG mode satisfying $v_{ti} \le |\mathrm{Re}(\omega)/k_\parallel| \ll v_{te}$ is separated into two regions, which appear in both sides of the $q_{\min}$-surface, and two different types of asymmetric modes are destabilized in these regions. Since the ion Larmor radius and the corresponding FLR effect vary significantly in these regions under the steep ion temperature profile, the single mode-rational surface mode which is destabilized in the low-T_i (high-T_i) side of the $q_{\min}$-surface becomes unstable in the high-k_y (low-k_y) region. The eigenfunctions of both modes show an oscillatory feature, and give the almost equal radial correlation lengths, $\Delta x \sim 4.51\bar{\rho}_{ti}$ for the low-T_i mode and $\Delta x \sim 4.32\bar{\rho}_{ti}$ for the high-T_i mode. Figure 3.1(d) shows the eigenfunction of the double mode-rational surface NS-ITG mode for $k_y\bar{\rho}_{ti} \simeq 1.5$ and $k_z\bar{\rho}_{ti} \simeq 0.00849$ ($k_z \sim 3\times 2\pi/(q_0R)$). In this case, the ion resonance point does not appear in the $q_{\min}$ side of the two mode-rational surfaces, because of a weak magnetic shear around the $q_{\min}$-surface, and, hence, a broad unstable region satisfying $v_{ti} \le |\mathrm{Re}(\omega)/k_\parallel| \ll v_{te}$ appears in this region. Accordingly, the double mode-rational surface NS-ITG mode, which becomes a bounded solution, has an extremely broad eigenmode structure with $\Delta x \sim 15.0\bar{\rho}_{ti}$. Here, it is noted that for the NS-ITG modes which are analyzed in this section, the ratio of the radial correlation length Δx to the scale length of an ion temperature gradient L_{ti} reaches at $\Delta x/L_{ti} \sim 0.5$ and, therefore, the WKB procedure may not be appropriate for the analysis of this mode. Figure 3.1(e) shows the eigenfunction of the nonresonant NS-ITG mode for $k_y\bar{\rho}_{ti} \simeq 1.5$ and $k_z\bar{\rho}_{ti} \simeq -0.00849$. As is predicted by the analytical solution, we see that the eigenfunction, which is limited by two ion resonance points, shows an oscillatory behavior. Because of this oscillatory nature, the radial correlation length of the nonresonant NS-ITG mode, $\Delta x \sim 8.59\bar{\rho}_{ti}$, becomes much shorter than that of the double mode-rational surface NS-ITG mode.

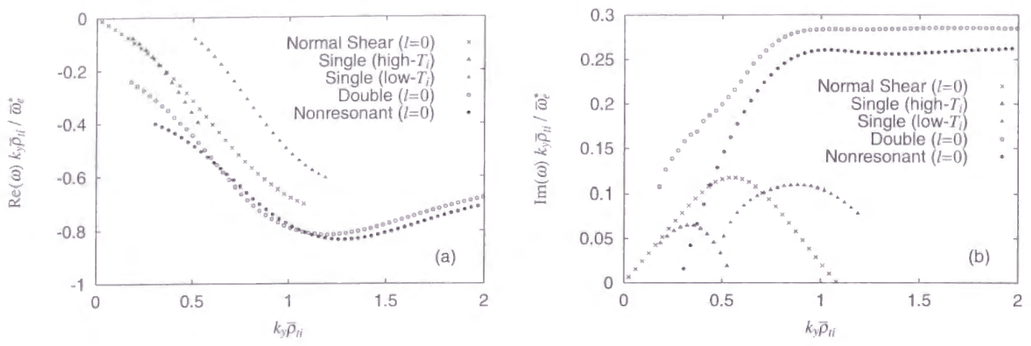

Figure 3.2: (a) Real frequency and (b) growth rate are plotted for the $l = 0$ branch of the normal-sheared slab ITG mode (crosses), the high-T_i (open triangles) and low-T_i (closed triangles) branches of the single mode-rational surface NS-ITG mode, the $l = 0$ branch of the double mode-rational surface NS-ITG mode (open circles), and the $l = 0$ branch of the nonresonant NS-ITG mode (closed circles). Equilibrium parameters are the same as in Fig. 3.1.

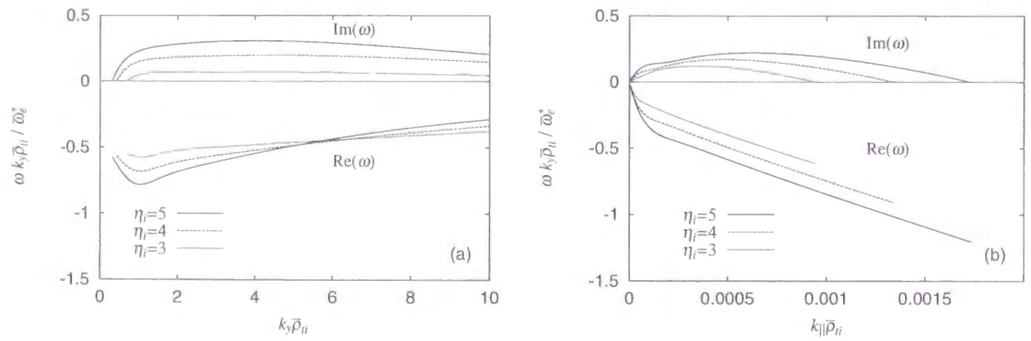

Figure 3.3: (a) k_y-dependence and (b) k_z-dependence of the local dispersion relation of the shearless slab ITG mode are plotted under conditions with (a) $k_x\bar{\rho}_{ti} \simeq 0.4$, $k_z\bar{\rho}_{ti} \simeq 0.00849$ and (b) $k_x\bar{\rho}_{ti} = k_y\bar{\rho}_{ti} \simeq 0.4$, and $\eta_i = \eta_e$.

Figure 3.2 shows the dispersion relation of the slab ITG modes corresponding to the modes shown in Fig. 3.1. It is seen that the unstable regions of the low-T_i (high-T_i) branch of the single mode-rational surface NS-ITG mode peaks in the high-k_y (low-k_y) region. The double mode rational-surface NS-ITG mode and the nonresonant NS-ITG mode show similar dispersive characteristics in both the real frequency and the growth rate. These two modes have relatively large growth rates compared with other three branches, and the unstable regions spread up to a significantly high-k_y region with $k_y\bar{\rho}_{ti} \sim 10$. In order to explain this unique feature of the NS-ITG modes, we have analyzed the k_y-dependence, Fig. 3.3(a), and the $k_\parallel$-dependence, Fig. 3.3(b), of the local dispersion relation for the shearless slab ITG mode at the $q_{\min}$-surface. As shown in Fig. 3.3(b), the ITG mode is basically the ion sound wave which is modified by the density and temperature gradients, and its stability is very sensitive to $k_\parallel$. Whereas, in Fig. 3.3(a), we see that with a constant $k_\parallel$, the k_y-dependence of the growth rate is weak for $k_y\bar{\rho}_{ti} > 1$. It is noted that the non-adiabatic ion response contributes to the stability of ITG mode in the high-k_y limit, while the contribution vanishes exponentially in the high-$k_\perp$ or k_x limit. This is because the non-adiabatic part of the ion response, Eq. (3.13), is proportional to $k_y\rho_{ti}\Gamma_0(b)$ or $k_y\rho_{ti}\Gamma_1(b)$, and in the high-k_y limit, these functions are approximated [79] as $\sqrt{b}\Gamma_0(b) \sim 0.399 + 0.0133b^{-1}$, and $\sqrt{b}\Gamma_1(b) \sim 0.399 - 0.0399b^{-1}$, respectively. Therefore, what is significant in stabilizing the ITG mode is not the variation of k_y but the variation of $k_\parallel$, which produces the ion Landau damping in a high-$k_\parallel$ region. In the sheared slab geometry, k_y and $k_\parallel$ are closely related by the magnetic shear. If the magnetic shear exist in an unstable region, $k_\parallel$ increases along with the increase of k_y, and the mode is then stabilized by the ion Landau damping for $k_y\bar{\rho}_{ti} > 1$. This is the kinetic stabilizing mechanism of the normal-sheared slab ITG mode and the single mode-rational surface NS-ITG mode. However, if the mode arises in a low magnetic shear region around the $q_{\min}$-surface, which corresponds to the double mode-rational surface and nonresonant NS-ITG modes, $k_\parallel$ is independent of k_y and the k_y-dependence of the stability is almost determined by the local stability of the slab ITG mode which is shown in Fig. 3.3(a). Thus, an unstable region with $k_y\bar{\rho}_{ti} > 1$ is allowed for the double mode-rational surface and nonresonant NS-ITG modes.

The destabilizing effect on the nonresonant mode is explained from a point of view

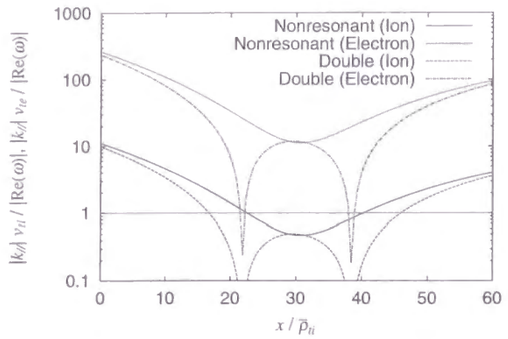

Figure 3.4: $|k_\parallel| v_{ti}/|\mathrm{Re}(\omega)|$ and $|k_\parallel| v_{te}/|\mathrm{Re}(\omega)|$ are plotted as a function of $x/\bar{\rho}_{ti}$ for the $l = 0$ branch of the double mode-rational surface NS-ITG mode (dashed curve and dash-dot curve) and the $l = 0$ branch of the nonresonant NS-ITG mode (solid curve and broken curve), which correspond to cases shown in Fig. 3.1(d) and Fig. 3.1(e). The behavior of resonance, which determines the local stability, is similar around the $q_{\min}$-surface at $x = 30.2\bar{\rho}_{ti}$ for both cases.

of the kinetic theory. In Fig. 3.4, we plot resonance conditions of these two modes, corresponding to Figs. 3.1(d) and 3.1(e). In the figure, it is considered that both modes are in a similar situation with respect to the local stability condition around the $q_{\min}$-surface, because almost the same resonance region with $v_{ti} \leq |\mathrm{Re}(\omega)/k_\parallel| \ll v_{te}$ is seen. Since the linear stability is essentially determined by the local resonance condition around the $q_{\min}$-surface, both the double mode-rational surface and nonresonant NS-ITG modes show similar behavior in the dispersion relation. However, the nonresonant NS-ITG mode gives a slightly lower growth rate than that of the double mode-rational surface NS-ITG mode, because of a stabilizing effect of the shear convective dumping.

In Fig. 3.3, the k_z-dependence of the growth rate spectrum is shown for the double mode-rational surface and nonresonant NS-ITG modes. Since the local stability does not depend on the sign of k_z, both spectrums, which follow the local dispersion shown in Fig. 3.4(b), are approximately symmetric about $k_z = 0$.

In Fig. 3.6, the q''-dependence of the growth rate is shown for the double mode-rational

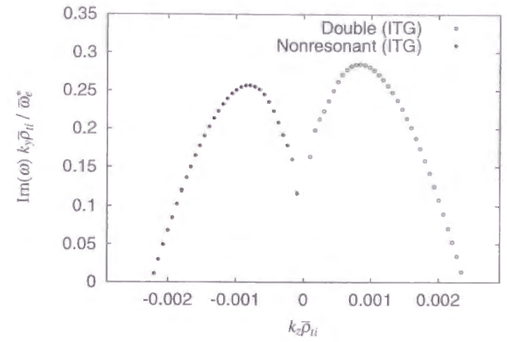

Figure 3.5: k_z-dependence of the growth rate is plotted for the $l = 0$ branch of the double mode-rational surface NS-ITG mode (open circles), and the $l = 0$ branch of the nonresonant NS-ITG mode (closed circles). Equilibrium parameters are the same as in Fig. 3.1 and $k_y\bar{\rho}_{ti} \simeq 1.5$.

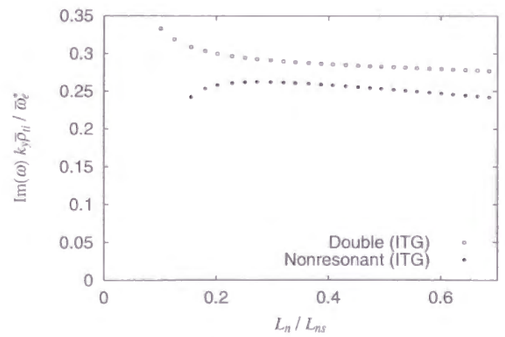

Figure 3.6: q''-dependence of the growth rate is plotted for the $l = 0$ branch of the double mode-rational surface NS-ITG mode with $k_y\bar{\rho}_{ti} \simeq 1.5$ and $k_z\bar{\rho}_{ti} \simeq 0.00849$ (open circle) and the $l = 0$ branch of the nonresonant NS-ITG mode $k_y\bar{\rho}_{ti} \simeq 1.5$ and $k_z\bar{\rho}_{ti} \simeq -0.00849$ (closed circle). Parameters used are the same as in Fig. 3.1. The magnetic configuration used in Fig. 3.1 corresponds to $L_n/L_{ns} = 0.43$.

surface and nonresonant NS-ITG modes. As the magnetic shear becomes weak, the growth rate slightly increases for both modes. However, in the weak magnetic shear limit, the behavior is different between the double mode-rational surface and nonresonant NS-ITG modes. In the weak magnetic shear configuration, the unstable region, where the fluid limit approximation is valid, becomes larger, and the stabilizing (and destabilizing) effect due to the oscillatory (bounded) solution and its asymptotic behavior strongly affects the growth rate.

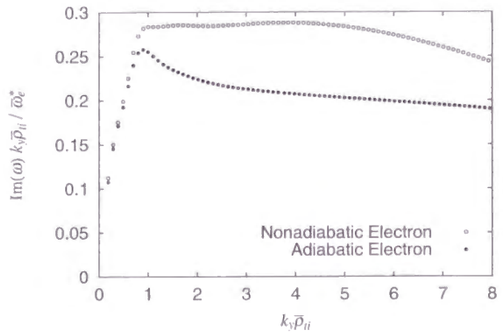

Figure 3.7: Growth rates of the $l = 0$ double mode-rational surface NS-ITG mode in the case with the non-adiabatic electron response (closed circles), and in the case with the adiabatic electron response (open circles).

Figure 3.7 shows the growth rates of the $l = 0$ double mode-rational surface NS-ITG mode which are calculated with the adiabatic electron response and the non-adiabatic electron response. Since the unstable region in the case with the adiabatic electron response also spreads over a high-k_y region, the mode has basically the feature of ion mode even in the high-k_y region. However, we see an increase of the growth rate due to the non-adiabatic electron response in the high-k_y region, where the electron FLR effect is also finite, $k_y \bar{\rho}_{te} < 0.1$. In the figure, we also see that an unstable region exists in the considerably high-k_y region with $k_y \bar{\rho}_{ti} \sim 10$. This is the unique feature of the NS-ITG mode. In the high-k_y region with $k_y \bar{\rho}_{ti} \sim 10$, the ETG mode also becomes important. A quantitative discussion on the growth rate or the unstable k_y region of the ETG mode will be given in

Chapter 4.

3.5 Discussion

In this chapter, we have analyzed the NS-ITG modes using the gyrokinetic integral eigenvalue code. In the negative shear configuration, several types of ITG modes exist due to the peculiar properties of the magnetic configuration: the magnetic shear is very weak around the $q_{\min}$-surface; and the configuration is determined by q_0'', which forms an effective potential well (hill) in the Weber type differential eigenmode equation. Depending on the number of the mode-rational surfaces, the NS-ITG mode is classified into three types: a single mode-rational surface mode, a double mode-rational surface mode, and a nonresonant mode.

In the single mode-rational surface case with $k_z = 0$, two separate unstable regions, which widely spread in both sides of the mode-rational surface, appear because of a very weak magnetic shear around the $q_{\min}$-surface. In both the high-T_i and low-T_i regions, independent asymmetric modes are excited. Since the ion temperature and the corresponding FLR effect vary considerably in these regions, the high-T_i (low-T_i) mode has an unstable region in the low-k_y (high-k_y) side.

We have shown both the analytic and numerical solutions for the double mode-rational surface and nonresonant NS-ITG modes. In an analytical treatment using the Weber type differential eigenmode equation, the double mode-rational surface (nonresonant) NS-ITG mode is characterized by an parabolic potential well (hill) perturbed by a fourth order potential hill, in which a bounded (oscillatory) solution is obtained around the $q_{\min}$-surface. Since the asymptotic behavior of the NS-ITG mode becomes the outgoing wave, a stabilizing effect of shear convective damping works for the nonresonant NS-ITG mode, and this mode gives a slightly lower growth rate than that of the double mode-rational surface NS-ITG mode. These solutions are also obtained from the gyrokinetic integral eigenvalue code. These analyses have shown an existence of a broad unstable region in the interior region between the two mode-rational surfaces or ion resonance points. Thus, the NS-ITG modes have an extremely broad radial eigenmode structure compared with that of

the normal-sheared slab ITG mode. Here, it should be noted that for the analysis of this kind of modes, which have a long radial correlation length, the WKB approximation or the ballooning representation seems inappropriate, because the scale length ordering, $\Delta x/L_n \sim \Delta x/L_t \sim \mathcal{O}(\epsilon)$, does not hold for the steep density and temperature profiles. Another particular feature of theses modes are that the unstable region spreads over the high-k_y region with $k_y\bar{\rho}_{ti} \sim 10$. Unlike the conventional slab ITG modes and the single mode-rational surface NS-ITG modes, these modes are excited in a weak magnetic shear region around the $q_{\min}$-surface, where $k_{||}$ becomes independent of k_y. Hence, the k_y-dependence of the growth rate is essentially determined locally at the $q_{\min}$-surface. Also, in the high-k_y region, the non-adiabatic electron response is important to sustain the instability. These numerical results may explain the short wavelength fluctuation with $k_\theta\rho_{ti} \sim 5$, based on the NS-ITG mode, which was observed in the TFTR enhanced reversed shear (ERS) experiment [80]. In order to identify this short wavelength fluctuation, a comparison with the ETG mode will be given in Chapter 4.

Chapter 4

Slab electron temperature gradient driven mode

4.1 Introduction

As is discussed in Chapter. 1, the ETG mode is considered as a candidate for the anomalous electron transport in the ITB of negative shear tokamaks. Although a correspondence between the observed temperature gradient parameter and its critical value for the ETG mode has been shown for the DIII-D negative shear experiment [30] using the kinetic ballooning code [17], the level of the electron anomalous transport induced by the ETG mode has not been estimated. For an estimation of a transport coefficient based on the mixing length theory, it is necessary to know a radial eigenmode structure or a radial correlation length, which is not given by kinetic ballooning calculations. Therefore, an integral eigenmode analysis is also required for the ETG mode. In Chapter 3, we have shown that the NS-ITG mode becomes strongly unstable in a region of the $q_{\min}$-surface, using a gyrokinetic integral eigenvalue code. This result imply an importance of the slab drift mode in the negative shear configuration. Since eigenmode equations have a similar form for both the ITG and ETG modes, the slab ETG mode is also supposed to become strongly unstable in the negative shear configuration.

In this chapter, we will discuss properties of the slab ETG modes in the negative shear

configuration. In the numerical results obtained from the gyrokinetic integral eigenvalue code, the negative-sheared slab ETG (NS-ETG) modes [61] are classified into three types as in the NS-ITG modes: a single mode-rational surface mode, a double mode-rational surface mode, and a nonresonant mode. In Section 3.3, we have already discussed the properties of the NS-ITG modes based on analytic solutions obtained from the Weber type differential eigenmode equation. The double mode-rational surface (nonresonant) NS-ITG mode has a bounded (oscillatory) solution. According to the conventional discussion for the ETG mode [10], the eigenmode equation of the slab ETG mode is equivalent to that of the slab ITG mode, if electron quantities are replaced with ion quantities, and similar analytic solutions are expected for both cases. However, the numerical results show that the ETG mode has a relatively long scale length compared with ρ_{te}, and its behavior is different from the corresponding solution of the slab ITG mode. An analytical estimation shows that this difference comes from a consistency condition. When $\lambda_{De}^2 \ll \rho_{te}^2$, the quasineutrality condition is imposed by the electron polarization effect, and the ETG mode is described by an almost identical eigenmode equation as that for the ITG mode, where λ_{De} is the electron Debye length. But, for typical fusion plasma parameters or the TFTR like parameters shown in Table 3.1, another limit, $\lambda_{De}^2 \gg \rho_{te}^2$, becomes valid, and a consistency condition is dominated by the Debye shielding effect. Under this condition, we have formulated a new eigenmode equation with retaining the Debye shielding effect. The analytic solutions obtained from this new eigenmode equation qualitatively show a good agreement with the numerical solutions, and their scale length is characterized by λ_{De}.

4.2 Analytic solutions

In Section 3.3, we have derived analytic solutions of the double mode-rational surface and nonresonant NS-ITG modes. The same solutions are also obtained for the slab ETG mode provided that the quasineutrality condition is imposed under $\lambda_{De}^2 \ll \rho_{te}^2$. However, when the Debye shielding is dominant or $\lambda_{De}^2 \gg \rho_{te}^2$, a new eigenmode equation, which is essentially different from the eigenmode equation for the slab ITG mode, is obtained with retaining the Debye shielding effect. Consequently, characteristics of solutions for the

slab ETG modes become different from the slab ITG modes. We will discuss qualitative features of these solutions particularly for the negative shear configuration.

The linear stability problem of the slab ETG mode has been discussed by several authors [10, 27], using a similar eigenmode equation to that of the slab ITG mode. For the short wavelength ETG modes, the kinetic ion response decreases exponentially because $k_\perp^2 \rho_{ti}^2 \gg 1$, and the adiabatic response can be assumed for the ion perturbed density. Again, if we assume the phase velocity and the perpendicular wavelength as $v_{te} < |\mathrm{Re}(\omega)/k_\parallel|$ and $k_\perp^2 \rho_{te}^2 \ll 1$, difference between the eigenmode equations for the slab ITG and ETG modes results in only modification for the particle species. However, it should be noted that a validity of the quasineutrality condition is not trivial for the short wavelength ETG mode, and that the above discussion is valid provided that the consistency condition is dominated by the electron polarization shielding effect rather than the Debye shielding effect, or for $\lambda_{De}^2 \ll \rho_{te}^2$. For the parameters used in the present analysis (see Table 3.1), this condition is violated, and it is necessary to consider the opposite limit, $\lambda_{De}^2 \gg \rho_{te}^2$. In order to analyze the slab ETG mode under this condition, we have derived a Weber type differential eigenmode equation with retaining the Debye shielding effect (without using the quasineutrality condition). Under the approximation of the long perpendicular wavelength, $b_e \ll 1$, we can reduce the integral eigenmode equation into the following second order ordinary differential equation,

$$\frac{d^2\tilde{\phi}}{d\tilde{x}^2} + Q(\tilde{x})\tilde{\phi} = 0, \tag{4.1}$$

$$Q(\tilde{x}) \equiv -\tilde{k}_y^2 + \frac{\tau + 1 + \{1 - 1/\tilde{\Omega} + \eta_e/(2\tilde{\Omega})\}\xi_e Z_e - (\eta_e/\tilde{\Omega})\xi_e^2(1 + \xi_e Z_e)}{-\tilde{\lambda}^2 + \{1 - 1/\tilde{\Omega} - \eta_e/(2\tilde{\Omega})\}\xi_e Z_e - (\eta_e/\tilde{\Omega})\xi_e^2(1 + \xi_e Z_e)}, \tag{4.2}$$

where $\tilde{\lambda} = \lambda_{D_e}/\rho_{te}$ and the normalizations are taken to be the same as for Eq. (3.20), except for the unit length, $\tilde{x} \equiv x/\rho_{te}$ and $\tilde{k}_y \equiv k_y \rho_{te}$. By applying the fluid limit approximation, $\xi_e \gg 1$, the plasma dispersion function is written in a form of the asymptotic expansion, $Z_e \sim -\xi_e^{-1} - \frac{1}{2}\xi_e^{-3} - \frac{1}{4}\xi_e^{-5} - \cdots$. We then have a reduced form of the eigenmode equation as

$$\frac{d^2\tilde{\phi}}{d\tilde{x}^2} + \left[-\tilde{k}_y^2 + \frac{1 + \tau\tilde{\Omega}}{-\tilde{\lambda}^2\tilde{\Omega} + (1 + \eta_e)} - \left(\frac{1}{\tilde{\Omega}} - 1\right)\frac{\tilde{L}_n^2 \tilde{k}_\parallel^2}{\tilde{k}_y^2 \tilde{\Omega}^2}\right]\tilde{\phi} = 0, \tag{4.3}$$

where the lowest order terms are retained by assuming $\tilde{\lambda}^2 = \lambda_{De}^2/\rho_{te}^2 \gg 1$. In Eq. (4.3), we see one salient feature in the potential term, which comes from the third term in square parenthesis. Since the sign of this potential term, which characterizes the potential hill (or well) structure, becomes negative for a typical case with $\tilde{\Omega} < 1$ (and $\tilde{\Omega} > 0$ for an electron mode), we expect that solutions of the slab ETG mode show a different feature from the slab ITG modes.

For the normal shear case, Eq. (4.3) is again written in a standard form of the Weber equation, and the eigenfunction and the dispersion relation are respectively given by Eqs. (3.23) and (3.24), except for the definitions of variables:

$$\zeta = a\tilde{x}, \quad a = \left[\left(\frac{1}{\tilde{\Omega}} - 1\right)\frac{\tilde{L}_n^2}{\tilde{L}_s^2\tilde{\Omega}^2}\right]^{1/4}, \quad \epsilon = a^{-2}\left[-\tilde{k}_y^2 + \frac{1+\tau\tilde{\Omega}}{-\tilde{\lambda}^2\tilde{\Omega} + (1+\eta_e)}\right].$$

Unlike the slab ITG mode, the normal-sheared slab ETG mode becomes a bounded solution, and a stabilizing effect of shear convective damping is not expected.

For the negative shear configuration, the eigenfunction and the dispersion relation, which are again described by Eqs. (3.28)-(3.33), respectively, are obtained with the following definitions:

$$\zeta = a\tilde{x}, \quad a = \left[-\frac{2\tilde{k}_z}{\tilde{k}_y}\left(\frac{1}{\tilde{\Omega}} - 1\right)\frac{\tilde{L}_n^2}{\tilde{L}_{ns}^2\tilde{\Omega}^2}\right]^{1/4},$$

$$\alpha \equiv \left(-\frac{\tilde{k}_y}{2\tilde{k}_z}\right)^{3/2}\left[\frac{1}{1/\tilde{\Omega} - 1}\frac{\tilde{\Omega}^2}{\tilde{L}_n^2\tilde{L}_{ns}^2}\right]^{1/2},$$

$$\epsilon = a^{-2}\left[-\tilde{k}_y^2 + \frac{1+\tau\tilde{\Omega}}{-\tilde{\lambda}^2\tilde{\Omega} + (1+\eta_i)} - \left(\frac{1}{\tilde{\Omega}} - 1\right)\frac{\tilde{L}_n^2\tilde{k}_z^2}{\tilde{\Omega}^2\tilde{k}_y^2}\right].$$

For the eigenfrequency with $|\mathrm{Re}(\tilde{\Omega})| \gg |\mathrm{Im}(\tilde{\Omega})|$, Eq. (3.28) gives an oscillatory solution in the double mode-rational surface case with $k_z > 0$. For ETG modes with $\mathrm{Re}(\tilde{\Omega}) > 0$, the asymptotic solution is obtained as

$$\lim_{|x|\to\infty}\tilde{\phi} = C\exp\left[-\left(\frac{1}{\tilde{\Omega}} - 1\right)^{1/2}\frac{|\tilde{L}_n|}{3\tilde{L}_{ns}^2\tilde{\Omega}}|\tilde{x}|^3\right]. \tag{4.4}$$

For the eigenfrequency with $|\mathrm{Re}(\tilde{\Omega})| \gg |\mathrm{Im}(\tilde{\Omega})|$, Eq. (4.4) gives a damped solution. Thus, although the eigenfunction, Eq. (3.28), shows an oscillatory feature, a stabilizing effect of shear convective damping is expected to be weak. For the nonresonant case with $k_z < 0$, Eq.

(3.28) becomes basically a bounded solution. Since the bounded solution gives a relatively longer radial correlation length compared with the oscillatory solution, the nonresonant NS-ETG mode is likely to give a significant contribution to the electron anomalous transport.

4.3 Numerical solutions

With the gyrokinetic integral eigenvalue code, we analyze the slab ETG mode in the negative shear model configuration. As in the NS-ITG modes shown in Section 3.4, the NS-ETG modes are also classified into three types: a single mode-rational surface mode, a double mode-rational surface mode, and a nonresonant mode. However, as shown in Section 4.2, the properties of these modes are different from the corresponding ITG modes, because of the Debye shielding effect. Also, from a quantitative comparison between calculations with and without the Debye shielding term, we will discuss effects of the Debye shielding term on the scale length and eigenfrequency of the ETG mode.

The TFTR like parameters shown in Table 3.1 are used also in the study of the ETG mode. It is noted that these parameters correspond to the case where the quasineutrality condition is violated for the short wavelength ETG mode, since $\bar{\lambda}_{De}^2/\bar{\rho}_{te}^2 \sim 10$. The model magnetic configuration is also the same as in Section 3.4: $L_s = 2.78$m for the normal shear case and $L_{ns} = 0.883$m for the negative shear case. As is mentioned in the previous section, the adiabatic electron response is often used for analyses of the ITG mode and, on the contrary, the adiabatic ion response is used for the ETG mode. Instead of these assumptions, in the present analysis, we have retained the full kinetic responses both for ions and for electrons, in order to make a rigorous comparison between the ITG and ETG modes under the same conditions. In the code, $128 \sim 256$ modes are used for the k_x spectrum in order to obtain a good convergence for the short wavelength ETG mode.

Figure 4.1 shows the eigenfunctions of the slab ETG modes, where the same temperature gradient parameter, $L_{ti} = L_{te} = 0.076$m ($\eta_i = \eta_e = 5$), as in Fig. 3.1 is adopted. In Fig. 4.1(a1), the eigenfunction of the $l = 0$ branch of the normal-sheared slab ETG mode for $k_y\bar{\rho}_{te} \simeq 0.235$ is plotted. For this eigenfunction, the radial correlation length is evaluated as $\Delta x \sim 0.213\bar{\rho}_{ti}(\sim 16.5\bar{\rho}_{te} \sim 5.16\bar{\lambda}_{De})$, where Δx is given by Eq. (3.36). It seems that

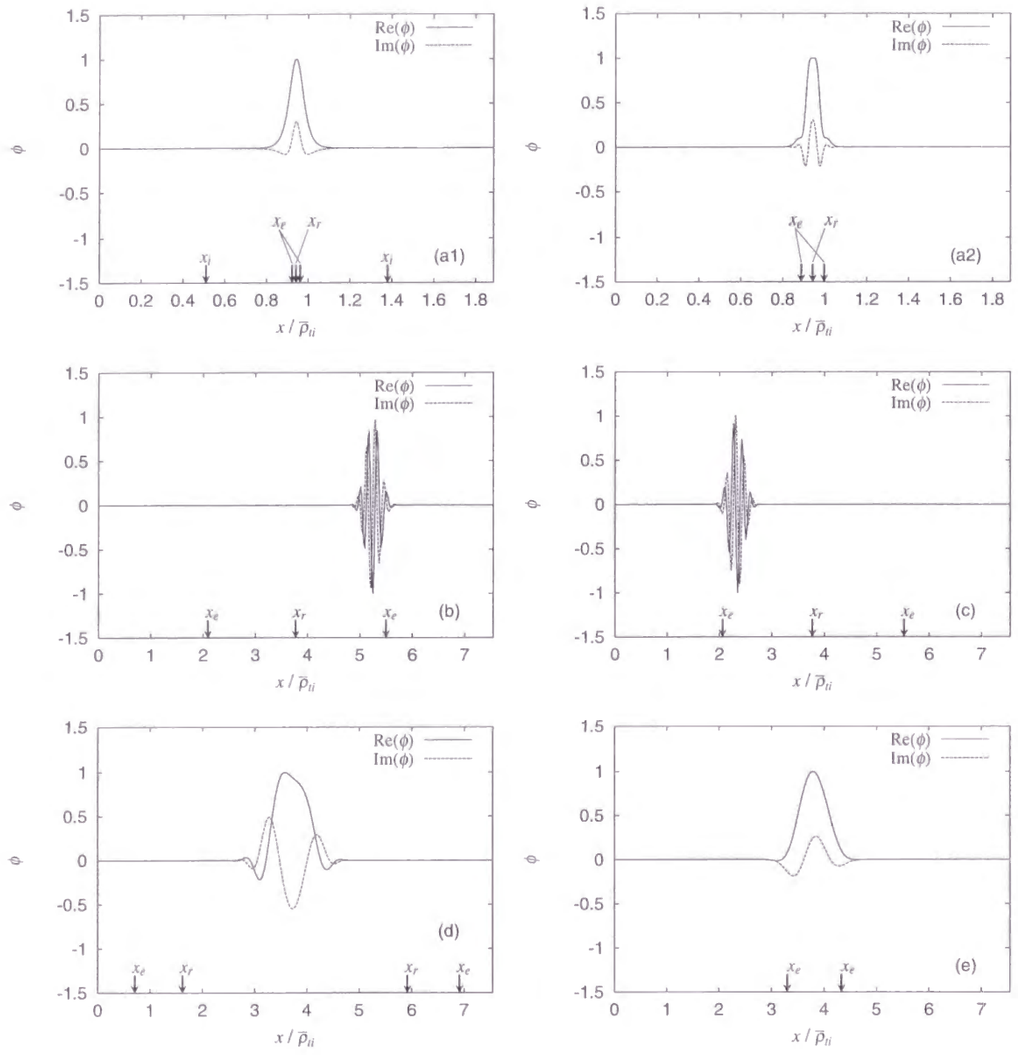

Figure 4.1: Typical eigenfunctions of the slab ETG modes are plotted for $\eta_i = \eta_e = 5$. (a1) shows the $l = 0$ branch of the normal-sheared slab ETG mode for $k_y\bar{\rho}_{te} \simeq 0.235$. (a2) shows the same branch, which is obtained with the quasineutrality condition, for $k_y\bar{\rho}_{te} \simeq 0.476$. (b) and (c) show the high-T_e and low-T_e branches of the single mode-rational surface NS-ETG modes for $k_y\bar{\rho}_{te} \simeq 0.347$. (d) shows the $l = 0$ branch of the double mode-rational surface NS-ETG mode for $k_y\bar{\rho}_{te} \simeq 0.284$ and $k_z\bar{\rho}_{ti} \simeq 0.00849$. (e) shows the $l = 0$ branch of the nonresonant NS-ETG mode for $k_y\bar{\rho}_{te} \simeq 0.284$ and $k_z\bar{\rho}_{ti} \simeq -0.00849$. In all cases, the equilibrium configuration is the same as is used in Fig. 3.1.

the characteristic scale length of the mode structure is determined basically by the Debye shielding effect, since $\bar{k}_x\bar{\lambda}_{De} \sim 2\pi\bar{\lambda}_{De}/\Delta x \sim 1.2$. In order to confirm characteristics which are predicted in the analytical solution, the eigenfunction of the same branch which is calculated by imposing the quasineutrality condition is also shown for $k_y\bar{\rho}_{te} \simeq 0.476$ in Fig. 4.1(a2). In this case, the radial correlation length, $\Delta x \sim 0.135\bar{\rho}_{ti}$, is much smaller than that in Fig. 4.1(a1). Since the eigenmode equation becomes similar to that of the slab ITG mode, an oscillatory solution is expected for this case. However, such an oscillatory feature of the eigenfunction is not so clear in Figs. 3.1(a) and 4.1(a2), because both eigenfunctions are limited in a narrow region between the two kinetic resonance points, where the fluid limit approximation is violated. Figures 4.1(b) and 4.1(c) show the eigenfunctions of the single mode-rational surface NS-ETG mode for $k_y\bar{\rho}_{te} \simeq 0.347$. In this case, two unstable regions with $v_{te} \leq |\mathrm{Re}(\omega)/k_\parallel|$ exist in both sides of the $q_{\min}$-surface, and the similar eigenfunctions as seen for the single mode-rational surface NS-ITG mode in Figs. 3.1(c) and 3.1(d) are obtained. For both branches of the single mode-rational surface NS-ETG mode in Figs. 4.1(b) and 4.1(c), the radial correlation lengths are estimated as $\Delta x \sim 0.167\bar{\rho}_{ti}$. Figure 4.1(d) shows the eigenfunction of the $l = 0$ branch of the double mode-rational surface NS-ETG mode for $k_y\bar{\rho}_{te} \simeq 0.284$ (and $k_z\bar{\rho}_{ti} \simeq 0.00849$). The radial correlation length becomes larger than above two cases [see Figs. 4.1(a)-4.1(c)], $\Delta x \sim 1.20\bar{\rho}_{ti}$, and the eigenfunction shows an oscillatory feature as is predicted by the analytical solution. Figure 4.1(e) shows the eigenfunction of the $l = 0$ branch of the nonresonant NS-ETG mode for $k_y\bar{\rho}_{te} \simeq 0.284$ (and $k_z\bar{\rho}_{ti} \simeq -0.00849$). Since the nonresonant NS-ETG mode has a bounded solution, its radial correlation length, $\Delta x \sim 1.64\bar{\rho}_{ti}$, is larger than that of the double mode-rational surface NS-ETG mode.

In order to see a difference which comes from the Debye shielding effect, we plot the dispersion relations of the normal-sheared slab ETG mode obtained with the Poisson equation [see Fig. 4.1(a1)] and with the quasineutrality condition [see Fig. 4.1(a2)] in Fig. 4.2. Because of a difference in the consistency condition, an unstable k_y region becomes different between these two cases, and the case with the quasineutrality condition becomes unstable for $k_y\lambda_{De} > 1$, while the case with the Poisson equation has an unstable region for $k_y\lambda_{De} < 1$. Also, the real frequency and the growth rate of the case with the quasineu-

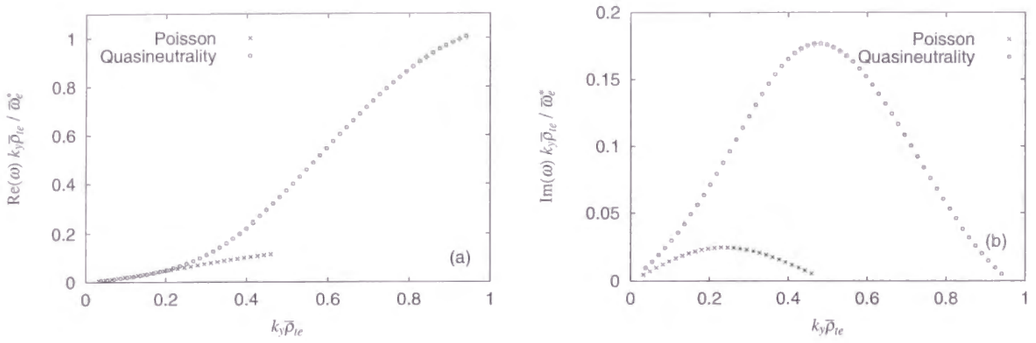

Figure 4.2: (a) Real frequency and (b) growth rate are plotted for the $l = 0$ branch of the normal-sheared slab ETG mode, which are calculated by imposing the Poisson equation (crosses) and the quasineutrality condition(open circles). The eigenfunctions of these branches are shown in Fig. 4.1(a1) and 4.1(a2), respectively.

trality condition are very large compared with the case with the Poisson equation, because in a high k_y region, a corresponding ω_e^* also becomes large. Hence, it is considered that analyses with the quasineutrality condition overestimate a real frequency and a growth rate of short wavelength micro-instabilities. It is noted that Lee *et al.* analyzed the slab ETG mode using a Vlasov integral eigenvalue code with retaining the Debye shielding effect [27]. However, since they adopted parameters with $\Omega_e^2/\omega_{pe}^2 = 1$, i.e, $\lambda_{De}^2/\rho_{te}^2 = 1$, their numerical results showed the unstable k_y region of the slab ETG mode for $k_y\rho_{te} < 1$, and the characteristic scale length of $\sim \rho_{te}$, where ω_{pe} is the electron plasma frequency.

Figure 4.3 shows the dispersion relation of the slab ETG modes corresponding to the five branches shown in Fig. 4.1. Compared with the dispersion relation of the slab ITG mode, several qualitative differences are seen in this dispersion relation. Firstly, for the high-T_e and low-T_e branches of the single mode-rational surface NS-ETG modes, a separation of unstable regions in the k_y space is not seen. It is considered that for a mode whose scale length is determined mainly by the Debye shielding effect, the electron FLR effect is weak, $k_\perp^2\rho_{te}^2 \sim \rho_{te}^2/\lambda_{De}^2 \ll 1$. Secondly, the double mode-rational surface NS-ETG mode and the nonresonant NS-ETG mode give the almost equal real frequency and growth rate. This is

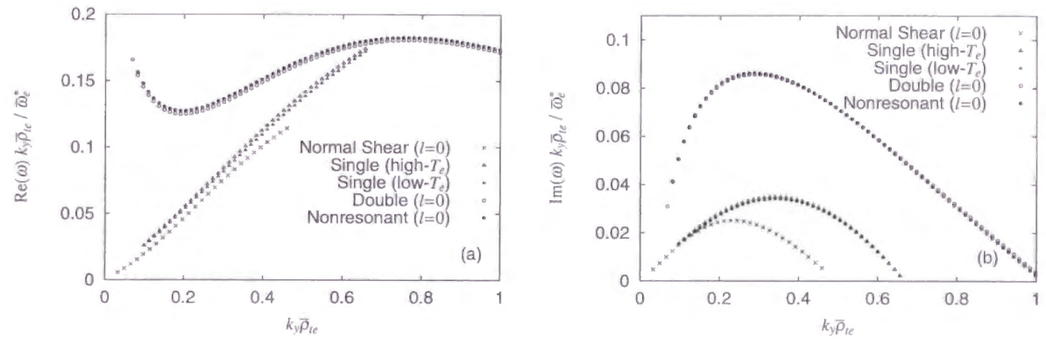

Figure 4.3: (a) Real frequency and (b) growth rate are plotted for the $l = 0$ branch of the normal-sheared slab ETG mode (crosses), the high-T_e (open triangles) and low-T_e (closed triangles) branches of the single mode-rational surface NS-ETG mode, the $l = 0$ branch of the double mode-rational surface NS-ETG mode with $k_z\bar{\rho}_{ti} \simeq 0.00849$ (open circles), and the $l = 0$ branch of the nonresonant NS-ETG mode with $k_z\bar{\rho}_{ti} \simeq -0.00849$(closed circles). Unlike the dispersion of the single mode-rational surface NS-ITG mode, the unstable k_y-regions of the two single mode-rational surface NS-ITG modes is not separated. Here, the double mode-rational surface NS-ITG mode and the nonresonant NS-ITG mode give almost the same frequency and growth rate. Equilibrium parameters are the same as in Fig. 4.1.

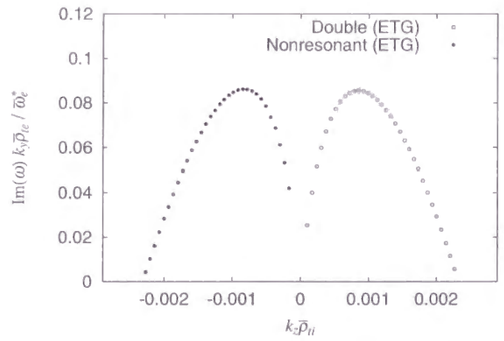

Figure 4.4: k_z-dependence of the growth rate is plotted for the $l = 0$ branch of the double mode-rational surface NS-ETG mode (open circles), and the $l = 0$ branch of the nonresonant NS-ETG mode (closed circles). Equilibrium parameters are the same as in Fig. 4.1. and $k_y\bar{\rho}_{te} \simeq 0.283$

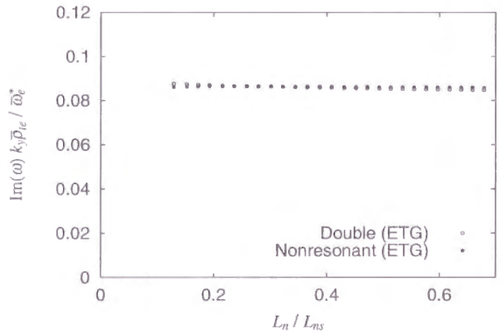

Figure 4.5: q''-dependence of the growth rate is plotted for the $l = 0$ branch of the double mode-rational surface NS-ETG mode with $k_y\bar{\rho}_{te} \simeq 0.284$ and $k_z\bar{\rho}_{ti} \simeq 0.00849$ (open circle) and the $l = 0$ branch of the nonresonant NS-ETG mode with $k_y\bar{\rho}_{ti} \simeq 0.284$ and $k_z\bar{\rho}_{ti} \simeq -0.00849$ (closed circle). Parameters used are the same as in Fig. 4.1.

understood from that the stabilizing effect due to shear convective damping does not work for the double mode-rational surface NS-ETG mode. Also, the unstable regions of these two types of ETG modes are limited for $k_y\bar{\rho}_{te} < 1$, while the double mode-rational surface NS-ITG mode and the nonresonant NS-ITG mode are unstable for $k_y\bar{\rho}_{ti} \gg 1$. Since the unstable k_y regions are characterized by the Debye shielding effect, peaks of the growth rates of these modes are at $k_y \sim 0.3\bar{\rho}_{te}^{-1} \sim \bar{\lambda}_{De}^{-1}$, where the electron FLR effect is not significant.

Figures 4.4 and 4.5 show the k_z-dependence and q''-dependence of the growth rate for the double mode-rational surface and nonresonant NS-ETG modes. As is discussed above, both modes show a similar behavior because of an absence of a stabilizing effect due to the shear convective damping.

4.4 Comparison between ETG mode and ITG mode

In Fig. 4.6, the k_y-dependences of the growth rate for both the slab ITG and ETG modes, which are taken from Figs. 3.2(b) and 4.2(b), are compared. Here, the conventional normal shear case is plotted as a reference. For the negative shear case, the double mode-rational surface mode and the nonresonant mode, which seem to give a significant contribution to the anomalous thermal transport, are plotted. In Fig. 4.6, it is seen that relevant regimes of k_y and $\mathrm{Im}(\omega)$ for each branch of the slab ETG modes are larger than those of the corresponding slab ITG modes by the ratio of $\bar{\rho}_{ti}/\bar{\lambda}_{De} \sim 24$. While the double mode-rational surface NS-ITG mode and the nonresonant NS-ITG mode are unstable up to $k_y\bar{\rho}_{ti} \sim 10$, the corresponding NS-ETG modes become marginally stable at $k_y\bar{\lambda}_{De} \sim 3$ (or $k_y\bar{\rho}_{te} \sim 1$). This difference comes from a treatment of a consistency condition. For the ITG mode with $k_\perp^2\lambda_{De}^2 \ll 1$, the quasineutrality condition is imposed due to the ion polarization effect, which appears as the ion polarization density in the integral eigenmode equation, Eq. (3.14). In the description including the full FLR effect, this term approaches to a constant, $-en_0\phi/T_i$, as k_y increases. On the other hand, the Debye shielding effect, which appears in the L.H.S. of the Poisson equation, Eq. (3.8), continues to increase monotonically as k_y increases, and, therefore, the slab ETG mode with $k_\perp\bar{\lambda}_{De} \gg 1$ becomes forbidden by the

strong Debye shielding effect.

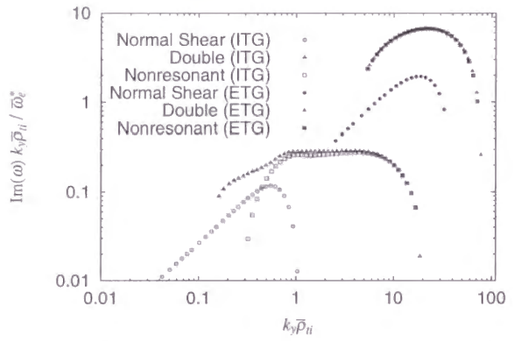

Figure 4.6: The growth rates are plotted as a function of k_y for both the slab ITG and ETG modes. For both modes, the growth rates of the double mode-rational surface negative-sheared slab mode, the nonresonant negative-sheared slab mode, and the conventional slab mode are plotted. All results are taken from Figs. 3.2(b) and 4.2(b).

Figure 4.7 shows the $\eta_i(=\eta_e)$-dependence of the growth rates of the slab ITG mode and the slab ETG mode. For each mode, k_y and k_z are chosen so that a critical temperature gradient parameter, $\eta_{ic}(=\eta_{ec})$, becomes the approximately minimum value. In the normal shear case with $L_n/L_s = 0.167$, almost the same critical value around $\eta_{ic}(=\eta_{ec}) \sim 1.8$ is given for both the slab ITG and ETG modes. On the other hand, in the negative shear case, the NS-ITG modes give a lower critical value $\eta_{ic} \sim 1.5$ than that in the normal shear case, while the NS-ETG modes give an almost the same critical value $\eta_{ec} \sim 1.8$.

Figure 4.8 shows the η_i-dependence of the transport coefficient, $\mathrm{Im}(\omega)\Delta x^2$, based on the conventional mixing length theory. Parameters used in the calculations in Fig. 4.8 are the same as those in Fig. 4.7. Hence, the transport coefficients are estimated for the modes close to the marginal values of η_{ic}. Since the radial correlation length occupies a significant contribution to $\mathrm{Im}(\omega)\Delta x^2$, the slab ITG modes give higher transport coefficients than the corresponding slab ETG modes in both the normal and negative shear cases. Also, for both the slab ITG and ETG modes, order of magnitude higher transport coefficients are obtained in the negative shear case compared with the normal shear case. As is predicted by

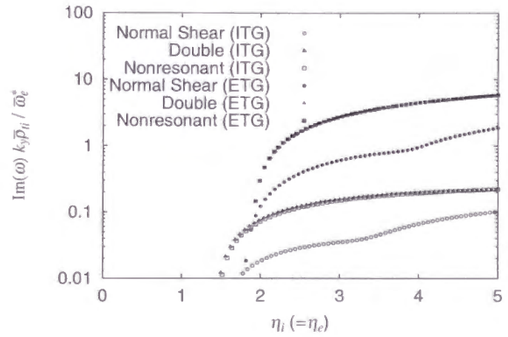

Figure 4.7: The growth rates as a function of $\eta_i(=\eta_e)$ for the $l = 0$ branch of the normal-sheared slab ITG mode for $k_y\bar{\rho}_{ti} \simeq 0.4$ (open circle), the $l = 0$ branch of the double mode-rational surface NS-ITG mode for $k_y\bar{\rho}_{ti} \simeq 1.06$ and $k_z\bar{\rho}_{ti} \simeq 4.24 \times 10^{-4}$ (open triangle), the $l = 0$ branch of the nonresonant NS-ITG mode for $k_y\bar{\rho}_{ti} \simeq 1.06$ and $k_z\bar{\rho}_{ti} \simeq 4.24 \times 10^{-4}$ (open square), the $l = 0$ branch of the slab ETG mode for $k_y\bar{\rho}_{te} \simeq 0.246$ (closed circle), the $l = 0$ branch of the double mode-rational surface NS-ETG mode for $k_y\bar{\rho}_{te} \simeq 0.41$ and $k_z\bar{\rho}_{ti} \simeq 4.24 \times 10^{-4}$ (closed triangle), and the $l = 0$ branch of the nonresonant NS-ITG mode for $k_y\bar{\rho}_{te} \simeq 0.41$ and $k_z\bar{\rho}_{ti} \simeq 4.24 \times 10^{-4}$ (closed square). The same equilibrium configuration as in Fig. 3.1 and 4.1 are used. Wavenumbers are chosen so that η_{ic} $(=\eta_{ec})$ becomes the approximately minimum value in the k_y and k_z space.

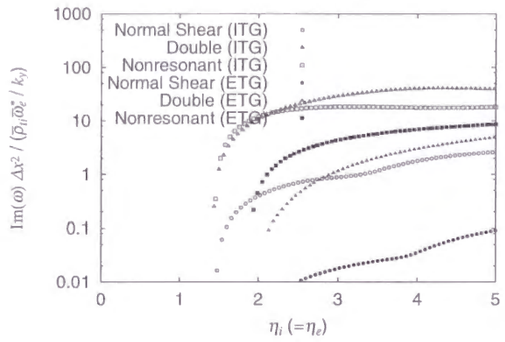

Figure 4.8: $\eta_i(=\eta_e)$-dependence of the transport coefficient estimated with the mixing length theory, $\mathrm{Im}(\omega)\Delta x^2$, is plotted for both the ITG and ETG modes which are shown in Fig. 4.7. For the ITG modes, the double mode-rational surface NS-ITG mode has a dominant contribution, while for the ETG modes, the nonresonant mode gives the largest contribution to the anomalous transport.

the analytic solution, the double mode-rational surface NS-ITG mode and the nonresonant NS-ETG mode, which have a bounded solution, give the largest transport coefficient in the negative shear case, respectively. It should be noted that the transport coefficient of the nonresonant NS-ETG mode exceeds that of the normal-sheared slab ITG mode. This remarkable feature implies that the electron anomalous transport arising from the slab ETG mode may become large enough to suppress the electron temperature gradient, especially in the negative shear configuration.

4.5 Discussion

In this chapter, we have analyzed the slab ETG modes in the negative shear configuration. In the numerical results obtained from the gyrokinetic integral eigenvalue code, the NS-ETG mode also has three types of branches: the single mode-rational surface mode, the double mode-rational surface mode, and the nonresonant mode. For the single mode-rational surface mode, several independent branches are destabilized in two unstable region-

s, which appear in both sides of the $q_{\min}$-surface. However, their unstable regions are not separated in the k_y space unlike the single mode-rational surface NS-ETG modes, because the FLR effect is not significant in their unstable regions with $k_y\bar{\lambda}_{De} \sim 1$ ($k_y\bar{\rho}_{te} \sim 0.3$). The double mode-rational surface mode with a broad eigenfunction becomes unstable in an interior region between the two mode-rational surfaces. Also, the nonresonant NS-ETG mode with a broad eigenfunction appears in an unstable region between the two electron resonance points. Since both the double mode-rational surface and nonresonant modes are destabilized in a weak magnetic shear region around the $q_{\min}$-surface, their stability is basically determined by the local stability at the $q_{\min}$-surface, as in the NS-ITG modes. While the NS-ITG modes have a high-k_y unstable region for $k_y\bar{\rho}_{ti} \leq 10$, their unstable regions are limited for $k_y\bar{\rho}_{te} < 1$. All these difference between the ITG and ETG modes can be explained by the Debye shielding effect. From the mixing length estimate of the transport coefficient, the double mode-rational surface and nonresonant NS-ETG modes seem to play an important role in the electron anomalous transport in the negative shear configuration.

We have also shown analytic solutions of the slab ETG mode with the eigenmode equation formulated for $\lambda_{De}^2/\rho_{te}^2 \gg 1$, or with retaining the Debye shielding effect. Compared to the conventional eigenmode equation, which is obtained by changing the particle species from ions to electrons, the new eigenmode equation for the slab ETG modes has qualitatively different properties: the potential term has the opposite sign, and the scale length is characterized by the Debye length. Because of these characteristics, the solutions are classified differently. The normal-sheared slab ETG mode has a bounded solution, and, therefore, the stabilizing effect of shear convective damping is not expected. In the negative shear case, the double mode-rational surface NS-ETG mode has an oscillatory solution, and the nonresonant NS-ETG mode has a bounded solution. However, unlike the ITG modes, the stabilizing effect does not appear in the oscillatory solution of the double mode-rational surface NS-ETG mode, since the asymptotic behavior is determined by a damped solution. All these properties predicted in the analytical calculations have been proved in the numerical results.

In the TFTR enhanced reversed shear experiment, Wong *et al.* observed short wave-

length ion mode fluctuations with a typical wavenumber of $k_y\bar{\rho}_{ti} \sim 5$ and a frequency of $\omega \sim 0.08\omega_i^*$ [80]. From a comparison of the dispersion relation with these results, we see that at $k_y\bar{\rho}_{ti} \sim 5$, the unstable regions of the NS-ITG mode and the NS-ETG mode overlap each other. However, their frequency regimes are separated by the ratio of ρ_{ti}/λ_{De}. At $k_y\bar{\rho}_{ti} \sim 5$, their frequencies are estimated as $\omega \sim 0.03\bar{\omega}_i^*$ for the NS-ITG mode and $\omega \sim -0.74\bar{\omega}_i^*$ for the NS-ETG mode. Therefore, the observed short wavelength fluctuation may be explained by the NS-ITG mode.

As for the transport coefficient based on the mixing length theory, a significant enhancement of the coefficient is observed in the negative shear configuration, because of a large radial correlation length which is produced by a weak magnetic shear around the $q_{\min}$-surface. Also, since the scale lengths of the slab ITG and ETG modes disparate by the ratio of ρ_{ti}/λ_{De}, the slab ITG modes give much larger transport coefficients compared with the corresponding ETG modes. However, it is remarkable that the transport coefficients of the NS-ETG modes exceed that of the normal-sheared slab ITG mode. This large transport coefficient indicates the electron anomalous transport due to the ETG mode, which is enough for explaining the experimental data.

In the present analysis, we have considered a plasma with $\lambda_{De}^2/\rho_{te}^2 \gg 1$. For the toroidal magnetic field of $B_0 \sim 4.6$T in TFTR, this condition does not breaks down until the electron density increases up to $n_0 \sim 2 \times 10^{20}\mathrm{m}^{-3}$, where $\lambda_{De}^2/\rho_{te}^2 \sim 1$. Therefore, this condition seems to be valid for usual experimental parameters.

Chapter 5

Nonlinear simulation of ETG turbulence

5.1 Introduction

In Chapter 4, we have shown that the mixing length estimate for the slab ETG mode in the negative shear configuration give an order of magnitude larger transport coefficient than that for the conventional normal-sheared slab ETG mode. Also, in recent Vlasov simulation of the ETG turbulence [62], it has been reported that the electron thermal transport is greatly enhanced by radially elongated vortices (or streamers). These results may support the transport data analysis for the DIII-D negative shear discharges [30], in which it has been reported that the electron temperature gradient is limited by the stability of the ETG mode. Therefore, the ETG turbulence is a recent topic, and its nonlinear properties are of interest for understanding the electron anomalous transport in tokamaks.

In this chapter, the ETG turbulence in a sheared slab configuration modeling the negative shear tokamak is studied using a gyrokinetic PIC simulation. Our previous gyrokinetic PIC code [59] is modified into a finite element PIC method [33], which is stable for the numerical instability reported in Ref. [81]. Numerical simulations with a two-and-a-half dimensional slab model are performed for the nonresonant NS-ETG mode, because this mode gives a significant contribution to the electron thermal transport with the mixing

length estimate shown in Section 4.4. In a linear growth phase of the simulation, the eigenmode structure is characterized by radially elongated vortices, which is consistent with the linear eigenmode structure in Section 4.2. However, a quasi-steady phase after a nonlinear saturation of the unstable ETG mode is characterized by a wave energy cascade in a wavenumber space and a resulting generation of $E_r \times B$ zonal flows. A spontaneous generation of the turbulent driven $E_r \times B$ zonal flows has been seen also in recent global (gyrokinetic) particle simulations of the electrostatic ITG turbulence [35, 82]. If we assume an adiabatic ion (electron) response for the ETG (ITG) turbulence, the governing gyrokinetic equations become similar for both the ETG and ITG turbulence. Thus, the generation of $E_r \times B$ zonal flows may be a common feature of the drift-wave turbulence.

As is discussed in Chapter 1, generation and damping mechanisms of turbulent driven $E_r \times B$ shear flows are critical issues for understanding the transport properties of negative shear tokamaks, because it is believed that the improved energy confinement is produced by the flow shear suppression of micro-instabilities. Although several flow generation mechanisms such as the self-organization of a magnetized plasma [52] or the turbulent driven Reynolds stress [54] have been proposed, a stability of spontaneously generated $E_r \times B$ shear flows has not been discussed so far. In this chapter, we will study the stability of the $E_r \times B$ zonal flows observed in the simulations of the ETG turbulence, based on the linear theory of the Kelvin-Helmholtz (K-H) mode [56].

As is shown by the Rayleigh necessary condition for instability, in a two-dimensional plasma or a magnetized plasma with a uniform background field, the K-H mode is unstable for $E_r \times B$ shear flows which have an inflection point of flow shear, provided that the system size L_x is sufficiently large compared with a scale length of flow shear L_v, $L_v/L_x < 1$. Therefore, for sustaining quasi-steady $E_r \times B$ zonal flows, some stabilizing effect on the K-H mode is required. Satyanarayana *et al.* have shown a stability condition due to the parallel electron dynamics for the electrostatic K-H mode in a three-dimensional collisionless plasma [83]. This condition was confirmed with a particle simulation [84]. We derive a similar stability condition of the K-H mode for the gyrokinetic Vlasov-Maxwell system describing the ETG turbulence. In a sheared slab configuration, the parallel electron dynamics or $k_\parallel$ is produced by the magnetic shear, and the linear stability of the K-H

mode is related to the q-profile. A linear stability analysis of the electrostatic K-H mode is performed for the negative shear configuration with a gyrokinetic integral eigenvalue code [60], which is extended to include the equilibrium $E_r \times B$ shear flow.

A correspondence between the stability condition for the K-H mode and the flow velocity profile of spontaneously generated $E_r \times B$ zonal flows is found in the simulation results. Also, it is shown that the K-H mode becomes unstable by changing the q-profile to reduce the magnetic shear. An onset of the K-H mode may correspond to a collisionless damping of quasi-steady $E_r \times B$ zonal flows. A possibility of controlling $E_r \times B$ zonal flows and a resulting plasma confinement property is discussed from a point of view of the K-H mode.

5.2 Gyrokinetic finite element PIC code

In this section, we will provide a method for solving a nonlinear gyrokinetic Vlasov-Maxwell system as an initial value problem using a gyrokinetic PIC simulation.

In the present study, we use a sheared slab geometry modeling the negative-sheared magnetic configuration with $q_{\min} \sim 2$ for studying single helicity electrostatic perturbations (or a two-and-a-half dimensional model). In this model configuration, the x-direction corresponds to the radial direction, the z-direction is chosen in the direction of the ambient magnetic field at the $q = 2$ surface, and the y-direction is chosen to be perpendicular to both the x- and z-directions. We assume the periodic boundary condition in the y- (and z-) direction, and the fixed boundary condition in the x-direction. By expanding the q-profile around the $q_{\min}$-surface at $x = 0$, we write the q-profile as $q(x) = q_0 + q_0' x + \frac{1}{2} q_0'' x^2 + \cdots$, where $q_0 = 2 + \delta q_0$, and δq_0, q_0' and q_0'' are evaluated at $x = 0$. We give the corresponding model magnetic field configuration for the negative shear configuration with $q_0' = 0$ as

$$\mathbf{B}(x) = B_0[\mathbf{e}_z - \{\Delta + (x/L_{ns})^2\}\mathbf{e}_y], \tag{5.1}$$

where $\Delta = (\delta q_0 r_0)/(q_0^2 R)$, $L_{ns} = \sqrt{(2q_0^2 R)/(q_0'' r_0)}$, R is the major radius of a toroidal plasma, and r_0 is the minor radius at the $q_{\min}$-surface. In the model magnetic configuration, Eq. (5.1), the resonance condition for the $m/n = 2$ mode is changed from a nonresonant situation to a situation with single or double mode-rational surfaces by varying δq_0 from

a positive to negative value, where m and n are poloidal and toroidal mode numbers, respectively.

Basic equations used in our simulation is the gyrokinetic Vlasov-Maxwell system, Eqs. (2.56), (2.60) and (2.61),

$$\frac{\partial \bar{F}_s}{\partial t} + \left[-\frac{c}{B_0} \nabla_{\bar{\mathbf{R}}} \langle \phi \rangle_{\bar{\theta}} \times \mathbf{b} + \frac{\bar{v}_z}{B_0} \langle \mathbf{B} \rangle_{\bar{\theta}} \right] \cdot \nabla_{\bar{\mathbf{R}}} \bar{F}_s - \frac{q_s}{m_s B_0} \langle \mathbf{B} \rangle_{\bar{\theta}} \cdot \nabla_{\bar{\mathbf{R}}} \langle \phi \rangle_{\bar{\theta}} \frac{\partial \bar{F}_s}{\partial \bar{v}_z} = 0, \tag{5.2}$$

$$n_s(\mathbf{x}, t) = \int \bar{F}_s(\bar{\mathbf{R}}, \bar{v}_z, \bar{M}, t) \delta([\bar{\mathbf{R}} + \bar{\rho}_s] - \mathbf{x}) \bar{D}_s d^6 \bar{\mathbf{Z}}$$

$$- \frac{n_{0s} q_s}{T_s} \sum_{\mathbf{k}} \left[1 - I_0(k_\perp^2 \rho_{ts}^2) \exp(-k_\perp^2 \rho_{ts}^2) \right] \phi_{\mathbf{k}} \exp(i\mathbf{k} \cdot \mathbf{x}), \tag{5.3}$$

$$-\nabla^2 \phi = 4\pi \sum_s q_s n_s(\mathbf{x}), \tag{5.4}$$

where s denotes the particle species. As is discussed in Chapter 2, using the gyrokinetic formalism, we can efficiently describe low frequency micro-instabilities in tokamak plasmas. In solving the gyrokinetic Vlasov-Maxwell system, Eqs. (5.2)-(5.4), we adopt the conventional nonlinear characteristic δf method [85]. We write the distribution function as

$$\bar{F}_s = \bar{F}_{s0} + \delta \bar{F}_s, \tag{5.5}$$

where $\bar{F}_{s0}$ and $\delta \bar{F}_s$ are the equilibrium and perturbed part of the distribution function respectively. It is assumed that $\bar{F}_{s0}$ is a local Maxwellian (2.59). Marker particles are assigned only for $\delta \bar{F}_s$ and the evolution of $\delta \bar{F}_s$ is solved along the nonlinear characteristics of the gyrokinetic equation (5.2):

$$\frac{d\bar{\mathbf{R}}}{dt} = -\frac{c}{B_0} \nabla_{\bar{\mathbf{R}}} \langle \phi \rangle_{\bar{\theta}} \times \mathbf{b} + \frac{\bar{v}_z}{B_0} \mathbf{B}, \tag{5.6}$$

$$\frac{d\bar{v}_z}{dt} = -\frac{q_s}{m_s B_0} \mathbf{B} \cdot \nabla_{\bar{\mathbf{R}}} \langle \phi \rangle_{\bar{\theta}}, \tag{5.7}$$

where the gyro-average for the equilibrium magnetic field is ignored because of the scale length ordering, $\rho / L_{ns} \sim \mathcal{O}(\epsilon)$, and the gyro-average for the electrostatic potential is approximated by a four-point averaging method [49], which is sufficient for perturbations with $k_\perp^2 \rho_{te}^2 \ll 1$. The time integration of the nonlinear characteristics is executed by using a predictor-corrector method. A discrete distribution function of marker particles is given

as

$$\bar{G}_s(\bar{\mathbf{R}}, \bar{v}_z, \bar{M}, t) = \sum_j \delta(\bar{\mathbf{R}} - \bar{\mathbf{R}}_j) \delta(\bar{v}_z - \bar{v}_{zj}) \delta(\bar{M} - \bar{M}_j). \tag{5.8}$$

Defining the particle weight of j-th particle, $\bar{W}_{sj}$, as

$$\bar{W}_s \equiv \left. \frac{\delta \bar{F}_s}{\bar{G}_s} \right|_{\bar{\mathbf{Z}} = \bar{\mathbf{Z}}_j}, \tag{5.9}$$

we write $\delta \bar{F}_s$ as

$$\delta \bar{F}_s(\bar{\mathbf{R}}, \bar{v}_z, \bar{M}, t) = \sum_j \bar{W}_{sj} \delta(\bar{\mathbf{R}} - \bar{\mathbf{R}}_j) \delta(\bar{v}_z - \bar{v}_{zj}) \delta(\bar{M} - \bar{M}_j). \tag{5.10}$$

Substituting Eqs. (5.5), (5.8), (5.9) and (5.10) into the gyrokinetic equation (5.2), the nonlinear evolution equation of the particle weight, $\bar{W}_{sj}$, is obtained as

$$\frac{d\bar{W}_{sj}}{dt} = -\left(\left. \frac{F_{0s}}{\bar{G}_s} \right|_{\bar{\mathbf{Z}} = \bar{\mathbf{Z}}_j(t=0)} - \bar{W}_{sj} \right) \left[\frac{d\bar{\mathbf{R}}}{dt} \cdot \frac{\nabla_{\bar{\mathbf{R}}} F_{0s}}{F_{0s}} + \frac{d\bar{v}_z}{dt} \frac{1}{F_{s0}} \frac{\partial F_{s0}}{\partial \bar{v}_z} \right]_{\bar{\mathbf{Z}} = \bar{\mathbf{Z}}_j(t)}. \tag{5.11}$$

The first factor in Eq. (5.11) reduces to $(1 - \bar{W}_{sj})$ provided that the initial marker particle distribution function is chosen to be the same as the unperturbed distribution function F_{0s}. In our code, uniform particle loading is adopted in order to keep the same numerical resolution in the whole configuration space.

The consistency condition is imposed by the Poisson equation (5.4). Since we consider relatively short wavelength perturbations with $k_\perp \lambda_{De} \leq 1$, an ion response is assumed to be adiabatic under the ordering of $k_\perp^2 \rho_{ti}^2 \gg 1$. It is noted that in Chapter 4, we have shown that the ETG modes are unstable for $k_\perp \lambda_{De} \leq 1$ ($k_\perp^2 \rho_{te}^2 \ll 1$ for typical fusion plasma parameters satisfying $\rho_{te}^2 / \lambda_{De}^2 \ll 1$). By applying the long wavelength approximation, $k_\perp^2 \rho_{te}^2 \ll 1$, to the electron polarization density (the second term in Eq.(5.3)), we write the electron density as

$$n_e(\mathbf{x}, t) = n_{0e} + \int \delta \bar{F}_e(\bar{\mathbf{R}}, \bar{v}_z, \bar{M}, t) \delta([\bar{\mathbf{R}} + \bar{\rho}_e] - \mathbf{x}) \bar{D}_e d^6 \bar{\mathbf{Z}} - \nabla_\perp \cdot \frac{e n_{0e}}{T_e} \rho_{te}^2 \nabla_\perp \phi. \tag{5.12}$$

From Eqs. (5.4) and (5.12), we obtain the gyrokinetic Poisson equation for electron modes,

$$-\left(\nabla^2 + \nabla_\perp \cdot \frac{\rho_{te}^2}{\lambda_{De}^2} \nabla_\perp \right) \phi + \frac{1}{\lambda_{Di}^2} \phi = -4\pi e \int \delta \bar{F}_e(\bar{\mathbf{R}}, \bar{v}_z, \bar{M}, t) \delta([\bar{\mathbf{R}} + \bar{\rho}_e] - \mathbf{x}) \bar{D}_e d^6 \bar{\mathbf{Z}}. \tag{5.13}$$

While the electron adiabatic response for modes with $\omega/k_\parallel \ll v_{te}$. e.g., the ITG mode, is produced by a fast passing motion of thermal electrons (see Section 2.4), the ion adiabatic response for modes with $k_\perp^2\rho_{ti}^2 \gg 1$ comes from the ion polarization density. Therefore, adiabatic ions also respond to $k_y = k_z = 0$ component of the electrostatic potential. The gyrokinetic Poisson equation, Eq. (5.13) is solved using a finite element PIC method [33]. By introducing the finite elements, we write the electrostatic potential ϕ and the perturbed electron guiding-center density δg_e as

$$\phi(x,y) = \sum_k \phi_k \Lambda_k(x,y), \tag{5.14}$$

$$\delta g_e(x,y) = \sum_k \delta g_{ek} \Lambda_k(x,y), \tag{5.15}$$

$$\Lambda_k(x,y) = S_{ix}(x) S_{iy}(y), \tag{5.16}$$

where $k = ix + N_y(iy-1)$, $ix = 1 \sim N_x$, $iy = 1 \sim N_y$, and N_x, N_y are the system size in the x- and y-directions, respectively. For a two-dimensional basis (5.16), we use a quadratic spline function, $S_{ix}(x)$ and $S_{iy}(y)$. A matrix form of the gyrokinetic Poisson equation is written as

$$\sum_k \mathcal{M}_{kl}\phi_k = \delta g_{el}, \tag{5.17}$$

$$\mathcal{M}_{kl} = -\frac{1}{4\pi e}\int\left[\left(1+\frac{\rho_{te}^2}{\lambda_{De}^2}\right)\nabla_\perp\Lambda_k\cdot\nabla_\perp\Lambda_l + \frac{1}{\lambda_{Di}^2}\Lambda_k\Lambda_l\right]d\mathbf{x}, \tag{5.18}$$

$$\delta g_{el} = \sum_j \bar{W}_{ej}\frac{1}{2\pi}\int\int \Lambda_l(x,y)\delta([\bar{\mathbf{R}}_j + \bar{\rho}_{ej}] - \mathbf{x})d\mathbf{x}\bar{D}_e d\bar{\theta}, \tag{5.19}$$

where the four-point averaging method is used also for the gyro-average in Eq.(5.19) so as not to generate a self-force. It is noted that in this algorithm, point particles are used. In a finite element PIC method, sub-grid-scale noises are suppressed by spline functions for the two-dimensional basis Λ_k, while in the standard PIC simulation, such a noise is excluded by a form factor of finite-size-particles. In the code, the time independent linear operator (5.18) is decomposed by using a Choleski decomposition in the initial time step. In each time steps, ϕ_k is obtained efficiently by calculating a back-substitution.

As is shown in Chapter 2, the gyrokinetic Vlasov-Maxwell system is formulated so as not to lose the inherent nature of the Hamiltonian system, and has the energy conservation property, Eq. (2.104). Also for the reduced gyrokinetic Vlasov-Maxwell system, Eqs. (5.2)-(5.4), an energy conservation law is written as,

$$\frac{d}{dt}\int\frac{1}{2}m_e\bar{v}_z^2\bar{F}_e\bar{D}_e d^6\bar{\mathbf{Z}} + \frac{d}{dt}\frac{1}{8\pi}\int\left[|\nabla\phi|^2 + \frac{\rho_{te}^2}{\lambda_{De}^2}|\nabla_\perp\phi|^2 + \frac{1}{\lambda_{Di}^2}|\phi|^2\right]d^3\mathbf{x} = 0. \tag{5.20}$$

In order to estimate the accuracy of the simulation, this energy conservation law is checked by varying a number of marker particles.

5.3 Simulation results

In this section, we will show gyrokinetic PIC simulations of the ETG turbulence. In Chapter 4, we have already studied linear properties of the slab ETG mode. From an estimation of the transport coefficient based on the mixing length theory, we have shown that the negative-sheared slab ETG (NS-ETG) mode gives an order of magnitude larger transport coefficient compared with that for the conventional normal-sheared slab ETG mode. Also, it has been shown that among several branches of the NS-ETG mode, the nonresonant mode, which has a bounded solution due to the magnetic shear, plays the most significant role in the electron anomalous transport. Therefore, in the present study, we limit ourselves to nonlinear simulations of the nonresonant mode in the negative shear configuration.

The TFTR like parameters shown in Table 3.1 are used also in this chapter. The model magnetic configuration is given with $L_{ns} = 0.624 \sim 1.25$m and $\Delta = 4\times10^{-5}$ ($\delta q_0 = 0.0022$). The system sizes in the x- and y-directions are $N_x = 128 \sim 256$ and $N_y = 16 \sim 64$, respectively, with the unit length or the grid size of $\Delta x = 1.43\bar{\lambda}_{De} = 4.57\bar{\rho}_{te}$. It is noted that for the present plasma parameter, the scale length of the ETG mode is characterized by the electron Debye length, since $\bar{\lambda}_{De}^2/\bar{\rho}_{te}^2 \sim 10$. And, this grid size Δx is sufficient for resolving the ETG modes with $k_\perp\lambda_{De} \sim 1$. The density and temperature profiles with constant gradient parameters , L_{ne} and L_{te}, are chosen as in Section 4.4,

$$n_{0e}(x) = \frac{\bar{n}_{0e}(L_x/L_{ne})\exp[-(x-L_x/2)/L_{ne}]}{1-\exp(-L_x/L_{ne})}, \tag{5.21}$$

$$T_{0e}(x) = \frac{\bar{T}_{0e}(L_x/L_{te})\exp[-(x-L_x/2)/L_{te}]}{1-\exp(-L_x/L_{te})}, \tag{5.22}$$

where $L_x = N_x\Delta x$. In the simulations, a typical time step is chosen as $\Delta t \sim 0.349\Omega_i^{-1}$.

5.3.1 Linear theory and convergence

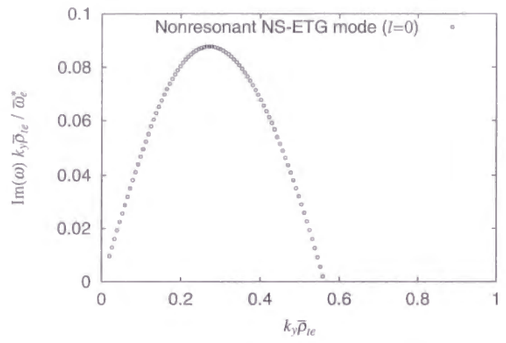

Figure 5.1: k_y-dependence of the growth rate spectrum of the $l = 0$ branch of the nonresonant NS-ETG mode is plotted for the single-helicity configuration ($k_\parallel = \mathbf{k} \cdot \mathbf{B}/B$) with $\eta_e = \eta_i = 5$ and $L_{ne}/L_{ns} = 0.430$.

In Fig. 5.1, the k_y-dependence of the linear growth rate, which is obtained with a gyrokinetic integral eigenvalue code, is plotted for the $l = 0$ branch of the nonresonant NS-ETG mode with $\eta_e = \eta_i = 5$ and $L_{ne}/L_{ns} \sim 0.430$. Since the shortest wavelength included in the simulation system is $k_y \bar{\rho}_{te} \sim 0.687$, the grid size is sufficient for resolving stable modes (or energy sink) in the k_y spectrum of the ETG turbulence. It is noted that the k_x spectrum of the corresponding linear eigenfunction has an amplitude for $k_x \bar{\rho}_{te} < 0.2$. The system size in the x-direction is chosen so that the boundary condition does not affect the simulation result. Figure 5.2 shows the η_e-dependence of the growth rate obtained from both the gyrokinetic integral eigenvalue code and the gyrokinetic PIC code. Parameters used in this comparison are $L_{ne}/L_{ns} \sim 0.430$, $N_x \times N_y = 128 \times 16$, and a marker particle number of 512 particles par a cell. The growth rates of the fastest growing mode agree well in both results.

Figure 5.3 shows a convergence check with respect to a volume averaged electron thermal transport coefficient $\bar{\chi}_e$ by changing a number of marker particle in a single cell for the simulation with $\eta_e = \eta_i = 5$, $L_{ne}/L_{ns} \sim 0.430$, and $N_x \times N_y = 256 \times 16$. Here, the flux surface averaged electron thermal transport coefficient χ_e, the volume averaged electron

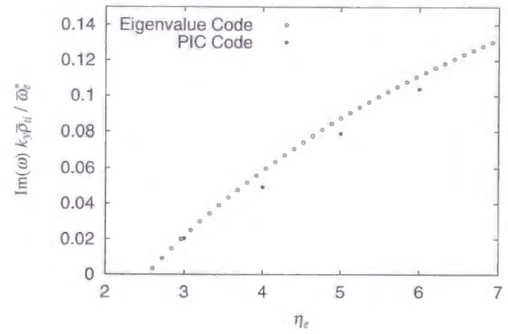

Figure 5.2: η_e-dependence of the linear growth rate of the nonresonant NS-ETG modes with $k_y \rho_{te} = 0.258$ is compared between the gyrokinetic integral eigenvalue code and the gyrokinetic PIC code.

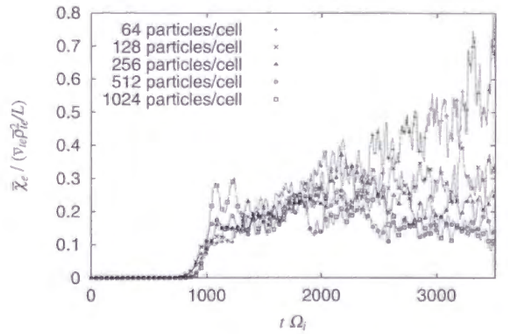

Figure 5.3: The volume averaged electron thermal transport coefficient $\bar{\chi}_e$ is plotted for the simulations of the nonresonant NS-ETG mode with a different number of marker particles. $\bar{\chi}_e$ is converged with a particle number of ≥ 512 particles par a cell.

thermal transport coefficient $\bar{\chi}_e$, and the electron heat flux Q_e are defined as

$$\chi_e(x) = -\int Q_e/p'_{0e}dy, \tag{5.23}$$

$$\bar{\chi}_e = -\int\int Q_e/p'_{0e}dxdy, \tag{5.24}$$

$$Q_e(x,y) = \sum_k [\delta p_{ek}\Lambda_k(x,y)]\,[-c/B_0\phi_k\nabla\Lambda_k(x,y)\times\mathbf{b}\cdot\mathbf{e}_x]\,, \tag{5.25}$$

$$\delta p_{ek} = \sum_j (m_e\bar{v}_{zj}^2/2 + \bar{M}_j\Omega_e)\bar{W}_{ej}\frac{1}{2\pi}\int\int\Lambda_l(x,y)\delta([\bar{\mathbf{R}}_j + \bar{\rho}_{ej}] - \mathbf{x})d\mathbf{x}\bar{D}_e d\bar{\theta}, \tag{5.26}$$

where $p_{0e} = \frac{3}{2}n_{0e}T_{0e}$. As the marker particles increase, $\bar{\chi}_e$ in the saturated state approaches to $\bar{\chi}_e \sim 0.15\bar{v}_{te}\bar{\rho}_{te}^2/L$, where $L^{-1} = L_{ne}^{-1} + L_{te}^{-1}$, and $\bar{v}_{te}\bar{\rho}_{te}^2/L$ corresponds to $0.42\mathrm{m}^2/\mathrm{s}$ for the present simulation parameters. It is noted that the absolute value of $\bar{\chi}_e$ is different from χ_e, because the linearly stable region with $\chi_e \sim 0$ is involved in the simulation system with single-helicity perturbations. In this test, a particle number of more than 512 particles par a cell is required for obtaining a convergence of $\bar{\chi}_e$. Since the maximum amplitude of the electrostatic potential in the saturated state is very small $e\phi/T_e < 0.01$, a simulation of the ETG turbulence is sensitive to the noise due to discrete particles. Thus, an order of magnitude larger number of marker particles are required for a good convergence than that in a gyrokinetic PIC simulation of the ITG turbulence [34, 35], in which a marker particle number of less than 10 particles par a cell is usually used. In the simulation results shown in the following, we have adopted a marker particle number of 512 particles par a cell.

5.3.2 Nonlinear evolution of ETG turbulence

In Figs. 5.4(a)-5.4(d), contour plots of the electrostatic potential are shown for the simulation of the nonresonant NS-ETG mode with $\eta_e = \eta_i = 5$, $L_{ne}/L_{ns} \sim 0.430$, and $N_x \times N_y = 256 \times 64$. Figures 5.5(a) and 5.5(b) show time evolution of the k_y spectrum of the electrostatic field energy observed in a region around the $q_{\min}$-surface ($x/\bar{\rho}_{te} = -146.2 \sim 146.2$) and in a $E_r \times B$ zonal flow region ($x/\bar{\rho}_{te} = -361.1 \sim -287.9$), respectively.

In the linear phase for $t\Omega_i = 0 \sim 1100$ [see Fig. 5.4(a)], the radially elongated vortex structure appears. The k_y spectrum in Fig. 5.5(a) peaks at $k_y\bar{\rho}_{te} = 0.258$ where the maximum linear growth rate is given in Fig. 5.2. As is discussed in Chapter 4, the broad

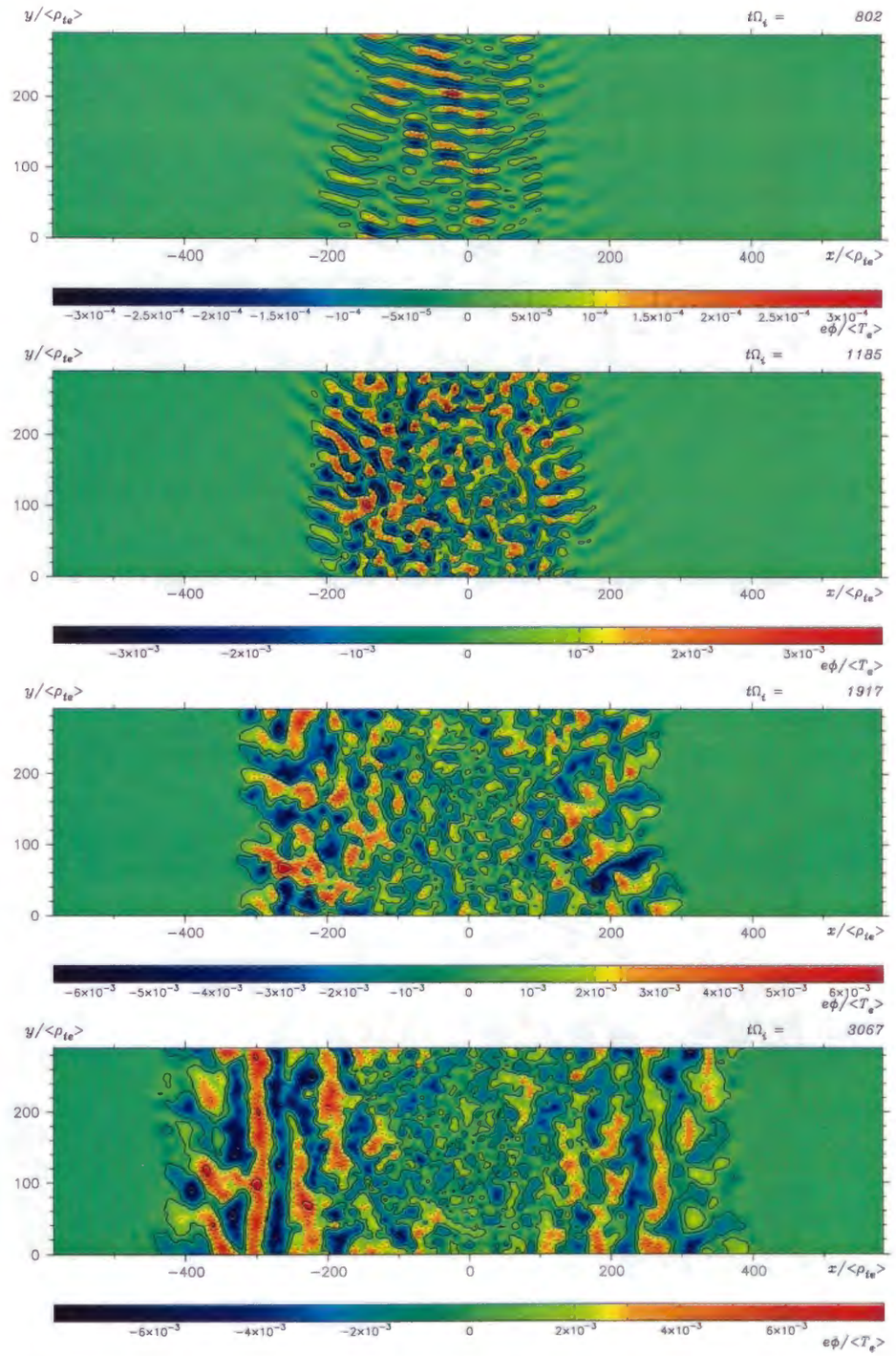

Figure 5.4: Contour plots of ϕ at $t\Omega_{ci} = 802, 1185, 1917, 3067$ are shown for the simulation of the nonresonant NS-ETG mode with $\eta_e = \eta_i = 5$, $L_{ne}/L_{ns} \sim 0.430$, and $N_x \times N_y = 256 \times 64$. The $q_{\min}$-surface is $x/\bar{\rho}_{te} = 0$.

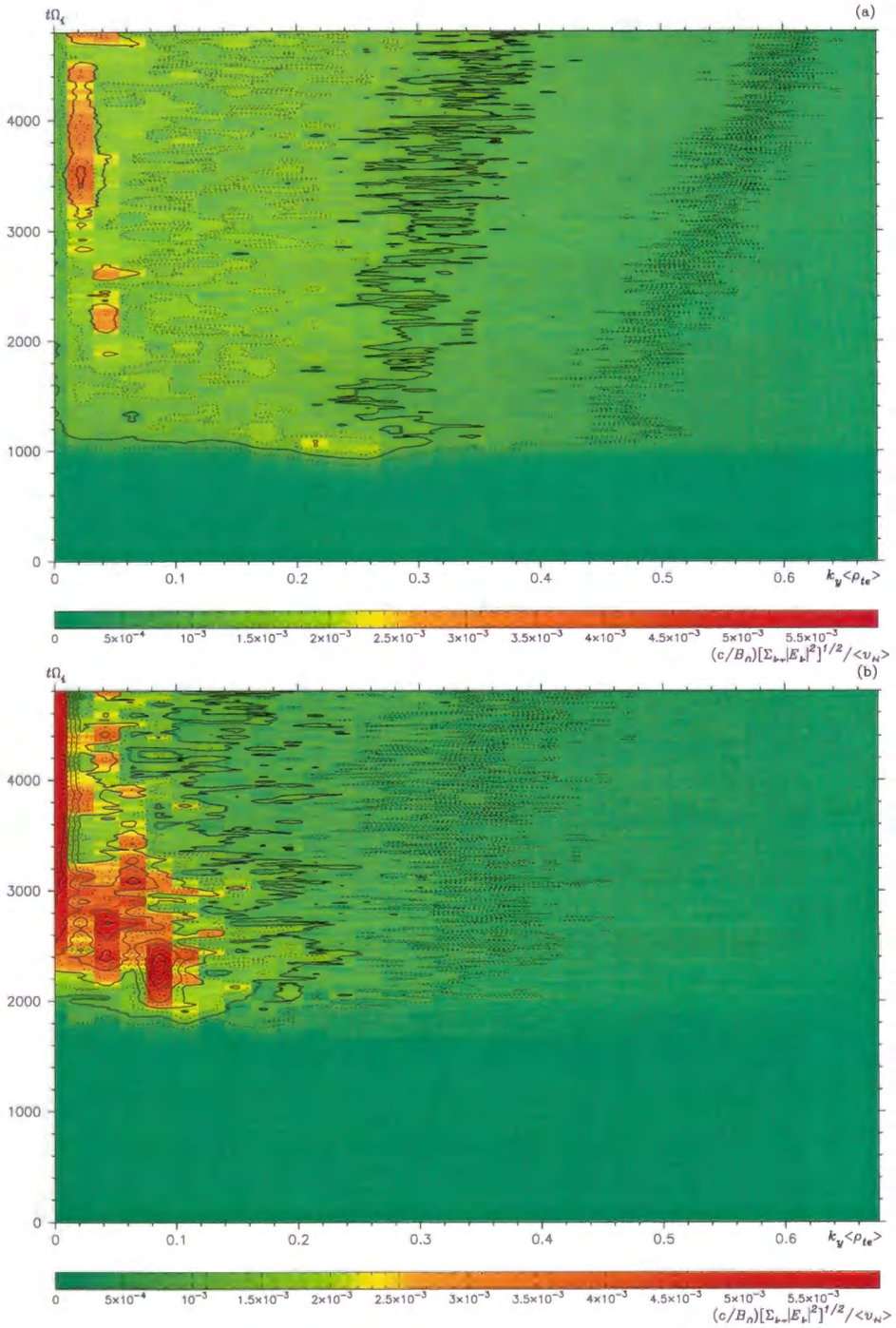

Figure 5.5: Time histories of k_y spectrum of $[\sum_{k_x}|E_k|^2]^{1/2}$ observed in the simulation of the nonresonant NS-ETG mode shown in Fig. 5.4. The observation regions are set for (a) $x/\bar{\rho}_{te} = -146.2 \sim 146.2$ and (b) $x/\bar{\rho}_{te} = -361.1 \sim -287.9$.

radial eigenmode structure is a characteristic feature of the NS-ETG modes which becomes unstable in a weak magnetic shear region around the $q_{\min}$-surface.

A saturation of the nonresonant NS-ETG mode occurs around $t\Omega_{te} \sim 1100$. In the initial saturation phase [see Fig. 5.4(b)], the radially elongated vortices are broken into small scale and almost isotropic eddies. A destruction of the radially elongated vortices is caused by $E \times B$ shear flows with $k_y \sim 0$, which is generated by a local charge separation arising from the electron particle transport. This process is recognized as a normal cascade in the k_x space. Also, in Fig. 5.5(a), we see an inverse cascade process in the k_y space. This property of the wave energy cascade in a relatively long wavelength regime with $k_\perp \rho_{te} < 1$ is consistent with a picture of a self-organization process in the electrostatic drift-wave turbulence, which was discussed based on the Hasegawa-Mima equation [86]. It is noted that, through the whole time evolution, a variation of the electron temperature is estimated as $\delta T_e/T_{0e} \leq 0.005$. Also, a modification of the velocity distribution function due to a particle trapping is weak, because of a small saturation amplitude with $e\phi/T_e \leq 0.003$ in the initial saturation phase. Therefore, in the present simulation, the dominant nonlinear saturation mechanism is not the quasi-linear relaxation of the background temperature profile or a flattening of the velocity distribution function due to a particle trapping. An important saturation mechanism is considered to be an inverse (normal) energy cascade process in the k_y (k_x) space which generates $E \times B$ shear flows with $k_y \sim 0$.

After the initial nonlinear saturation of the unstable ETG modes [see Fig. 5.4(c)], for $t\Omega_i = 1200 \sim 2300$, a low-$k_y$ secondary instability occurs in a linearly stable region in both sides of the nonlinearly saturated region around the $q_{\min}$-surface. The wave number of the secondary instability is estimated as $k_y\bar{\rho}_{te} = 0.0859$ in Fig. 5.5(b). This unstable k_y region can not be explained by the linear growth rate of the ETG mode which peaks around $k_y\bar{\lambda}_{De} \sim 1$ ($k_y\bar{\rho}_{te} \sim 0.3$). We will discuss about a mechanism of this instability later. The k_y spectrum shown in Fig. 5.5(b) also shows the inverse energy cascade during the evolution of the secondary instability. This inverse energy cascade process leads to a generation of strong $E_r \times B$ zonal flows.

Finally, in the quasi-stationary phase after $t\Omega_i \sim 2400$ [see Fig. 5.4(d)], the wave energy condenses into the $k_y = 0$ mode, which means a formation of $E_r \times B$ zonal flows.

Then, the expansion of the secondary instability region is suppressed.

5.3.3 Effects of $E \times B$ zonal flow on χ_e

Figure 5.6 shows a time history of $\bar{\chi}_e$ obtained from simulations with and without the $k_y = 0$ mode or the $E_r \times B$ zonal flows. The generation of the $E_r \times B$ zonal flow greatly decreases $\bar{\chi}_e$ in the quasi-stationary phase, where the $E_r \times B$ zonal flows are fairly strong. It is noted that in the initial saturation phase, both results show a similar behavior, because in this phase, an important process is not a generation of $E_r \times B$ zonal flows with $k_y = 0$ but an inverse energy cascade into $k_y \sim 0$ modes [see Fig. 5.5(a)].

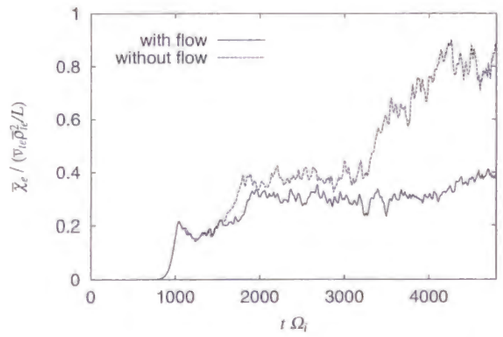

Figure 5.6: $\bar{\chi}_e$ is plotted for the simulation of the nonresonant NS-ETG mode with and without $k_y = 0$ component of the electrostatic potential ($E_r \times B$ zonal flow). Simulation parameters are the same as in Fig. 5.4.

Figures 5.7(a) and 5.7(b) show time histories of the radial distributions of the ($k_y = 0$) $E_r \times B$ flow $v_{E_r \times B}(x)$ and the electron thermal transport coefficient $\chi_e(x)$, respectively. At the end of the linear growth phase at $t\Omega_i \sim 1100$, a large χ_e region produced by the radially elongated linear vortex structure is observed around the $q_{\min}$-surface at $x = 0$. After the saturation of the nonresonant NS-ETG mode, this large χ_e region disappears, because the radially elongated linear vortex structure is decorrelated due to the $E \times B$ shear flows with $k_y \sim 0$. Then, large χ_e regions arising from the secondary instability propagates in the radial direction for $t\Omega_i = 1100 \sim 2300$. A generation of the $E_r \times B$ zonal flow is observed

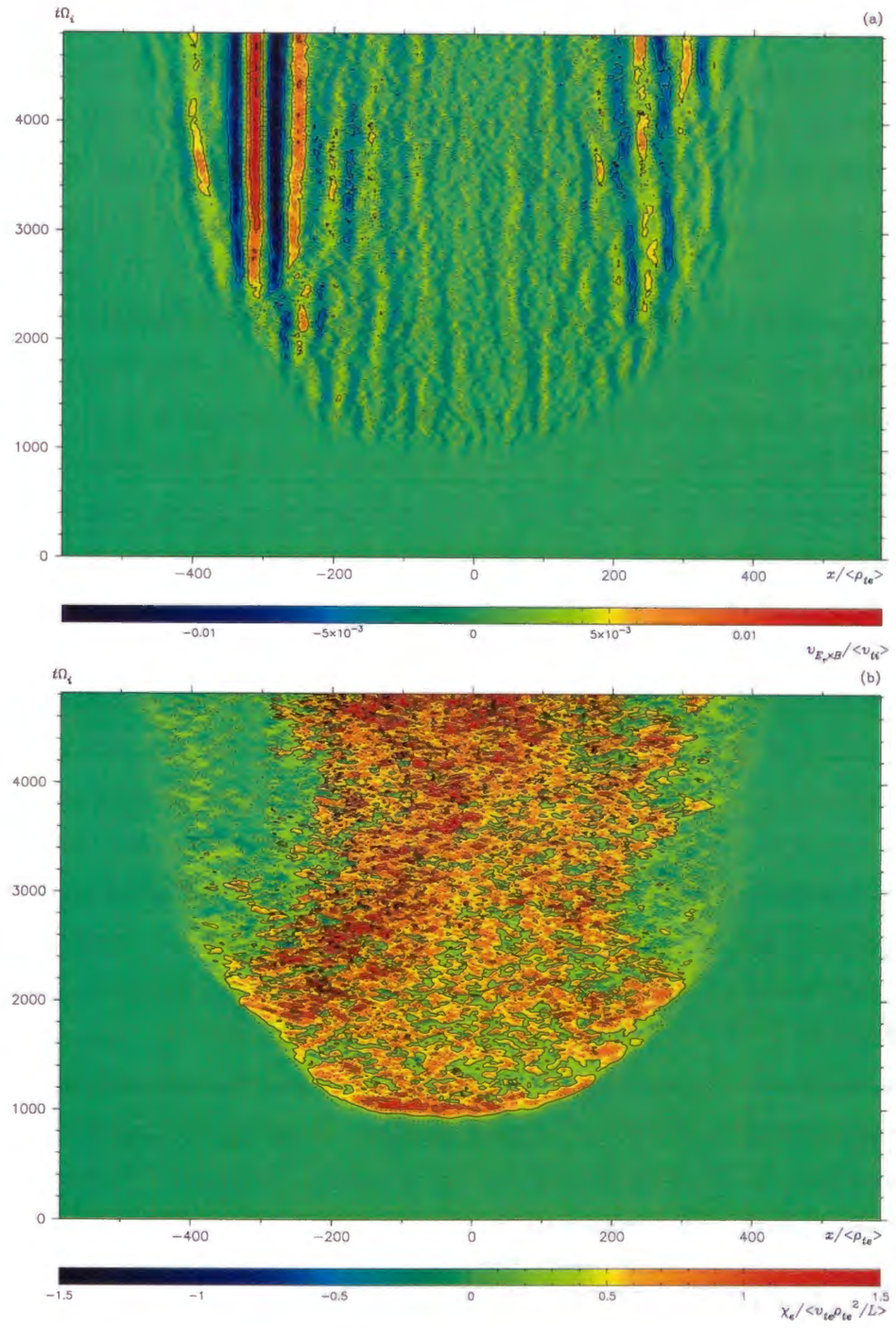

Figure 5.7: Time histories of the radial distributions of (a) the $E_r \times B$ flow velocity $v_{E_r \times B}$ and (b) the electron thermal transport coefficient χ_e are plotted for the simulation of the nonresonant NS-ETG mode shown in Fig. 5.4. A generation of the quasi-steady $E_r \times B$ zonal flow and a remarkable reduction of χ_e in the $E_r \times B$ zonal flow region are observed.

during the nonlinear saturation of the secondary instability. The $E_r \times B$ zonal flow velocity has a large amplitude $v_{E_r \times B} \leq 0.015\bar{v}_{ti}$ in finite magnetic shear regions in both sides of the $q_{\min}$-surface compared with that observed in a region of the $q_{\min}$-surface $v_{E_r \times B} \leq 0.002\bar{v}_{ti}$. After $t\Omega_i \sim 2400$, the quasi-steady $E_r \times B$ zonal flow pattern is sustained. It is noted that in the present simulation model, a flow damping effect due to a dissipation such as a Coulomb collision is not involved, because the growth time of the ETG mode is shorter than that of the ITG mode. In the k_y spectrum of the electrostatic potential fluctuation in the large $E_r \times B$ zonal flow region shown in Fig. 5.5(b), finite k_y modes, which contributes to the anomalous particle and heat fluxes, have relatively small amplitudes, because of an inverse energy cascade into $k_y = 0$ mode. An absence of finite k_y modes corresponds to a remarkable reduction of χ_e in the large $E_r \times B$ zonal flow region. This reduction of χ_e explains the difference of $\bar{\chi}_e$ in the quasi-stationary phase between results obtained with and without the $k_y = 0$ mode or $E_r \times B$ zonal flows [see Fig. 5.6].

The obtained radial profile of the quasi-steady $E_r \times B$ zonal flow is non-uniform and has a fairly large flow velocity in the small χ_e region in both sides of the $q_{\min}$-surface. In a region of the $q_{\min}$-surface where the nonresonant NS-ETG mode is unstable, such a quasi-steady $E_r \times B$ zonal flow is not seen. Although an inverse energy cascade in the k_y space is observed both in the region of the $q_{\min}$-surface [see Fig.5.5(a)] and in the large $E_r \times B$ zonal flow region [see Fig.5.5(b)], the wave spectrum condensation into the $k_y = 0$ mode occurs only in the latter region. In other words, it seems that the $k_y = 0$ mode or $E_r \times B$ zonal flows can not be sustained in the former region. Since the main difference between these two regions is the magnetic shear, we suppose that the magnetic shear plays a significant role for sustaining the $E_r \times B$ zonal flows. In order to confirm this conjecture, in the next section, we will discuss about a stability of the $E_r \times B$ zonal flow from a point of view of the K-H instability.

5.4 Stability of $E \times B$ zonal flow

In this section, we discuss a stability of the $E_r \times B$ zonal flow. Using a gyrokinetic integral eigenvalue code, we analyze a linear stability of the K-H mode for a model $E_r \times B$ shear flow,

which is chosen based on $E_r \times B$ zonal flows observed in the gyrokinetic PIC simulation. Numerical results indicate a correlation between the observed $E_r \times B$ zonal flow profile and the K-H instability. Also, an evidence of the K-H instability is seen in the gyrokinetic PIC simulation, in which the equilibrium q-profile is changed during the quasi-stationary phase after the nonlinear saturation.

5.4.1 Linear theory of K-H mode

In order to analyze a slab plasma with the equilibrium $E_r \times B$ flow, we extend the gyrokinetic Vlasov-Maxwell system, Eqs. (5.2)-(5.4), to include an equilibrium part of the electrostatic potential Φ. Since an obtained amplitude of the electrostatic potential which produces the quasi-steady $E_r \times B$ zonal flow is very small $e\Phi/T_e < 0.01$, we treat an equilibrium electrostatic potential Φ as a quantity of the same order as the electrostatic fluctuating potential ϕ. Also, since the corresponding $E_r \times B$ flow velocity is small compared with the thermal velocity, $v_{E_r \times B} \sim 0.015\bar{v}_{ti}$, a correction to the definition of the magnetic moment is not needed in the present analysis. We then write a linear gyrokinetic Vlasov-Maxwell system for gyrokinetic electrons and adiabatic ions as

$$\frac{\partial \bar{F}_{1e}}{\partial t} + \frac{\bar{v}_z}{B_0}\mathbf{B} \cdot \nabla_{\bar{\mathbf{R}}} \bar{F}_{1e} - \frac{c}{B_0}\nabla_{\bar{\mathbf{R}}}\Phi \times \mathbf{b} \cdot \nabla_{\bar{\mathbf{R}}} \bar{F}_{1e}$$
$$- \frac{c}{B_0}\nabla_{\bar{\mathbf{R}}}\langle\phi\rangle_{\bar{\theta}} \times \mathbf{b} \cdot \nabla_{\bar{\mathbf{R}}} \bar{F}_{0e} + \frac{e}{m_e B_0}\mathbf{B} \cdot \nabla_{\bar{\mathbf{R}}}\langle\phi\rangle_{\bar{\theta}} \frac{\partial \bar{F}_{0e}}{\partial \bar{v}_z} = 0, \tag{5.27}$$

$$n_{1e}(\mathbf{x}, t) = \int \bar{F}_{1e}(\bar{\mathbf{R}}, \bar{v}_z, \bar{M}, t)\delta([\bar{\mathbf{R}} + \bar{\rho}_e] - \mathbf{x})\bar{D}_e d^6\bar{\mathbf{Z}} - \nabla_\perp \cdot \frac{en_{0e}}{T_e}\rho_{te}^2 \nabla_\perp \phi, \tag{5.28}$$

$$-\nabla^2\phi + \frac{1}{\lambda_{Di}^2}\phi = -4\pi e n_{1e}, \tag{5.29}$$

where the gyro-average for Φ and the electron polarization density arising from Φ are ignored because $\rho_{te}/L_v \ll 1$, and L_v is a scale length of the $E_r \times B$ flow velocity shear. Equations (5.27)-(5.29) are derived using the same approximation as in the simulation system in order to analyze an equilibrium configuration which is realized in a quasi-steady state of the gyrokinetic PIC simulation. By eliminating $\bar{F}_{1e}$ and n_{1e} in Eqs. (5.27)-(5.29), the gyrokinetic integral eigenmode equation is derived as

$$\sum_{k_l} \mathcal{L}_{k_m, k_l}(\omega)\phi_{k_l} = 0 \tag{5.30}$$

$$\mathcal{L}_{k_m,k_l}(\omega) \equiv \frac{1}{2L_x}\int_{-L_x}^{L_x} dx \exp[i(k_l-k_m)x]$$
$$\times\left[-\left(1+\frac{\rho_{te}^2}{\lambda_{De}^2}\right)(k_l^2+k_y^2+k_z^2)+\frac{d}{dx}\left(\frac{\rho_{te}^2}{\lambda_{De}^2}\right)ik_l-\frac{1}{\lambda_{Di}^2}\right.$$
$$\left.+\frac{1}{\lambda_{De}^2}\left[\left\{\Gamma_0-\eta_e\left(\frac{1}{2}+b_{ae}\right)\Gamma_0+\eta_e b_{ge}\Gamma_1\right\}\xi_e^* Z_e+\Gamma_0(\eta_e\xi_e^*\xi_e-1)(1+\xi_e Z_e)\right]\right], \quad (5.31)$$

where the definitions of quantities are the same as in Eqs. (3.14) and (3.15) except for the effect of the equilibrium $E_r \times B$ flow, $v_{E_r\times B} = -c/B_0 \nabla\Phi\times\mathbf{b}\cdot\mathbf{e}_y$, which appears as a Doppler shift for an eigenfrequency, $\xi_e = [\omega - k_y v_{E_r\times B}]/(\sqrt{2}|k_\parallel|v_{te})$.

Before showing the numerical solution of the gyrokinetic integral eigenvalue code, we shortly discuss the properties of the K-H mode analytically in the limit: $k_\perp\rho_{te} \to 0$, $L_{ne} = L_{ni} \to \infty$, $L_{te} = L_{ti} \to \infty$, $L_{ns} \to \infty$, and $n_{1i} \to 0$. In this limit, the gyrokinetic integral eigenmode equation reduces to a simple differential eigenmode equation,

$$\frac{d^2\phi}{dx^2}+\left[-k_y^2\phi+\frac{k_y v''_{E_r\times B}}{\omega-k_y v_{E_r\times B}}+\frac{\bar{v}_{te}^2 k_\parallel^2}{\bar{\lambda}_{De}^2(\omega-k_y v_{E_r\times B})^2}\right]\phi=0, \quad (5.32)$$

where the plasma dispersion function is approximated as $Z_e \sim -\xi_e^{-1}-\frac{1}{2}\xi_e^{-3}-\cdots$ under the fluid limit $\xi_e \gg 1$. This eigenmode equation is mathematically identical to the well-known Rayleigh equation describing the K-H mode in a weakly inhomogeneous neutral fluid in a gravitational field [56]. In Eq. (5.32), the parallel electron dynamics (the third term in square parenthesis), which comes from an effect of the magnetic shear, plays a role of buoyancy in a neutral fluid under a gravitational field [83]. In Eq. (5.32), a non-dimensional parameter corresponding to the Richardson number in a neutral fluid is given by

$$J = \frac{k_\parallel^2}{k_y^2}\frac{(L_v/\bar{\lambda}_{De})^2}{(v_0/\bar{v}_{te})^2}, \quad (5.33)$$

where v_0 is a characteristic flow velocity. The marginal stability condition of the K-H mode was analytically obtained for the flow shear profile of $v_{E_r\times B} = v_0\tanh(x/L_v)$ as [87]

$$J = k_y^2 L_v^2(1-k_y^2 L_v^2). \quad (5.34)$$

From this relation, the unstable k_y and $k_\parallel$ regions are respectively written as

$$0 < k_y L_v < 1, \quad (5.35)$$

and

$$0 < k_\parallel L_v < \frac{v_0/\bar{v}_{te}}{L_v/\bar{\lambda}_{De}} k_y^2 L_v^2\sqrt{1-k_y^2 L_v^2}. \quad (5.36)$$

From the condition (5.36), the K-H mode is completely stabilized for

$$k_\parallel L_v > \frac{1}{2\sqrt{2}}\frac{v_0/\bar{v}_{te}}{L_v/\bar{\lambda}_{De}}. \quad (5.37)$$

In the limit of $k_\parallel \to 0$, we have recovered the growth rate spectrum of the electrostatic K-H mode for $v_{E_r\times B} = v_0\tanh(x/L_v)$ [88]. This branch is numerically traced by changing various equilibrium parameters, and the electrostatic K-H mode is identified in the negative shear configuration.

The equilibrium electron distribution function $\bar{F}_{e0}$ is chosen as a local Maxwellian (2.59). It is noted that in a slab geometry, a local Maxwellian is also an equilibrium solution of the gyrokinetic Vlasov-Maxwell system including an equilibrium potential $\Phi(x)$, because the unperturbed characteristics satisfy $\dot{\bar{R}}_x = 0$. The equilibrium density profile $n_{0e}(x)$ which is consistent with $\Phi(x)$ is determined using the Poisson equation,

$$-\nabla^2\Phi+\frac{1}{\lambda_{Di}^2}\Phi = 4\pi e(n_{0i}-n_{0e}), \quad (5.38)$$

where n_{0i} is chosen as the same profile as Eq. (5.21), and we assume a deviation from the original equilibrium profile (5.21) for the electron density n_{0e} as in the simulation. Although the observed $E_r \times B$ zonal flow has a global oscillatory profile with multiple periods, we assume a model $E_r \times B$ flow profile with a single period and analyze a relatively localized mode in order to understand characteristics of the K-H mode. We write a model $E_r \times B$ flow profile as

$$v_{E_r\times B}(x) = v_0[x-x_c]/L_v \exp\{-([x-x_c]/L_v)^2/2+1/2\}, \quad (5.39)$$

where v_0 is a peak velocity and x_c is a position of a neutral point of the $E_r \times B$ flow. In Fig. 5.8(a), a model $E_r \times B$ flow (5.39) with $L_v \sim 14.4\bar{\rho}_{te}$ is plotted for a case with $x_c = 0$, where a scale length of flow shear $L_v = \pi/(2k_x)$ is chosen based on the k_x spectrum of the observed $E_r \times B$ zonal flow which peaks at $k_x\bar{\rho}_{te} \sim 0.109$. The corresponding electron density profile calculated from Eq. (5.38) is plotted in Fig. 5.8(b). The other parameters are chosen as the same as the simulation parameters given in Section 5.3.

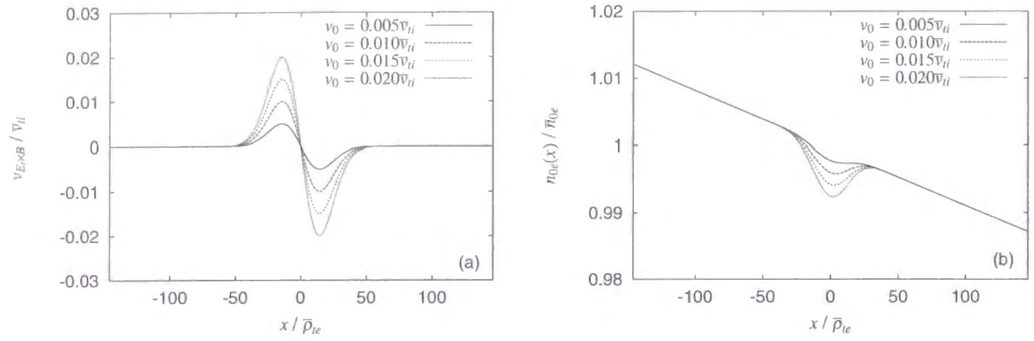

Figure 5.8: (a) model equilibrium $E_r \times B$ flows and (b) the corresponding electron density profiles used in a calculation of the electrostatic K-H mode are shown for $L_v \sim 14.4\bar{\rho}_{te}$, and $x_c = 0$.

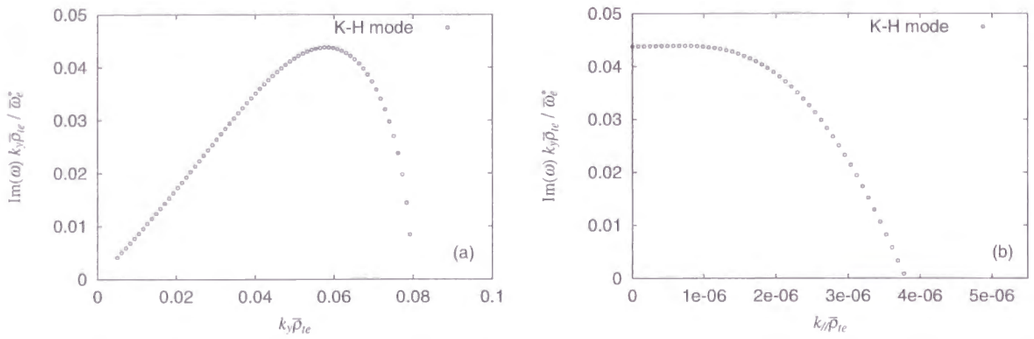

Figure 5.9: (a) k_y-dependence and (b) $k_\parallel$-dependence of the growth rate spectrum of the electrostatic K-H mode are plotted for $k_\parallel = 0$ and $k_y\bar{\rho}_{te} = 0.0580$, respectively. The equilibrium parameters are chosen as $L_{ne}/L_{ns} = 0$, $L_v \sim 14.4\bar{\rho}_{te}$, $v_0 \sim 0.02\bar{v}_{ti}$, and $x_c = 0$. Other parameters are the same as the simulation parameter.

First, we show the growth rates obtained for a shearless slab configuration and discuss about basic properties of the K-H mode. Equilibrium parameters are the same as the simulation parameters, and the model $E_r \times B$ flow profile with $L_v \sim 14.4\bar{\rho}_{te}$ and $x_c = 0$ is used [see Fig. 5.8(a)]. Figure 5.9(a) shows the k_y-dependence of the growth rate of the K-H mode. In the growth rate spectrum, the marginally stable k_y is estimated as $k_y L_v \sim 1.15$, and the peak of the growth rate is $\mathrm{Im}(\omega)L_v/v_0 \sim 0.0636$. Figure 5.9(b) shows the $k_\parallel$-dependence of the growth rate of the K-H mode with $k_y\bar{\rho}_{te} \sim 0.0580$ ($k_y L_v \sim 0.833$). The K-H mode is stable for $k_\parallel L_v < 5.42 \times 10^{-5}$. These stability conditions are comparable with the marginally stable conditions, $k_y L_v = 1$ and $k_\parallel L_v \sim 7.23 \times 10^{-5}$, which are given by Eqs. (5.35) and (5.36).

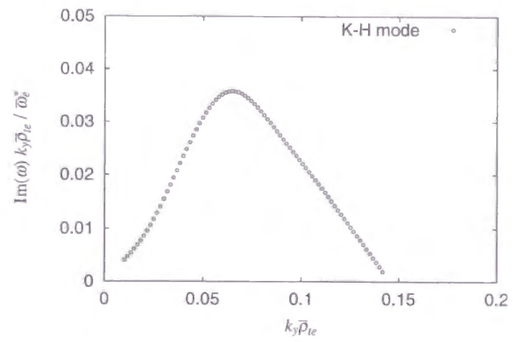

Figure 5.10: k_y-dependence of the growth rate spectrum of the electrostatic K-H mode is plotted for the single-helicity configuration ($k_\parallel = \mathbf{k}\cdot\mathbf{B}/B$) with $L_{ne}/L_{ns} = 0.430$. Other equilibrium parameters are the same as in Figs. 5.9(a) and 5.9(b).

In Fig. 5.10, the k_y-dependence of the growth rate of the electrostatic K-H mode is plotted for the model $E_r \times B$ flow profile with $L_v \sim 14.4\bar{\rho}_{te}$ and $x_c = 0$ in the negative shear configuration with $L_{ne}/L_{ns} = 0.430$. Here, $k_\parallel$ and k_y are related as $k_\parallel = \mathbf{k}\cdot\mathbf{B}/B = k_y B_y/B$ for the single helicity perturbations, where $B_y = B_0\{\Delta + (x/L_{ns})^2\}$. In the growth rate spectrum, the marginally stable k_y is estimated as $k_y L_v \sim 2.05$, and the peak of the growth rate is $\mathrm{Im}(\omega)L_v/v_0 \sim 0.052$. The enhancement of unstable k_y region in Fig. 5.10 may be explained by a driving effect due to density and temperature gradients which affect the

stability through the parallel electron dynamics or the Landau resonance.

In order to clearly see the K-H mode, we have chosen a system size as $N_x \times N_y = 256 \times 16$ in simulations shown in the following. In this system size, only the lowest wavenumber mode with $k_y \bar{\rho}_{te} \sim 0.0859$ is involved in an unstable k_y region of the K-H mode.

5.4.2 Magnetic shear stabilization of K-H mode

Since the linear stability of the K-H mode is sensitive to a variation of $k_\parallel$, it is considered that the $E_r \times B$ zonal flow profile is related to the q-profile. In Figs. 5.11(a)-5.11(d), we show time histories of the $E_r \times B$ zonal flow in simulations of the nonresonant NS-ETG mode with $\eta_e = \eta_i = 5$ and different q-profiles.

In the simulation with $L_{ne}/L_{ns} = 0$ shown in Fig. 5.11(a), quasi-steady $E_r \times B$ zonal flows are not generated. Also for other three cases, the region without $E_r \times B$ zonal flows is observed near the $q_{\min}$-surface. As is shown in Fig. 5.7(b), the reduction of χ_e is small in this region. Consequently, in a shearless case shown in Fig. 5.11(a), a difference of $\bar{\chi}_e$ between the simulations with and without the $E_r \times B$ flows is small ($\sim 15\%$) compared with that observed in a negative shear case shown in Fig. 5.11(c) ($\sim 75\%$). In Figs. 5.11(b)-5.11(d), the $E_r \times B$ zonal flows are generated in the finite magnetic shear regions in both side of the $q_{\min}$-surface, and a clear correlation between the $E_r \times B$ zonal flow profile and the q-profile is observed.

In order to show a correspondence between the observed $E_r \times B$ zonal flow profile and the K-H mode, the linear stability of the K-H mode is analyzed for the configurations used for Figs. 5.11(b)-5.11(d). In Fig. 5.12, a critical $E_r \times B$ flow velocity v_{0c} to stabilize the K-H mode is plotted for the model $E_r \times B$ flow profiles with $L_v \sim 14.4 \bar{\rho}_{te}$ and various neutral points x_c, where v_{0c} is the maximum flow velocity given by Eq. (5.39). It is seen that the radial distribution of v_{0c} is closely related to the q-profile. This result explain the feature of the $E_r \times B$ zonal flow profile observed in the gyrokinetic PIC simulation qualitatively. Also, the observed quasi-steady state with $E_r \times B$ zonal flows is considered as a stable equilibrium solution of the gyrokinetic Vlasov-Maxwell system. It is noted that v_{0c} in Fig. 5.12 is relatively larger than the observed $E_r \times B$ flow velocity of $\sim 0.015 \bar{v}_{ti}$. One reason

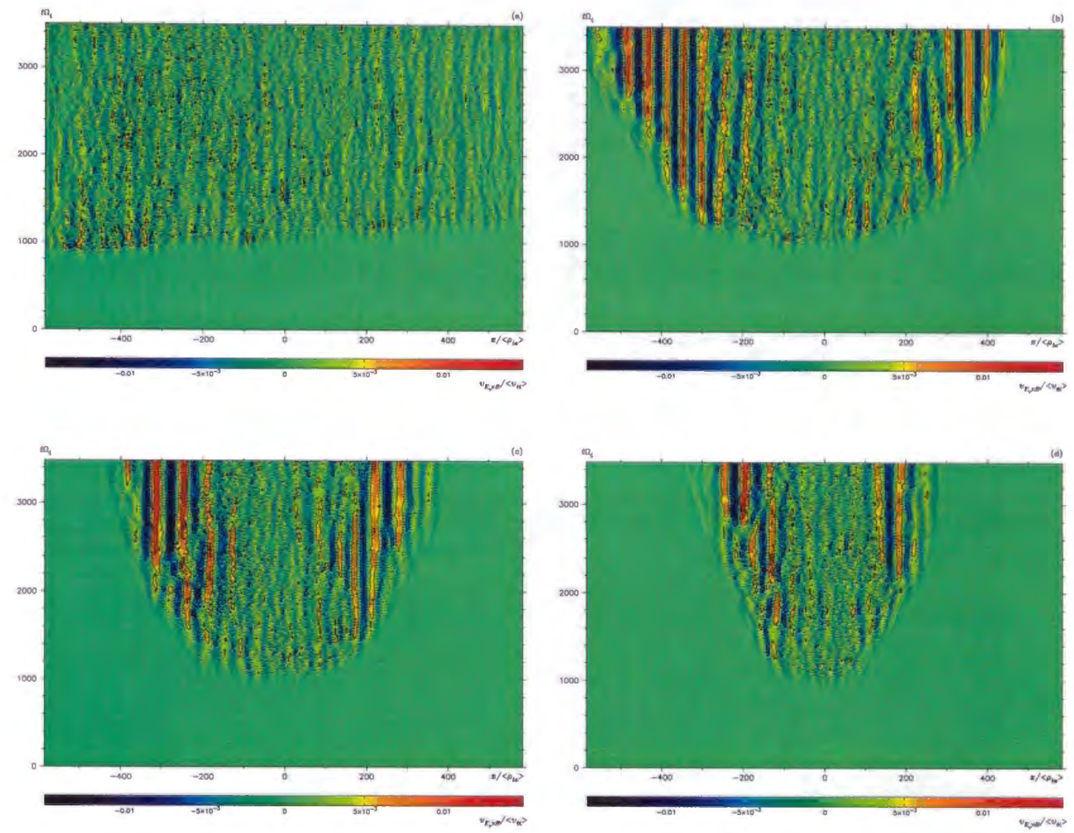

Figure 5.11: Time histories of the radial distribution of $v_{E_r \times B}$ are shown for the simulation of the nonresonant NS-ETG mode with (a) $L_{ne}/L_{ns} = 0$, (b) $L_{ne}/L_{ns} = 0.304$, (c)$L_{ne}/L_{ns} = 0.430$, and (d) $L_{ne}/L_{ns} = 0.609$. A correspondence between the q-profile and the $E_r \times B$ zonal flow region is observed.

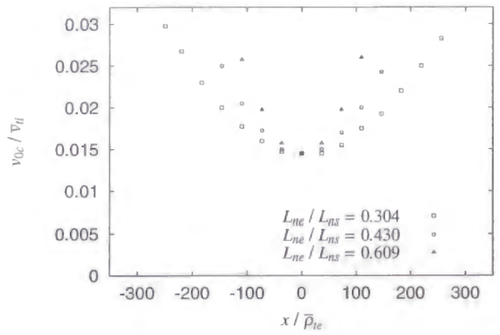

Figure 5.12: The critical $E_r \times B$ flow velocity v_{0c} of the K-H mode with $k_y \bar{\rho}_{te} \sim 0.0859$ is plotted for the negative shear configuration with $L_{ne}/L_{ns} = 0.304$ (open squares), $L_{ne}/L_{ns} = 0.430$ (open circles), and $L_{ne}/L_{ns} = 0.609$ (open triangles). A position of each plot corresponds to a neutral point x_c of a model $E_r \times B$ flow profile.

is that the model $E_r \times B$ flow profile given by Eq. (5.39) underestimates a free energy involved in the $E_r \times B$ zonal flows of multiple periods. Also, a nonlinear destabilization due to a mode coupling with fluctuations may be effective in the simulation.

5.4.3 Onset of K-H mode

Although we have discussed about an existence of the quasi-steady $E_r \times B$ zonal flow from a point of view of the linear stability of the K-H mode, the saturated turbulent state realized in a quasi-steady state of the nonlinear simulation is considered to be linearly stable for perturbations. In order to observe the K-H mode explicitly in the ETG turbulence, we make a linearly unstable state by artificially changing the q-profile in the simulation. Figures 5.13(a) and 5.13(b) show time histories of the $E_r \times B$ zonal flows in the simulation of the nonresonant NS-ETG mode with $\eta_e = \eta_i = 5$, $L_{ne}/L_{ns} \sim 0.609$, and $N_x \times N_y = 256 \times 16$. In Fig. 5.13(b), the q-profile is changed from $L_{ne}/L_{ns} \sim 0.609$ to $L_{ne}/L_{ns} \sim 0.304$ at $t\Omega_i \sim 4183$. After a change in the q-profile, the quasi-steady $E_r \times B$ zonal flows around $x/\bar{\rho}_{te} \sim \pm 200$ are destroyed, while such a change of the $E_r \times B$ zonal flows is not observed in Fig. 5.13(a). Also, in Fig. 5.13(b), a new generation of the $E_r \times B$ zonal flows is seen

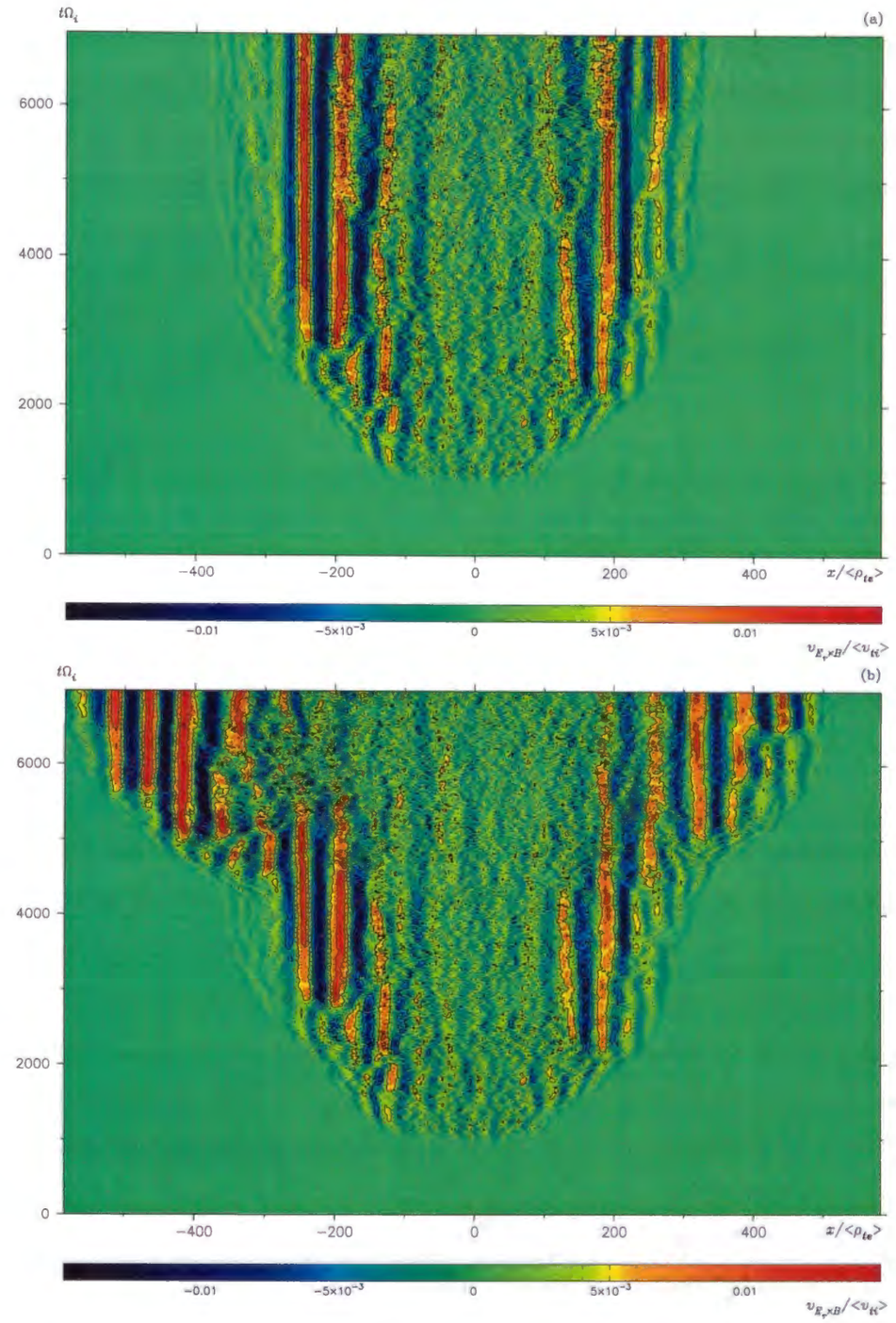

Figure 5.13: Time histories of the radial distribution of $v_{E_r \times B}$ are shown for the simulation of the nonresonant NS-ETG mode with $L_{ne}/L_{ns} = 0.609$. In a case (b), the q-profile is changed from $L_{ne}/L_{ns} = 0.609$ to $L_{ne}/L_{ns} = 0.304$ at $t\Omega_i = 4183$. The $E_r \times B$ zonal flows around $x/\bar{\rho}_{te} \sim \pm 200$ decay because of an onset of the K-H mode.

around $x/\bar{\rho}_{te} \sim \pm 400$. In this region, before the generation of the $E_r \times B$ zonal flows, the secondary instability with $k_y\bar{\rho}_{te} \sim 0.0859$ is observed again. The new $E_r \times B$ zonal flow region is also expanded in the radial direction, and the new quasi-steady $E_r \times B$ zonal flow profile around $x/\bar{\rho}_{te} \sim \pm 400$ is very similar to that observed in Fig. 5.11(b).

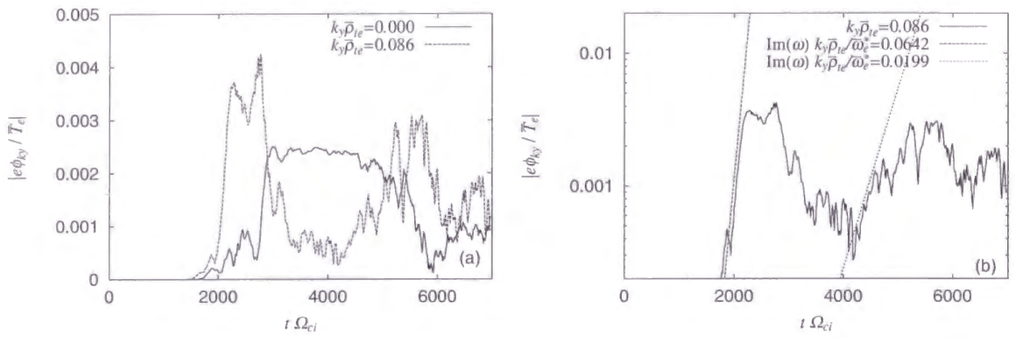

Figure 5.14: (a) shows the time history of the k_y spectrum of the electrostatic potential, which is averaged over the $E_r \times B$ zonal flow region for $x/\bar{\rho}_{te} = -233 \sim -183$ in Fig. 13(b). (b) shows a log scale plot of a $k_y\bar{\rho}_{te} \sim 0.0859$ mode.

In Figs. 5.14(a) and 5.14(b), a time history of the electrostatic potential fluctuation observed in the $E_r \times B$ zonal flow region for $x/\bar{\rho}_{te} = -233 \sim -183$ in Fig. 5.13(b) is plotted for $k_y = 0$ and $k_y\bar{\rho}_{te} \sim 0.0859$ modes, respectively. After a change in the q-profile at $t\Omega_i \sim 4183$, the linear growth of the K-H mode ($k_y\bar{\rho}_{te} \sim 0.0859$ mode) is seen. The damping of the $E_r \times B$ zonal flow ($k_y = 0$ mode) occurs after the K-H mode grows up to $e\phi_{k_y}/\bar{T}_e \sim 0.0015$. Here, the observed growth rate of the K-H mode is $\mathrm{Im}(\omega)k_y\bar{\rho}_{te}/\omega_e^* \sim 0.0199$. Accordingly, it is considered that the K-H mode works as a mechanism to destroy the $E_r \times B$ zonal flow.

In Figs. 5.14(a) and 5.14(b), the linear growth ($\mathrm{Im}(\omega)k_y\bar{\rho}_{te}/\omega_e^* \sim 0.0642$) of the secondary instability followed by the generation of the quasi-steady $E_r \times B$ zonal flow is observed for the $k_y\bar{\rho}_{te} \sim 0.0859$ mode at $t\Omega_i \sim 2000$. Properties of the secondary instability are summarized as follows: (a) the instability occurs in the neighborhood of the $E \times B$ shear flow or $E_r \times B$ zonal flow region, (b) the most unstable k_y region of the instability

around $k_y\bar{\rho}_{te} \sim 0.1$ is much lower than that of the ETG mode around $k_y\bar{\rho}_{te} \sim 0.3$, (c) after the saturation of the instability, the $E_r \times B$ zonal flow is generated, provided that $k_\parallel$ is sufficiently large, and (d) the instability propagates only in the weak magnetic shear region with $k_\parallel\bar{\rho}_{te} < 10^{-5}$. From these properties, it is considered that the secondary instability is the K-H mode, which becomes unstable in a front of the $E \times B$ shear flow or $E_r \times B$ zonal flow region. The propagation of the secondary instability may correspond to an avalanche process produced by a chain of the K-H instability and an associated generation of the $E_r \times B$ zonal flow.

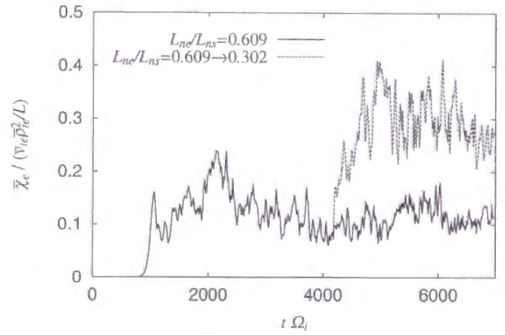

Figure 5.15: Time history of $\bar{\chi}_e$ is plotted for the simulations of the nonresonant NS-ETG mode shown in Fig. 13(a) and 13(b). After the onset of the K-H mode, $\bar{\chi}_e$ increases from $\bar{\chi}_e/(\bar{v}_{te}\bar{\rho}_{te}^2/L) \sim 0.1$ to $\bar{\chi}_e/(\bar{v}_{te}\bar{\rho}_{te}^2/L) \sim 0.3$.

Figure 5.15 shows a time history of $\bar{\chi}_e$ in the simulation shown in Figs. 5.13(a) and 5.13(b). After the change in the q-profile, we see a remarkable increase of $\bar{\chi}_e$ due to an onset of the K-H mode and the destruction of the $E_r \times B$ zonal flow.

5.5 Linear stability of ITG mode in ETG turbulence

The last problem addressed in this chapter is an analysis of the ITG mode in the presence of the ETG turbulence. As is seen in Fig. 4.6, the linear growth rate of the ETG mode is an order of magnitude larger than that of the ITG mode. Therefore, in studying the

ITG turbulence, it is necessary to consider effects of the ETG turbulence even for the linear stability. In this section, we focus on an effect of the $E_r \times B$ zonal flow which is generated from the ETG turbulence. Since the simulation of the ETG turbulence is performed with the adiabatic ions, the ITG mode is excluded artificially in the system. Here, we consider the gyrokinetic ions under microscopic equilibrium $E_r \times B$ zonal flows as a model configuration.

In the previous section, we have shown the gyrokinetic integral eigenmode equation (5.31) including the equilibrium $E_r \times B$ shear flows. In that case, the gyro-average for the equilibrium $E_r \times B$ shear flow is ignored under the ordering of $\rho_{te}/L_v \sim \mathcal{O}(\epsilon)$. However, for the case considered in this section, the scale length ordering is changed as $\rho_{ti}/L_v \sim \mathcal{O}(1)$, and the FLR effect becomes important also for the equilibrium $E_r \times B$ shear flow. This treatment in the gyrokinetic integral eigenvalue code becomes very complex because a velocity integral of the plasma dispersion function requires an integration also about the magnetic moment $\bar{M}$. Thus, we have developed a new initial value code based on the gyrokinetic particle simulation technique.

Since the gyrokinetic PIC code described in Section 5.2 is developed using the long wavelength approximation $k_\perp^2 \rho_{te}^2 \ll 1$ and the four-point averaging method, the higher order FLR effect for the microscopic $E_r \times B$ zonal flow with $\rho_{ti}/L_v \sim \mathcal{O}(1)$ can not be expressed. In order to treat the full FLR effect in the gyrokinetic particle simulation, we impose the consistency condition in the Fourier space where the FLR effect is expressed analytically with the zeroth order Bessel function J_0. We then write the nonlinear characteristics of the gyrokinetic equation as

$$\frac{d\bar{\mathbf{R}}}{dt} = \frac{c}{B_0}\langle \mathbf{E} \rangle_{\bar{\theta}} \times \mathbf{b} + \frac{\bar{v}_z}{B_0}\mathbf{B}, \tag{5.40}$$

$$\frac{d\bar{v}_z}{dt} = -\frac{e}{m_i B_0}\mathbf{B} \cdot \langle \mathbf{E} \rangle_{\bar{\theta}}, \tag{5.41}$$

$$\langle \mathbf{E} \rangle_{\bar{\theta}} = -\sum_{\mathbf{k}} i\mathbf{k}\left(\phi_{\mathbf{k}} + \Phi_{\mathbf{k}}\right) \exp(i\mathbf{k} \cdot \bar{\mathbf{R}}) S_{\mathbf{k}} J_0(k_\perp \bar{\rho}_i), \tag{5.42}$$

where $S_{\mathbf{k}}$ is the Gaussian form factor [45] of marker particles, and Φ is the equilibrium electrostatic potential which produces the $E_r \times B$ shear flows. In the present analysis, we assume microscopic $E_r \times B$ zonal flows produced by the electron density profile as shown in the simulations of the ETG turbulence. For the gyrokinetic ions and the adiabatic

electrons, the gyrokinetic Poisson equation including the full FLR effect is obtained as

$$-\nabla^2\phi + \frac{1}{\lambda_{Di}^2}\sum_{\mathbf{k}}\left[1 - I_0(k_\perp^2\rho_{ti}^2)\exp(-k_\perp^2\rho_{ti}^2)\right]\phi_{\mathbf{k}}\exp(i\mathbf{k}\cdot\mathbf{x}) + \frac{1}{\lambda_{De}^2}\phi = 4\pi e\int \delta\bar{F}_i(\bar{\mathbf{R}}, \bar{v}_z, \bar{M}, t)\delta([\bar{\mathbf{R}} + \bar{\rho}_i] - \mathbf{x})\bar{D}_i d^6\bar{\mathbf{Z}}. \tag{5.43}$$

As in the gyrokinetic integral eigenvalue code, this linear equation is solved in the Fourier space. A matrix form of the gyrokinetic Poisson equation (5.43) is written as

$$\sum_{k_l}\mathcal{L}_{k_m,k_l}\phi_{k_l} = \delta g_{ik_m}, \tag{5.44}$$

$$\mathcal{L}_{k_m,k_l} = \frac{1}{8\pi e L_x}\int_{-L_x}^{L_x} dx \exp[i(k_l - k_m)x] \times\left[(k_l^2 + k_y^2 + k_z^2) + \frac{1}{\lambda_{Di}^2}\left\{1 - I_0(b_i)\exp(-b_i)\right\} + \frac{1}{\lambda_{De}^2}\right], \tag{5.45}$$

$$\delta g_{i\mathbf{k}} = \frac{1}{L_x L_y L_z}\sum_j \bar{W}_{ij}\bar{D}_i S_{\mathbf{k}}\exp(-i\mathbf{k}\cdot\bar{\mathbf{R}}_j)J_0(k_\perp\bar{\rho}_{ij}), \tag{5.46}$$

where $b_i = (k_l^2 + k_y^2)\rho_{ti}^2$, and $\bar{W}_i$ is the particle weight of the nonlinear δf method. It is noted that both in Eqs. (5.42) and (5.46), the gyro-average is evaluated analytically, and, therefore, this scheme makes the treatment of the full FLR effect possible for the electric field with an arbitrary wavelength. Although we have developed a nonlinear gyrokinetic Fourier particle code, we apply this code only to linear calculations in this section. Since the system is symmetric in the y- and z-directions, k_y and k_z are specified by assuming a plane wave.

The calculation is performed for the $l = 0$ branch of the double mode-rational surface NS-ITG mode with $k_y\bar{\rho}_{ti} \simeq 0.833$. The equilibrium parameters are chosen as the same as the analyses shown in Figs. 3.1 and 3.2. For the linear analysis of the ITG mode with $k_y\bar{\rho}_{ti} < 1$, the adiabatic electron response is appropriate as discussed in Section 3.4. A model velocity profile of the equilibrium $E_r \times B$ zonal flow is chosen as the sinusoidal function,

$$v_{E_r\times B}(x) = v_0 \sin([\pi/2L_v]x), \tag{5.47}$$

where the flow shear parameter is chosen as $L_v \sim 16.7\bar{\rho}_{te}$ ($\bar{\rho}_{ti}/L_v \sim 4.59$) based on the $E_r \times B$ zonal flow profile observed in the simulation.

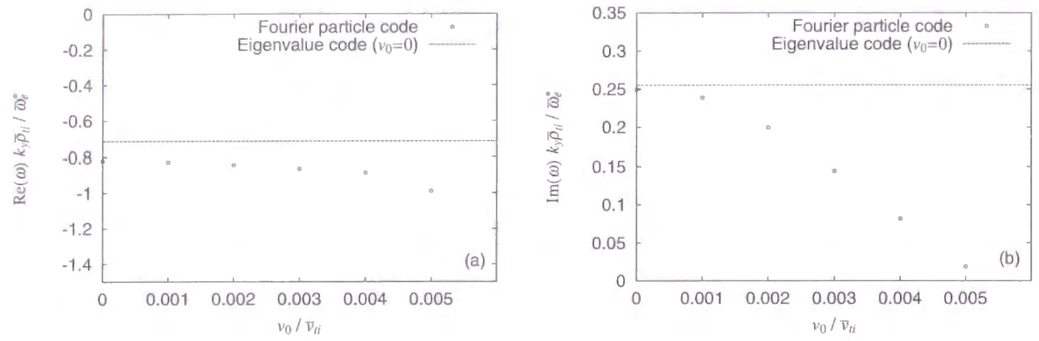

Figure 5.16: (a) Real frequency and (b) growth rate of the $l = 0$ branch of the double mode-rational surface NS-ITG mode with $k_y\bar{\rho}_{ti} \simeq 0.833$ are plotted against $v_0/\bar{v}_{ti}$ (open circles). The eigenfrequency without the equilibrium zonal flow obtained from the gyrokinetic integral eigenvalue code is shown for the comparison (broken line). The mode is stabilized by the sinusoidal $E_r \times B$ zonal flow with $v_0/\bar{v}_{ti} \sim 0.005$.

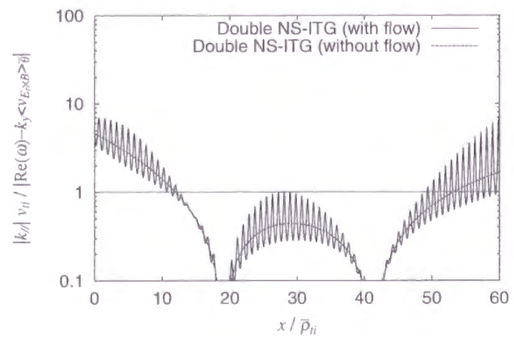

Figure 5.17: Resonance conditions with $(v_0/\bar{v}_{ti} = 0.004)$ and without $(v_0 = 0)$ the $E_r \times B$ zonal flow are compared. In the case with the $E_r \times B$ zonal flow, the gyro-average is evaluated for thermal ions with $\rho_i = \rho_{ti}$.

Figures 5.16(a) and 5.16(b) show the v_0-dependence of the real frequency and the growth rate of the double mode-rational surface NS-ITG mode. While the real frequency is insensitive to a change in v_0, the microscopic $E_r \times B$ zonal flow is remarkably effective for stabilizing the NS-ITG mode, and the marginally stable condition is given in a very small $E_r \times B$ flow velocity with $v_0/\bar{v}_{ti} \sim 0.005$. In order to understand the stabilizing mechanism, the resonance condition, $|k_\parallel|v_{ti}/|\mathrm{Re}(\omega) - k_y\langle v_{E_r\times B}\rangle_{\bar{\theta}}|$, is plotted for the cases with and without the $E_r \times B$ zonal flow in Fig. 5.17, where the gyro-average is evaluated for thermal ions, $\langle v_{E_r\times B}\rangle_{\bar{\theta}} = v_0 \sin([\pi/2L_v]x) J_0([\pi/2L_v]\rho_{ti})$. Since the real frequency is almost constant, the resonance condition is also not changed on average. However, in a wide range of the unstable region around the $q_{\min}$-surface, the local resonance condition is shifted from the most unstable condition due to the Doppler shift with the microscopic $E_r \times B$ zonal flow. This property that the resonance condition is shifted without changing the real frequency is a unique stabilizing mechanism of the microscopic $E_r \times B$ zonal flow. It is noted that such a change in the resonance condition can not be expected for the global $E_r \times B$ shear flow, because the real frequency is also shifted to sustain the instability.

5.6 Discussion

In this chapter, we have studied nonlinear dynamics of the ETG turbulence using a gyrokinetic finite element PIC code. In a negative-sheared slab configuration, simulations are performed for nonresonant single-helicity perturbations, because the nonresonant NS-ETG mode is considered to play a significant role in the electron anomalous transport based on the mixing length estimate. The principal results observed in the nonlinear simulation of the nonresonant NS-ETG mode are summarized as follows:(a) in the linear growth phase, a radially elongated vortex structure predicted by the linear theory appears, (b) in the initial saturation phase, a saturation of the ETG mode is produced by an inverse (normal) wave energy cascade in the k_y (k_x) space, which tends to generate $E \times B$ shear flows, (c) after the saturation of the ETG mode, the secondary instability followed by a generation of the $E_r \times B$ zonal flows occurs and the $E_r \times B$ zonal flow region is expanded in the radial direction, and (d) in the quasi-stationary phase, the quasi-steady $E_r \times B$ zonal flows, which

are stable for the K-H mode, is sustained, and a remarkable reduction of χ_e is observed in the $E_r \times B$ zonal flow region.

In the quasi-steady state of the simulation, the electron thermal transport coefficient is estimated as $\bar{\chi}_e \sim \bar{v}_{te}\bar{\rho}_{te}^2/L \sim 0.44\mathrm{m}^2/\mathrm{sec}$ ($\bar{\chi}_e \sim 0.3\bar{v}_{te}\bar{\rho}_{te}^2/L \sim 0.13\mathrm{m}^2/\mathrm{sec}$), where $L^{-1} = L_{ne}^{-1} + L_{te}^{-1}$. This coefficient is apparently comparable with χ_e observed in the ITB of the negative shear tokamaks [24, 30]. As was shown in the global gyrokinetic PIC simulation of the ITG turbulence [35], the $E_r \times B$ zonal flow generated by the ETG turbulence is effective for a reduction of χ_e. However, the mechanism of the reduction of the anomalous transport is different. In our simulation, the reduction of χ_e is explained by a decay of finite k_y modes due to a strong spectrum condensation into $k_y = 0$ mode which does not contribute to the anomalous χ_e. On the other hand, the reduction of the anomalous χ_i was explained by suppression and decorrelation of large vortices due to $E_r \times B$ zonal flows in the ITG turbulence [35].

The observed $E_r \times B$ zonal flow profile has a large amplitude $v_{E_r \times B} \sim 0.015\bar{v}_{ti}$ only in finite magnetic shear regions in both sides of the $q_{\min}$-surface, although an inverse energy cascade in the k_y space is observed also in a region of the $q_{\min}$-surface. Thus, the $E_r \times B$ zonal flow profile is closely related to the q-profile. From the linear stability analysis of the K-H mode, it is found that the parallel electron dynamics, which comes from an effect of the magnetic shear, has a stabilizing effect on the K-H mode. The observed $E_r \times B$ zonal flow profile may be explained by the local critical $E_r \times B$ flow velocity due to the magnetic shear or $k_\parallel$ stabilization. It is considered that the K-H mode play a critical role in the underlying physics of the $E_r \times B$ zonal flow in the ETG turbulence.

In the simulation shown in Fig. 5.13(b), it is shown that quasi-steady $E_r \times B$ zonal flows decay by changing the q-profile to reduce the magnetic shear. This result indicate that the K-H mode works to destroy the $E_r \times B$ zonal flow in a collisionless plasma. Thus, it is considered that a quasi-steady $E_r \times B$ zonal flow is determined by a competition between a flow generation process due to an inverse energy cascade in the k_y space and a flow destruction due to the K-H mode. Also, the simulation results show a possibility of controlling the $E_r \times B$ zonal flow and the resulting confinement property by changing the q-profile.

The linear stability analysis of the ITG mode in the presence of a microscopic model $E_r \times B$ flow has shown that the $E_r \times B$ zonal flow with $\rho_{ti}/L_v \sim \mathcal{O}(1)$ is effective for stabilizing the ITG mode. Therefore, if a generation of the microscopic $E_r \times B$ zonal flow is a universal property of the ETG turbulence in the negative shear configuration, this result may explain the observation that χ_i is reduced to a level of the neoclassical transport in the ITB region.

Chapter 6

Conclusions

The gyrokinetic Vlasov-Maxwell system is the most rigorous kinetic description of the low frequency dynamics in a collisionless high temperature tokamak plasmas. In this thesis, we have analyzed linear and nonlinear properties of micro-instabilities particularly for the negative shear configuration, based on the gyrokinetic theory.

In the gyrokinetic Vlasov-Maxwell system, low frequency phenomena in tokamak plasmas are described efficiently without losing important kinetic effects, such as the Landau resonance and the FLR effect. In the gyrokinetics, a gyro-phase dependent part of perturbations, which is recognized as a non-secular perturbation in analyzing low frequency waves, is removed from the Vlasov-Maxwell system using the action-variational Lie perturbation method. Since an inherent nature of the Hamiltonian system is conserved due to the area preserving property of the Lie transform, the gyrokinetic Vlasov-Maxwell system is appropriate for studying nonlinear dynamics via a computer simulation. In this thesis, we have applied this technique also to the treatment of fast passing motion of high energy drift-kinetic electrons, and the orbit-averaging model has been developed in the gyrokinetic simulation. The model will be extended to include a bounce motion of trapped particles in a toroidal case. Since a low cost simulation of low frequency waves with drift-kinetic electrons was demonstrated [59], this model possesses a promising feature for future application of the global gyrokinetic simulation to low frequency kinetic phenomena such as the collisionless tearing mode [89], where electrons play a crucial role.

One of the goals in this thesis has been the linear analysis of micro-instabilities in a

weak magnetic shear region around the $q_{\min}$-surface, where a WKB approach can not be used. To this end, we have developed a gyrokinetic integral eigenvalue code. Numerical results have shown that both the slab ITG mode and the slab ETG mode becomes strongly unstable around the $q_{\min}$-surface, and they are classified into three types of branches depending on the number of mode-rational surfaces: a single mode-rational surface mode, a double mode-rational surface mode, and a nonresonant mode. We have derived new analytic solutions for the double mode-rational surface and nonresonant modes, which have a significant contribution to the anomalous transport based on the mixing length estimate. The properties of these modes are summarized as follows:

NS-ITG mode

(a) The double mode-rational surface (nonresonant) NS-ITG mode becomes a bounded (oscillatory) solution around the $q_{\min}$-surface.

(b) Since this mode is excited in the weak magnetic shear region around the $q_{\min}$-surface, the stability is basically determined locally at the $q_{\min}$-surface.

(c) The unstable k_y region of the NS-ITG mode spreads up to $k_y\rho_{ti} \sim 10$ by following the local dispersion, while that of the normal-sheared slab ITG mode is limited for $k_y\rho_{ti} < 1$.

(d) The eigenfunctions have a broad radial eigenmode structure around the $q_{\min}$-surface, and their radial correlation lengths are several times larger than that of the normal-sheared slab ITG mode.

NS-ETG mode

(a) For typical fusion plasma parameters with $\rho_{te}^2/\lambda_{De}^2 \ll 1$, the properties of the ETG mode become different from the ITG mode, because of the Debye shielding effect.

(b) The double mode-rational surface (nonresonant) NS-ETG mode becomes a oscillatory (bounded) solution around the $q_{\min}$-surface.

(c) The stability is determined locally at the $q_{\min}$-surface, but the unstable k_y region is limited for $k_y\rho_{te} < 1$, because the scale length is characterized by λ_{De}.

(d) The NS-ETG mode has an order of magnitude larger radial correlation length than that of the conventional normal-sheared slab ETG mode.

These particular properties of the NS-ITG mode and the NS-ETG mode have been clarified for the first time by the present analyses with the gyrokinetics. In this thesis, we have shown that several approximations or assumptions used in the conventional stability theory are inappropriate especially for the negative shear tokamaks. Although a reduced model such as the fluid model is useful to understand physics qualitatively from the obtained numerical results, the gyrokinetic model is indispensable for a complete description of the drift-wave turbulence.

The main object in the study of the drift-wave turbulence is to investigate physics of a plasma turbulence as well as an estimation of the transport coefficient. In the normal shear case, the linearly unstable k_y region of the ITG mode for $k_y\rho_{ti} < 1$ and that of the ETG mode for $k_y\lambda_{De} < 1$ are separated each other. This may imply that the ITG turbulence is independent of the ETG turbulence, and that a simulation model of the ITG turbulence assuming adiabatic electrons is usable for a conventional normal shear configuration. However, in the negative shear case, their unstable regions overlap each other around $k_y\rho_{ti} \sim 10$ ($k_y\lambda_{De} \sim 0.4$). In other words, in the wavenumber space, an energy source of the ETG turbulence exists in an energy sink region of the ITG turbulence. Since the growth rate of the ETG mode is an order of magnitude larger than that of the ITG mode, effects of the ETG turbulence can not be ignored in studying the ITG turbulence. Therefore, especially in the negative shear tokamaks, non-adiabatic electrons play a significant role in a formation of the drift-wave turbulence.

From the conventional mixing length estimate, it is found that both the NS-ITG mode and the NS-ETG mode give order of magnitude larger transport coefficients compared with those in the normal shear cases. The obtained large transport coefficient of the NS-ITG mode seems to be inconsistent with an improved ion energy confinement in the negative shear discharges with the ITB. Hence, the NS-ITG modes may be suppressed by other

effects such as the $E_r \times B$ flow shear, as shown in Section 5.5. However, even if the $E_r \times B$ shear flow is considered, it may be insufficient to stabilize the NS-ETG modes, because it is difficult to satisfy the stability condition, $\omega_{E_r \times B} > \mathrm{Im}(\omega)$. For the electron energy confinement, the transport coefficient due to the NS-ETG mode may explain the residual anomalous electron thermal transport in the ITB of the negative shear tokamaks.

Effects of $E_r \times B$ shear flows on ITG modes were studied in the previous works [37, 39]. In their treatment of mean $E_r \times B$ flows, an equilibrium electric field was imposed as an external field. However, as shown in the linear theory of the K-H mode, if we consider the self-consistent density profile in the $E_r \times B$ shear flows, the K-H mode may become unstable. For proper estimation of the stability limit including the K-H mode, a careful determination of a radial electric field through the Poisson equation with both the ion and electron density profiles is required, because the charge density (the electrostatic potential) in a plasma corresponds to the vorticity (the stream function) in a neutral fluid.

In the present linear calculations, we have considered only the slab drift waves, which are driven by the resonant interaction between transit particles and electrostatic waves. Thus, the present results may not be sufficient for a quantitative comparison with tokamak experiments, since the driving force due to the toroidal effects such as toroidal guiding center drift, trapped particles, and the toroidal mode coupling is not included. However, it is shown that the toroidal effects tend to become weak for the negative shear configuration and the slab-type drift waves are relevant to understand experimental results.

Another goal in this thesis has been understanding of nonlinear physics of the drift-wave turbulence. Firstly, we have addressed the ETG mode whose growth time is much faster than that of the ITG mode. In order to study nonlinear dynamics of the ETG turbulence, we have developed a gyrokinetic finite element PIC code. In this thesis, we have applied a two-and-a-half dimensional model to the negative shear configuration. Simulations are performed particularly for the nonresonant NS-ETG mode, because its contribution to the electron anomalous transport based on the mixing length theory is the largest among several branches of the NS-ETG modes. The principal results observed in the nonlinear simulation of the nonresonant NS-ETG mode are summarized as follows:

(a) In the linear growth phase, a radially elongated vortex structure predicted by the linear theory is seen.

(b) In the initial saturation phase, a saturation of the ETG mode is produced by an inverse (normal) wave energy cascade in the k_y (k_x) space, which tends to generate the $E \times B$ shear flows.

(c) After the saturation of the ETG mode, the secondary instability followed by a generation of the $E_r \times B$ zonal flows occurs and the $E_r \times B$ zonal flow region is expanded in the radial direction.

(d) In the quasi-stationary phase, the quasi-steady $E_r \times B$ zonal flows, which are stable against the K-H mode, is sustained, and a remarkable reduction of χ_e is observed in the $E_r \times B$ zonal flow region.

From analyses of the simulation data, various new underlying physics in the ETG turbulence has been revealed.

The electron thermal transport coefficient $\bar{\chi}_e \sim \bar{v}_{te}\bar{\rho}_{te}^2/L \sim 0.44\mathrm{m}^2/\mathrm{sec}$ observed in the turbulent region around the $q_{\min}$-surface is large enough for explaining χ_e observed in the ITB of the negative shear tokamaks [24, 30]. It is noted that this coefficient is much smaller than that obtained from the mixing length estimate, since the linear eigenmode structure is not sustained after the nonlinear saturation of the ETG mode. On the other hand, in the $E_r \times B$ zonal flow region, an electron heat flux is strongly suppressed, because of the strong spectrum condensation into $k_y = 0$ mode which does not contribute to the anomalous χ_e.

From the Rayleigh necessary condition for instability, the K-H mode is basically unstable, if we consider a shearless slab configuration or a two-dimensional magnetized plasma. However, in a sheared slab configuration, the parallel electron dynamics induced by the magnetic shear has a stabilizing effect on the K-H mode. The linear stability analysis of the K-H mode has shown a close correspondence between the stability limit of the K-H mode and the q-profile. This feature is qualitatively consistent with simulation results, where $E_r \times B$ zonal flows are generated only in the finite magnetic shear regions, although an inverse energy cascade in the k_y space is also observed in the weak magnetic shear re-

gion. Also, it has been shown that quasi-steady $E_r \times B$ zonal flows decay by changing the q-profile to reduce the magnetic shear. Therefore, the K-H mode play a critical role in the underlying physics of the $E_r \times B$ zonal flow in the ETG turbulence. And, it is considered that a quasi-steady $E_r \times B$ zonal flow is determined by a competition between a flow generation process due to an inverse energy cascade in the k_y space and a flow destruction due to the K-H mode. These results imply a possibility of controlling the $E_r \times B$ zonal flow and the resulting confinement property by changing the q-profile.

We have shown that the microscopic $E_r \times B$ zonal flow with $\rho_{ti}/L_v \sim \mathcal{O}(1)$ has a strong stabilizing effect on the ITG mode. If the generation of the microscopic $E_r \times B$ zonal flow is a universal feature of the ETG turbulence in the negative shear configuration, a suppression of the ITG mode due to the ETG turbulence may be a plausible candidate for explaining a reduction of χ_i to a level of neoclassical transport in the ITB region of the negative shear tokamaks. However, in the present work, the study of the ETG turbulence formed by the nonresonant NS-ETG mode has been limited within a two-and-a-half dimensional slab model. For three-dimensional models, besides the nonresonant NS-ETG mode, the single and double mode-rational surface NS-ETG modes become unstable. Also, the linear stability of the K-H mode may be affected by multiple-helicity perturbations. In order to confirm the $E_r \times B$ zonal flow generation completely, three-dimensional simulations will be necessary in the future work.

As has been discussed in this thesis, the anomalous transport process or plasma turbulence in high temperature fusion plasmas is characterized by various kinetic and fluid phenomena. The gyrokinetic integral eigenvalue code and the gyrokinetic PIC simulation code are powerful tools in analyzing linear and nonlinear properties of such a complex system. With the gyrokinetic integral eigenvalue code, we have analyzed the ITG and ETG modes both in the normal shear and negative shear configuration, and the K-H mode arising from quasi-steady $E_r \times B$ zonal flows. Accordingly, this code is applied to any kind of micro-instabilities in arbitrary equilibrium configurations, provided that the gyrokinetic ordering is not violated. Also, this code is useful as a tool for analyzing linear properties of a nonlinearly saturated state or a new equilibrium state realized in a nonlinear simulation. However, nonlinear properties such as a saturation mechanism of micro-instabilities and a

generation mechanism of $E_r \times B$ shear flows are beyond linear calculations. Therefore, it is thought that both the gyrokinetic integral eigenvalue code and the gyrokinetic PIC code mutually play a complementary role in a simulation study of tokamak plasmas. Future work will be an extension of these codes to a toroidal geometry and an electromagnetic waves.

Bibliography

[1] W. W. Lee, Phys.Fluids **26**, 556 (1983).

[2] E. A. Frieman and L. Chen, Phys. Fluids **25**, 502 (1982).

[3] D. H. E. Dubin, J. A. Krommes, C. Oberman, and W. W. Lee, Phys. Fluids **26**, 3524 (1983).

[4] T. S. Hahm, W. W. Lee, and A. Brizard, Phys. Fluids **31**, 1940 (1988).

[5] T. S. Hahm, Phys. Fluids **31**, 2670 (1988).

[6] S. Ejima, T. W. Petrie, A. C. Riviere *et al.*, Nuclear Fusion **22**, 1627 (1982).

[7] R. J. Groebner, W. Pfeiffer, F. P. Blau *et al.*, Nuclear Fusion **26**, 543 (1986).

[8] R. J. Fonck, G. Cosby, R. D. Durst *et al.*, Phys. Rev. Lett **70**, 3736 (1993).

[9] R. J. Hawryluk, S. Batha, W. Blanchard *et al.*, Phys. Plasmas **5**, 1577 (1998).

[10] B. B. Kadomitsev and O. P. Pogutse, *Reviews of Plasma Physics, Turbulence in Toroidal Systems* (Consultants bureau, New York, 1970), Vol. 5, Chapter 2.

[11] A. B. Mikhailovskii, *Theory of Plasma Instabilities, Volume* 2 : *Instabilities of an Inhomogeneous Plasma* (Consultants bureau, New York, 1974).

[12] W. Horton, Jr., D. I. Choi, and W. M. Tang, Phys. Fluids **24**, 1077 (1981).

[13] D. L. Brower, W. A. Peebles, S. K. Kim *et al.*, Phys. Rev. Lett. **59**, 48 (1987).

[14] W. A. Peebles, D. L. Brower, R. Philipona *et al.*, in *Plasma Physics and Controlled Nuclear Fusion Research 1990, Washington, D.C.* (IAEA, Vienna, 1991), Vol. 1, p589.

[15] R. D. Durst, R. J. Fonck, J. S. Kim *et al.*, Phys. Rev. Lett. **71**, 3135 (1993).

[16] G. Rewoldt, W. M. Tang, and R. J. Hastie, Phys. Fluids **30**, 807 (1987).

[17] M. Kotschenreuther, G. Rewoldt, and W. M. Tang, Comput. Phys. Commun. **88**, 128 (1995).

[18] F. M. Levinton, M. C. Zarnstorff, S. H. Batha *et al.*, Phys. Rev. Lett. **75**, 4417 (1995).

[19] E. J. Strait, L. L. Lao, M. E. Mauel *et al.*, Phys. Rev. Lett. **75**, 4421 (1995).

[20] T. Fujita, S. Ide, H. Shirai *et al.*, Phys. Rev. Lett. **78**, 2377 (1997).

[21] Y. Koide, M. Kikuchi, M. Mori *et al.*, Phys. Rev. Lett. **72**, 3662 (1994).

[22] T. Fujita, T. Hatae, T. Oikawa *et al.*, Nuclear Fusion **38**, 207 (1998).

[23] C. M. Greenfield, D. P. Schissel, B. W. Stallard *et al.*, Phys. Plasmas **4**, 1596 (1997).

[24] H. Shirai and the JT-60 Team, Phys. Plasmas **5**, 1712 (1998).

[25] K. H. Burrell, Phys. Plasmas **4**, 1499 (1997).

[26] R. E. Waltz, G. D. Kerbel, J. Milovich *et al.*, Phys. Plasmas **2**, 2408 (1995).

[27] Y. C. Lee, J. Q. Dong, P. N. Guzdar, and C. S. Liu, Phys. Fluids **30**, 1331 (1987).

[28] W. Horton, B. G. Hong, and W. M. Tang, Phys. Fluids **31**, 2971 (1988)

[29] G. M. Staebler, R. E. Waltz, C. M. Greenfield, and B. W. Stallard, in *Plasma Physics and Controlled Nuclear Fusion Research 1998*, 18th IAEA Fusion Energy Conference, Yokohama, Japan, 1998 (International Atomic Energy Agency, Vienna, 1998), p. F1-CN-69/THP2/13.

[30] B. W. Stallard, C. M. Greenfield, G. M. Staebler *et al.*, Phys. Plasmas **6**, 1978 (1999).

[31] S. Brunner and J. Vaclavik, Phys. Plasmas **5**, 365 (1998).

[32] S. Brunner, M. Fivaz, T. M. Tran, and J. Vaclavik, Phys. Plasmas **5**, 3929 (1998).

[33] M. Fivaz, S. Brunner, G. Ridder *et al.*, Comput. Phys. Commun. **111**, 27 (1998).

[34] R. D. Sydora, V. K. Decyk, and J. M. Dawson, Plasma Phys. Control. Fusion **38**, A281 (1996).

[35] Z. Lin, Science, **281**, 1835 (1998).

[36] W. M. Tang, G Rewolt, and E. A. Frieman, Phys. Fluids **23**, 2454 (1980).

[37] M. Artun and W. M. Tang, Phys. Fluids B **4**, 1102 (1992).

[38] W. M. Tang and G. Rewoldt, Phys. Fluids B **5**, 2451 (1993).

[39] S. Hamaguchi and W. Horton, Phys. Fluids B **4**, 319 (1992).

[40] B. B. Kadomitsev, *Plasma Turbulence* (Academic Press, London, 1965).

[41] R. Z. Sagdeev and A. A. Galeev, *Nonlinear Plasma Theory* (Benjamin, New York, 1969).

[42] ITER Physics Basis Editors, Nuclear Fusion **39**, 2137 (1999).

[43] C. K. Birdsall and A. B. Langdon, *Plasma Physics via Computer Simulation* (Adam Hilger, Bristol and New York, 1991).

[44] R. W. Hockney and J. W. Eastwood, *Computer Simulation Using Particles* (Adam Hilger, Bristol and New York, 1988).

[45] T. Tajima, *Computational Plasma Physics : With Applications to Fusion and Astrophysics* (Addison-Wesley, Redwood City, California, 1989).

[46] Y. Idomura, S. Tokuda, and M. Wakatani, Comput. Phys. Commun. **102**, 68 (1997).

[47] R. G. Littlejohn, J. Math. Phys. **23**, 742 (1982).

[48] J. R. Cary and R. G. Littlejohn, Ann. Phys. **151**, 1 (1983).

[49] W. W. Lee, J. Comput. Phys. **72**, 243 (1987).

[50] A. M. Dimits, T. J. Williams, J. A. Byers, and B. I. Cohen, Phys. Rev. Lett. **77**, 71 (1996).

[51] A. M. Dimits, G. Bateman, M. A. Beer *et al.*, Phys. Plasmas **7**, 969 (2000).

[52] A. Hasegawa, Adv. Phys. **34**, 1 (1985).

[53] A. Hasegawa and M. Wakatani, Phys. Rev. Lett. **59**, 1581 (1987).

[54] P. H. Diamond and Y. B. Kim, Phys. Fluids B **3**, 1626 (1991).

[55] P. H. Diamond, M. N. Rosenbluth, F. L. Hinton *et al.*, in *Plasma Physics and Controlled Nuclear Fusion Research*, 18th IAEA Fusion Energy Conference, Yokohama, Japan, 1998 (International Atomic Energy Agency, Vienna, 1998), p. IAEA-CN-69/TH3/1.

[56] S. Chandrasekhar, *Hydrodynamic and Hydromagnetic Stability*, (Clarendon, Oxford, 1961).

[57] M. A. Beer, Ph. D. thesis, Princeton University, (1993).

[58] M. N. Rosenbluth and F. L. Hinton, Phys. Rev. Lett. **80**, 724 (1998).

[59] Y. Idomura, S. Tokuda, and M. Wakatani, J. Plasma and Fusion Res. **72**, 131 (1999).

[60] Y. Idomura, S. Tokuda, and M. Wakatani, Phys. Plasmas **6**, 4658 (1999).

[61] Y. Idomura, S. Tokuda, and M. Wakatani, to be published in Phys. Plasmas **7** (2000).

[62] F. Jenko, Bull. Am. Phys. Soc. **44**, 91 (1999).

[63] Y. Idomura, S. Tokuda, and M. Wakatani, submitted to Phys. Plasmas.

[64] S. Ichimaru, *Statistical Plasma Physics, Volume* I : *Basic Principles* (Addison-Wesley, Redwood City, California, 1992).

[65] N. Rostoker and M. N. Rosenbluth, *Phys. Fluids* **3**, 1 (1960).

[66] N. A. Krall and A. W. Trivelpiece, *Principles of Plasma Physics* (McGraw-Hill, New York, 1973).

[67] S. Tokuda, H. Naitou, and W. W. Lee, J. Plasma and Fusion Res. **74**, 44 (1998).

[68] B. H. Fong and T. S. Hahm, Phys. Plasmas **6**, 188 (1999).

[69] J. Li, W. Qu, L. Huang, and J. Zhang, Phys. Lett. A **233**, 85 (1997).

[70] J. Li, L. Huang, and W. Qu, Phys. Plasmas **5**, 959 (1998).

[71] R. B. White, J. Comput. Phys. **31**, 409 (1979).

[72] J. Q. Dong, Y. Z. Zhang, and S. M. Mahajan, Phys. Plasmas **4**, 3334 (1997).

[73] B. Davies, J. Comput. Phys. **66**, 36 (1986).

[74] R. D. Sydora, U.S.-Japan Workshop on ITG Turbulent Transport (AIP Press, New York, 1993), p 224.

[75] B. Coppi, M. N. Rosenbluth, and R. Z. Sagdeev, Phys. Fluids **10**, 582 (1967).

[76] T. S. Hahm and W. M. Tang, Phys. Fluids B **1**, 1185 (1989).

[77] L. Chen, *Waves and Instabilities in Plasmas* (World Scientific, Singapore and New Jersey, 1987), Chapter IV.

[78] L. D. Landau and E. M. Lifshitz, *Quantum Mechanics, Non-relativistic Theory* (Pergamon Press, Oxford, 1977), Chapter VI.

[79] M. Abramowitz and I. A. Stegun, *Handbook of Mathematical Functions with Formulas, Graphs, and Mathematical Tables* (Dover Publications, New York, 1965), p378.

[80] K. L. Wong, N. L. Bretz, T. S. Hahm, and E. Synakowski, Phys. Lett. A **236**, 339 (1997).

[81] J. A. Byers, A. M. Dimits, Y. Matsuda *et al.*, J. Comput. Phys. **115**, 352 (1994).

[82] Y. Kishimoto, J. Y. Kim, W. Horton *et al.*, Plasma Phys. Control. Fusion **40**, A663 (1998).

[83] P. Satyanarayana, Y. C. Lee, and J. D. Huba, J. Geophys. Res. **92**, 8813 (1987).

[84] P. L. Pritchett, Phys. Fluids B **5**, 3770 (1993).

[85] S. E. Parker and W. W. Lee, Phys. Fluids B **5**, 77 (1993).

[86] A. Hasegawa, C. G. Maclennan, and Y. Kodama, Phys. Fluids **22**, 2122 (1979).

[87] P. G. Drazin, J. Fluid Mech. **4**, 214 (1958).

[88] P. L. Pritchett and F. V. Coroniti, J. Geophys. Res. **89**, 168 (1984).

[89] H. Naitou, K. Tsuda, W. W. Lee and R. D. Sydora, Phys. Plasmas **2**, 4257 (1995).